ΜΕΤΑΠΤΥΧΙΑΚΗ ΔΙΠΛΩΜΑΤΙΚΗ ΕΡΓΑΣΙΑ ΟΝΟΜΑΤΕΠΩΝΥΜΟ: ΙΩΑΝΝΗΣ ΠΑΓΩΝΗΣ
ΤΙΤΛΟΣ: Growth and characterization of Type I (Straddling gap) and Type II (staggered gap) heterojunctions alignment in thin films for potential photovoltaic applications
ΠΜΣ-Φυσικής   *Τμήμα Φυσικής*   *Πανεπιστήμιο Ιωαννίνων*

Πρόγραμμα Μεταπτυχιακών Σπουδών στη Φυσική
Τμήμα Φυσικής
Σχολή Θετικών Επιστημών Πανεπιστήμιο Ιωαννίνων

ΜΕΤΑΠΤΥΧΙΑΚΗ ΔΙΠΛΩΜΑΤΙΚΗ ΕΡΓΑΣΙΑ (Μ.Δ.Ε)

Growth and characterization of Type I (Straddling gap) and Type II (staggered gap) heterojunctions alignment in thin films for potential photovoltaic applications

ΙΩΑΝΝΗΣ ΠΑΓΩΝΗΣ
Αριθμός Μητρώου: 827

Επιβλέπων καθηγητής: ΓΕΩΡΓΙΟΣ ΕΥΑΓΓΕΛΑΚΗΣ
Ομότιμος Καθηγητής Τμήματος Φυσικής Π.Ι.

Ιωάννινα
15/7/2024

Μέλη Τριμερούς Εξεταστικής Επιτροπής

Ευαγγελάκης Γεώργιος, Ομότιμος Καθηγητής Σχολής Θετικών Επιστημών του Τμήματος Φυσικής του Π.Ι.

Δεληγιαννάκης Ιωάννης, Καθηγητής Σχολής Θετικών Επιστημών του Τμήματος Φυσικής του Π.Ι.

Ευαγγέλου Ευάγγελος, Αναπληρωτής Καθηγητής Σχολής Θετικών Επιστημών του Τμήματος Φυσικής του Π.Ι.

Περίληψη

Παρουσιάζουμε αποτελέσματα μελέτης αναφορικά με τις επιδόσεις δύο διαφορετικών συστημάτων λεπτών υμενίων, εκ των οποίων το ένα αποτελείται από δύο ημιαγώγιμα υλικά στα οποία η ευθυγράμμιση των ενεργειακών ζωνών τους σχηματίζουν ετεροεπαφές Τύπου Ι (straddling gap) και στο άλλο Τύπου ΙΙ (staggered gap). Τα λεπτά υμένια αναπτύχθηκαν με μια διαδικασία δύο βημάτων εκ των οποίων το πρώτο βήμα είναι η εναπόθεση με την μέθοδο της μαγνητικά υποβοηθούμενης ιοντοβολής (magnetron sputtering) ενός μεταλλικού υμενίου σε υπόστρωμα n-τύπου Si(001) και ακολούθως οξείδωση με χρήση πλάσματος οξυγόνου. Για το σύστημα της ετεροεπαφής Τύπου Ι (straddling gap) αναπτύξαμε κράμα Zr-Ti-Cu που ακολούθως οξειδώθηκε, ενώ για την ετεροεπαφή Τύπου ΙΙ (staggered gap) εναποθέσαμε μεταλλικό Sn ο οποίος κατόπιν οξείδωσης σε πλάσμα οξυγόνου παρήγαγε Sn_xO_y , SnO και SnO_2 τα οποία είναι n,p και n τύπου ημιαγωγοί αντιστοίχως. Τα αναπτυχθέντα λεπτά υμένια αναλύθηκαν ως προς την κρυσταλλική δομή με σκέδαση ακτινών-X (XRD) και ως προς τον στοιχειακό και χημικό χαρακτηρισμό με την μέθοδο της φασματοσκοπίας φωτοηλεκτρονίων ακτινών-X (XPS). Για την πρώτη εκτίμηση των φωτο-ηλεκτρικών επιδόσεων των συστημάτων λεπτών υμενίων πραγματοποιήθηκε I-V ηλεκτρικός χαρακτηρισμός με μέτρηση 4-σημείων και με μετρήσεις φωτορεύματος σε μέτρηση 2-σημείων. Αποδείχθηκε ότι τα συστήματα τα οποία εμπεριέχουν ημιαγωγούς με ετεροεπαφές Τύπου ΙΙ αποδίδουν πολύ καλύτερα σε σχέση με εκείνα που έχουν Τύπου Ι, υποδηλώνοντας ότι αυτά τα υλικά είναι πολλά υποσχόμενα για μελλοντικές φωτοηλεκτρικές χρήσεις.

Abstract

We present results referring to the performances of two different thin films, one composed by two semiconductors exhibiting band alignment of Type I (straddling gap) and another on of Type II (staggered gap). The films were grown by means of a two-step process consisting in depositing first a metallic layer on silicon n-type semiconductor and subsequently oxidize it in oxygen plasma. For the type I band gap system we grow a Zr-Ti-Cu alloy, while for, the type II, we deposited metallic tin (Sn) considering that upon oxidation Sn_xO_y, SnO SnO_2 will be produced that are n,p and n type semiconductors, respectively. The grown films were analyzed by means of X-Ray Diffraction (XRD) and X-Ray Photoelectron spectroscopy (XPS) for the structural and compositional characterizations, while we used I-V four probe and photo-current measurements for the assessment of their photo-electrical performances. It came out that the systems containing semiconductors having electronic Type II band alignment perform significantly better than those of type I, suggesting that these systems could be promising for photo-electric application.

ΜΕΤΑΠΤΥΧΙΑΚΗ ΔΙΠΛΩΜΑΤΙΚΗ ΕΡΓΑΣΙΑ ΟΝΟΜΑΤΕΠΩΝΥΜΟ: ΙΩΑΝΝΗΣ ΠΑΓΩΝΗΣ
ΤΙΤΛΟΣ: Growth and characterization of Type I (Straddling gap) and Type II (staggered gap) heterojunctions alignment in thin films for potential photovoltaic applications
ΠΜΣ-Φυσικής   *Τμήμα Φυσικής*   *Πανεπιστήμιο Ιωαννίνων*

ΕΥΧΑΡΙΣΤΙΕΣ

Contents

ΜΕΤΑΠΤΥΧΙΑΚΗ ΔΙΠΛΩΜΑΤΙΚΗ ΕΡΓΑΣΙΑ ΟΝΟΜΑΤΕΠΩΝΥΜΟ: ΙΩΑΝΝΗΣ ΠΑΓΩΝΗΣ
ΤΙΤΛΟΣ: Growth and characterization of Type I (Straddling gap) and Type II (staggered gap) heterojunctions alignment in thin films for potential photovoltaic applications
ΠΜΣ-Φυσικής   *Τμήμα Φυσικής*   *Πανεπιστήμιο Ιωαννίνων*

.

Chapter 1: Introduction

ΜΕΤΑΠΤΥΧΙΑΚΗ ΔΙΠΛΩΜΑΤΙΚΗ ΕΡΓΑΣΙΑ ΟΝΟΜΑΤΕΠΩΝΥΜΟ: ΙΩΑΝΝΗΣ ΠΑΓΩΝΗΣ
ΤΙΤΛΟΣ: Growth and characterization of Type I (Straddling gap) and Type II (staggered gap) heterojunctions alignment in thin films for potential photovoltaic applications
ΠΜΣ-Φυσικής   Τμήμα Φυσικής   Πανεπιστήμιο Ιωαννίνων

8

1.1 Semiconductor theory

1.1.1 Electronic properties of materials

From the engineering point of view the electric conductivity is the physical quantity referring to the ability of a material to allow for electron transfer. The reciprocal quantity of conductivity is the electric resistivity that refers to the resistance in the flow of the electric current inside a material. Those two properties are fundamental for the study of the electronic abilities of a solid. Depending on the case, we can categorize the materials into groups depending on the amount of electricity that flows.

The first category, in which we have the biggest electron current flow, is the conductors. A conductor allows the flow of charge in one or more directions. The most common conductors are the metals like silver (Ag). The opposite category is known as insulators. In insulators, the electron current inside the material cannot flow freely. Therefore, insulators possess the highest electrical resistivity. Additively, there exists a category of materials with a value of electrical conductivity that falls between the conductors and the insulators, known as semiconductors. Besides the three most fundamental categories, we can make even larger distribution in electrical abilities of a material, like semimetals or superconductors, which will not be explained further. The previously mentioned categorization method can be fully understood by looking in the electronic structure of the materials.
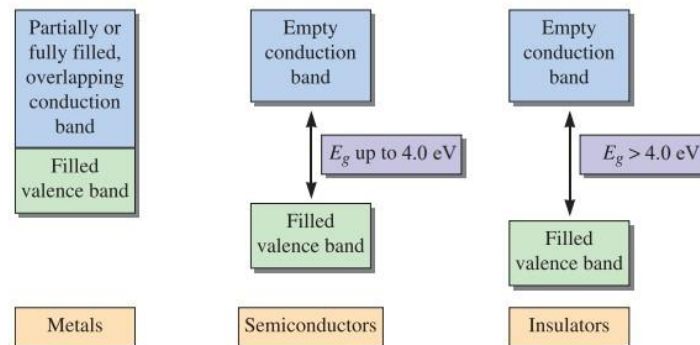
Figure 1 : Schematic of categorizing electrical materials.

The most known way of categorizing the materials for their electric properties is via the electronic structure and the resulting bandgap of a material. As bandgap we define the energy difference between the top of valence band and the bottom of the conduction band, and it is measured in eV units, as the schematic shown in Figure 1 (1)

$$E_g = |E_{VB} - E_{CB}| \qquad (1.1)$$

In condensed matter physics, the bandgap is defined as the range of energy states in which no electrons can exist. The electronic bands that contribute with electrons in the electronic conductivity are in the conduction band as shown in Figure 2 (1). Thus, the bandgap can also be defined as the necessary energy required for promoting electrons from the valence to conducting band.

Figure 2 : A schematic that explains the bandgaps between the electronic states in a configuration.

1.1.2 Semiconductor Physics

As we already mentioned, a semiconductor is a material which is characterized by a bandgap energy level lower than 4eV and it attains values of electrical conductivity between the conductors and the insulators. They obey in the Fermi-Dirac statistics since the electrons which is the most important part in understandin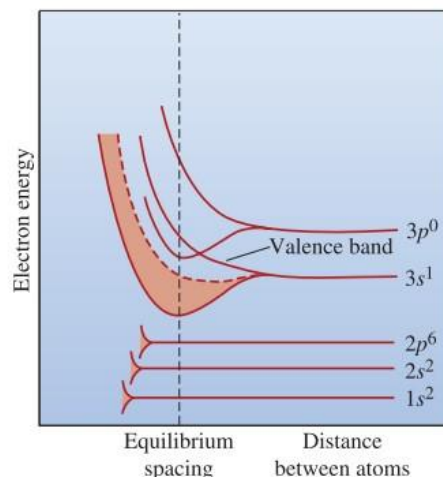g their mechanisms are Fermions (particle with spin equal to 1/2). In semiconductors (insulators as well) the Fermi energy is between the energies of the conducting and valence bands. The general relationship of the Fermi distribution is given by:

$$F(\varepsilon) = \frac{1}{e^{\beta(\varepsilon - \varepsilon_F)} + 1} \qquad (1.2)$$

Where $\beta \equiv k_B T$, and k_B is the Boltzmann constant. Since it can be implied that the distribution is symmetric around E_F it can be easily extracted that $\varepsilon_F = \varepsilon_V - \frac{\varepsilon_{bg}}{2}$ (1.3)

By applying the Grand Canonical Ensemble, the average Fermion number for a certain volume can be defined as:

$$\bar{n_\iota} = \frac{1}{e^{(\varepsilon_i - \mu)/k_B T} + 1} \qquad (1.4)$$

This relationship is identical with (1.2) with the replacement of the Fermi energy with the chemical potential of the system, a quantity equal under certain circumstances and is demonstrated in Figure 3 (2). Since the Fermi energy is only defined in the absolute zero it can be equalized with the chemical potential. This is the reason that the conducting bands of the semiconductors are empty at T=0. Hence, for systems which contain multiple semiconducting materials we expect the Fermi energy to be constant.

ΜΕΤΑΠΤΥΧΙΑΚΗ ΔΙΠΛΩΜΑΤΙΚΗ ΕΡΓΑΣΙΑ ΟΝΟΜΑΤΕΠΩΝΥΜΟ: ΙΩΑΝΝΗΣ ΠΑΓΩΝΗΣ
ΤΙΤΛΟΣ: Growth and characterization of Type I (Straddling gap) and Type II (staggered gap) heterojunctions alignment in thin films for potential photovoltaic applications
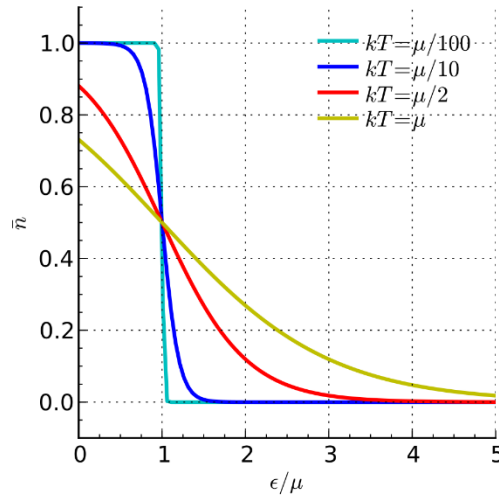*ΠΜΣ-Φυσικής*   *Τμήμα Φυσικής*   *Πανεπιστήμιο Ιωαννίνων*

Figure 3: The energy dependence in Fermi-Dirac statistics.

Semiconductor theory in the last decades has evolved rapidly. One very important property of semiconductors that needs to be mentioned is doping. As doping is defined the small amount of foreign material added to the semiconductor to alter its physical properties (e.g. magnetic, electric, optical). Semiconductor materials whether they are pure or doped, they can be categorized into two major categories, intrinsic semiconductors, and extrinsic semiconductors.

An intrinsic semiconductor is a material without any substances mixed with the crystal, like Germanium (Ge) or Silicon (Si). Their Fermi level is positioned in the middle between the conducting and valence bands, since the number of holes is equal to the number of electrons. When we add extra substances or impurities in the intrinsic semiconductor, we create the extrinsic ones by a physical process called doping (3).

The extrinsic semiconductors are the most used in the electronics industry because of their wide range of applications. They can also be divided into two different categories depending on the minority carriers (electrons and holes). We have a p-type extrinsic semiconductor when we have excess of holes in the material and an n-type where we have more electrons instead. The Fermi levels of extrinsic semiconductors are positioned close to the conducting or valence band, depending on the doping type. For a group IV semiconductor like Si (4 valence electrons in its structure) we can have two basic cases of doping. The first case is the doping with a material from group V like Phosphorus or Antimony. In this case the new material is called a donor because it possesses more electrons compared to the host and as a result an n type semiconductor is created. With the same logic if the dopant is from group III like Boron or Aluminum it's called acceptor, resulting into a p type semiconductor. A representation of doping is shown in Figure 4 (4).
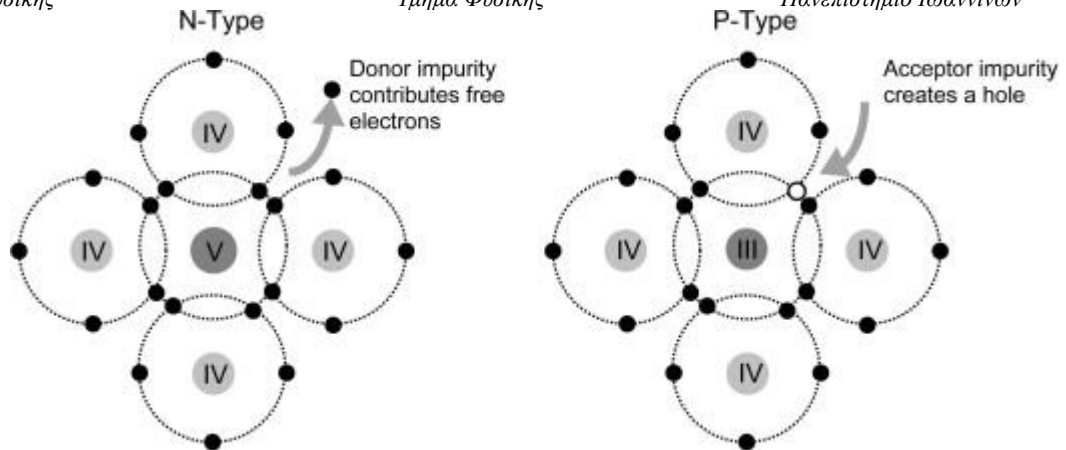
Figure 4 : Extrinsic semiconductor creation by doping foreign elements in Si.

Besides the metalloids, which have a semiconducting nature, oxidation, nitridation, etc can also create bandgaps in the materials and infuse them with interesting properties like the case of Aluminum Nitride (5) (AlN). The combination of two or more different types of extrinsic semiconductors or even the addition of metals or insulators, results in the creation of many different types of electronic devices like diodes, transistors, capacitors etc. The most fundamental type is the combination of two metals or semiconductors with the creation of a junction, which is the birth product of the interface between the materials.

1.1.3 I-V Characteristics

One of the simplest devices that can be created by the interface between a p and an n-type semiconductor is the diodes. The side of the diode with the excess holes (p-side) is called the anode and the one with the excess of electrons (n-side) is called cathode. Diodes are one of the fundamental electronics for the creation of electronic circuits. The performance of a diode or an electronic device in general is the most important part for creating a suitable device. Electronic devices like diodes have special graphs/curves, the I-V characteristics that represent the electric current that flows in a device and its corresponding supply of voltage. For a p-n diode the I-V curve characteristic has the form shown in the Figure 5 (6) and is has two characteristic regions, the forward and the reverse. The I-V curve obeys the following relationship known as Schottky equation:

$$I_D = I_S[\exp{(\frac{V_D}{nV_T}} - 1)] \qquad (1.5)$$

Where I_D is the forward bias current, I_S is the reverse bias current and V_T is the thermal voltage: $V_T = \frac{kT_k}{q}$ $\qquad (1.6)$
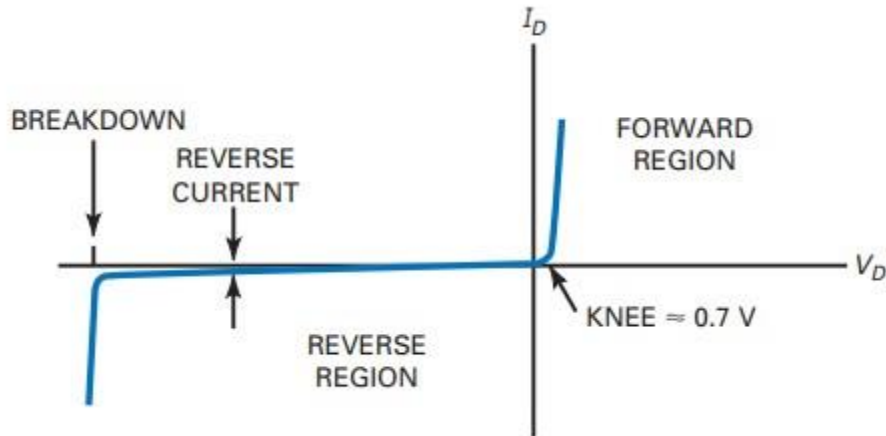
Figure 5: The I-V curve for a p-n diode circuit.

In the forward bias condition (forward region) the positive voltage is applied to the p-type material of the diode and the negative voltage to the n-type material (7). The charge carriers (electrons, holes) will recombine with the free ions resulting into a positive polarization and an increase in the current of the device. In the forward bias, after a certain amount of positive voltage the current in the diode increases rapidly; this current value is known as knee voltage, its value depends on the material and for a Si diode it is 0.7 Volts.

Meanwhile if the positive potential will supply the n-type and the negative potential supplies the p-type, the reverse effect takes places, an effect known as the reverse bias. The region in this phenomenon takes effect is the reverse region of the I-V curve. The ions in this case will be uncovered from the charge carriers of the semiconductors. The gradual increase of the voltage in the reverse polarization region the velocity of the minority carriers will increase as well. The ionization process that will occur from the release of additional charge carriers will combine their contribution in the establishment of an avalanche current. This current will result in the creation of a breakdown phenomenon in the circuit.

The characteristic I-V curves from device to device have significant differences, Figure 6. Depending on physical properties like the resistivity or the charge carriers' concentrations the I-V characteristic can obey a different form compared to the diodes. For example, the curves of a resistor with a small resistance (or large) will follow a linear relationship obeying Ohm's Law. Also, the number of p or n type semiconductors will surely result in a different characteristic. The study of the electrical characterization of the devices is crucial for the modeling of newly utilized circuits based on these devices.
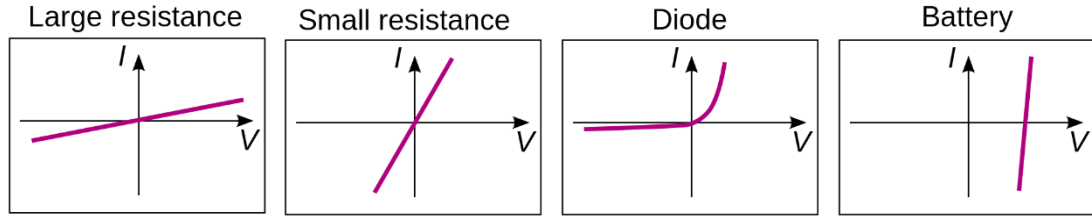
ΜΕΤΑΠΤΥΧΙΑΚΗ ΔΙΠΛΩΜΑΤΙΚΗ ΕΡΓΑΣΙΑ ΟΝΟΜΑΤΕΠΩΝΥΜΟ: ΙΩΑΝΝΗΣ ΠΑΓΩΝΗΣ
ΤΙΤΛΟΣ: Growth and characterization of Type I (Straddling gap) and Type II (staggered gap) heterojunctions
alignment in thin films for potential photovoltaic applications
ΠΜΣ-Φυσικής   *Τμήμα Φυσικής*   *Πανεπιστήμιο Ιωαννίνων*

Figure 6: I-V characteristics for four different devices: Resistor with large resistance, resistor with small resistance, diode, battery.

1.1.4 Semiconductor Homojunctions and Heterojunctions

The semiconductor materials can be combined for creating systems that attain combined properties, forming the junctions. There are two basic junctions which occur from two semiconductors, the homojunctions and the heterojunctions. As homojunction we can name the interface that occurs between layers of very similar semiconducting materials. They usually have different doping but identical energy band gaps. The most common case is the p-n junction created from the two doping types of Si. The creation of the p-n Si junction will result in the creation of the first-generation solar cells that will be explained further below. The energy difference between the Fermi energies of a semiconductor will result in a phenomenon called band bending, which is the process in which the electronic structure of the material curves in the energy area of the junction. The reason for the occurrence of the band bending is the equalization between the Fermi energies of each component of the junction. Because of the similarity limitations homojunctions are not so widely studied as the interface phenomenon of heterojunction that will be analyzed thoroughly in the next paragraphs. A representation of the p-n homojunction for a Si diode is shown in Figure 7 (8).
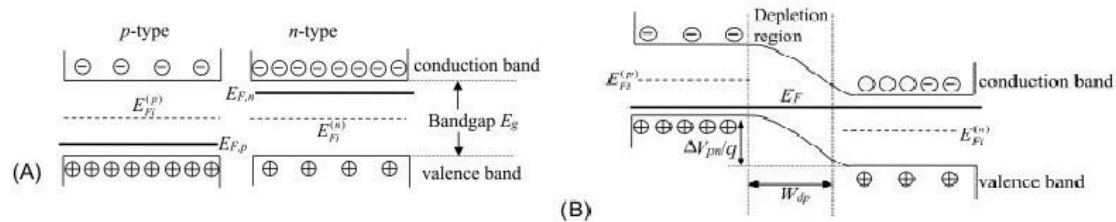

Figure 7 : A schematic illustration of a Si p-n homojunction.

In contrast to the homojunction we have the heterojunction which is referred to the interface between two layers of quite dissimilar semiconducting materials. Those materials usually have quite different absolute values of band gap energy. Therefore, we can have heterojunction independently of the type of the semiconductor. Heterostructures between one p and one n type, two n or p types or even junctions that include intrinsic semiconductors are possible. The interface can also happen with the replacement of one semiconducting material with a metal creating a M-S junction. The combination of many heterojunctions forms an heterostructure, which sometimes is referred just as heterojunction, and it has many applications in electronic like sensors, solar cells, transistors etc.
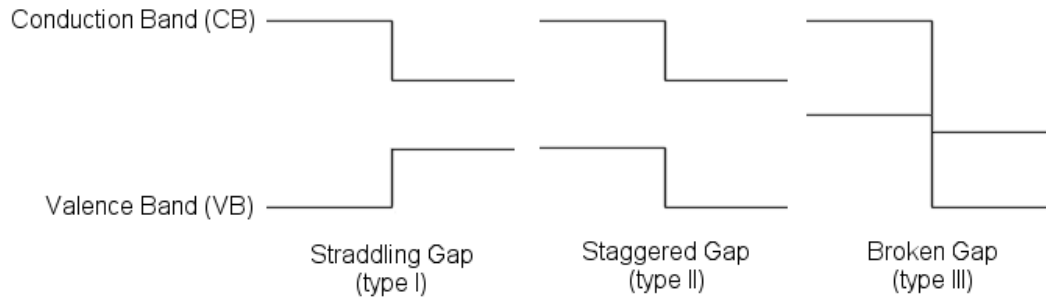
Figure 8: The three types of band alignment in heterostructures.

Heterojunctions, depending on the energy values (bandgap, valance etc.) can be divided into three basic types (Figure 8) (9): (I) Straddling gap type, (II) Staggered gap type, (III) Broken gap type. In the straddling type heterojunctions, the band structure of the one material completely fits inside the energy gap of the other material, since the last one has bigger energy in CB and smaller energy in VB. The heterojunctions that formed from Type II are preferred to those of Type I for photo-applications because of the bigger exciton lifetime (9). Finally, the broken type of gap is similar with the staggered one, but due to the differences in the band energies it offers a charge transfer with a significant change in the driving force.

Since many materials coupled in the bibliography are very unlike, there are many form factors for the determination of the formation of the heterojunction. There are many important fundamental properties like the lattice constants of the interfacing materials, the doping concentrations, and the energy band alignment which describes values like the energies of conducting, valence bands and the electron affinity. The electron affinity is a very important energy value for a semiconductor, and it is defined as the required energy for the excitation of an electron from the conducting band onto the vacuum.

The simplest way of predicting the band alignment of a material is the application of Anderson's rule (10), which is used for the creation of the energy band diagrams for the heterojunction. It is also referred as the electron affinity rule in which we define the latter as the energy required for the transition of one electron into the vacuum level. For heterojunctions including alloys the use of Vegard's law (11) is necessary. The following Figure 9 represents an example of the Anderson's rule for a heterojunction (12).
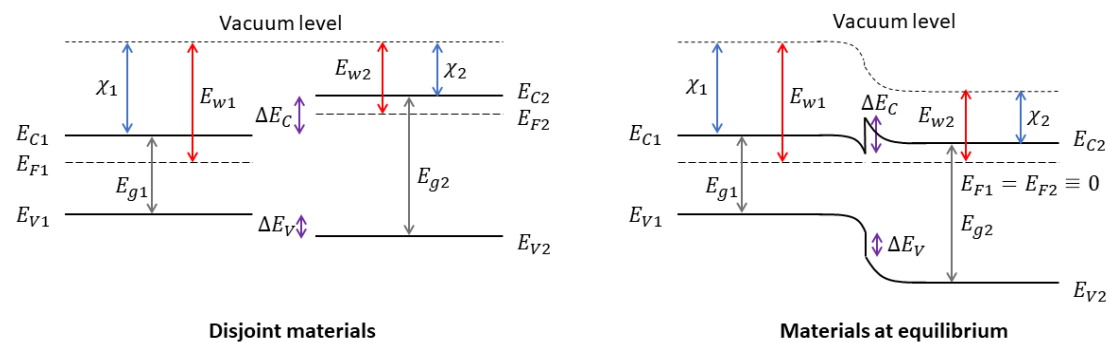

Figure 9: An example of Anderson's rule before and after for a n-N heterojunction.

15

For the schematic creation of the Anderson's rule the most basic step is the alignment of the Fermi energies for ensuring the stability of the new system. In heterojunctions, there are discontinuities in the depletion region because of the different values in electron affinity, which is the necessary amount of energy for extracting an electron from the conduction band to the vacuum those are called band offsets, and they are defined as:

Conduction band offset: $\Delta E_c = \chi_1 - \chi_2$ (1.7)

Valence band offset: $\Delta E_v = \left(\chi_1 + E_{g1}\right) - \left(\chi_2 + E_{g2}\right)$ (1.8)

Where χ is referred to the electron affinity and E_g is the bandgap of the material.

As it can be concluded from the graphic example of the Figure 9, in heterojunctions all the materials have different Fermi energies and thus for the creation of a stable interface they must be equalized. The "new" Fermi energy of the heterojunction must occur from the combination of the two separate ones and hence every other band diagram energy change must be done with the respect of the chemical potential. The physical explanation is the approximation of the Fermi energy as the chemical potential of the system. The chemical potential is a physical quantity that remains interchangeable independently of the state of the system.

Therefore, the newly formed system needs a kind of stability. For the achievement of this energy stability, the two materials should have a kind of discontinuity positive or negative in their merging of their bands. Those discontinuities exist in every type of interface, and they are physically expressed by the conduction and valence band offsets that were mentioned. A very important characteristic found in the occurring potential barriers is the built-in potential which is referred as the energy difference between the work functions of the two semiconductors.

$$V_{bi} = \varphi_2 - \varphi_1 \qquad (1.9)$$

The creation of the heterojunctions can be done with many techniques in many different forms of materials like nanoparticles and thin films. With thin films deposition methods like CVD, thermal evaporation or sputtering we can freely control parameters like the thickness of the interface or the percentages of the components and hence creating multiple heterojunctions in the system.

1.1.5 Metal-Semiconductor Interfaces

In electronics physics a Metal-Semiconductor (MS Junction) is the interface in which we have a close contact between a metal and a semiconduction material, instead of two semiconducting materials (Figure 10).
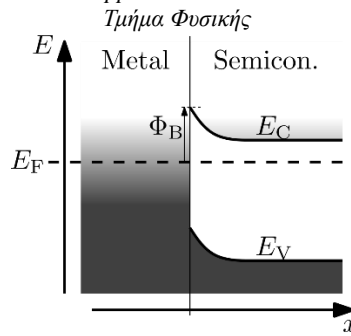
Figure 10 : The MS junction at equilibrium.

The classic MS junction usually has two possible outcomes, the rectifying and the non-rectifying contact. The rectifying contact results in the formation of a Schottky barrier and the other one in an ohmic contact. The last one is useful for the channeling of electrical charge in the transistor, whereas the Schottky contact is useful for the creation of the Schottky diodes and other useful electronics. Schottky diodes can exploit the phenomenon of Schottky barrier, in which a sufficient voltage must be applied for the flow of current. Despite they are looking quite similar, the Schottky barrier of the MS interface and the barrier created in the semiconductor heterostructures are different types of barriers. The discontinuity of the second one is not a Schottky barrier, since it has the characteristic heterojunction quantity, the built-in voltage.

As we can see in Figure 11 (13) we have a total of four cases of junction for a p or n doped semiconductive material. In cases a) and c) the Fermi level of metal has lower energy compared to the semiconductor one. In this case the band alignment attains a negative discontinuity in which voltage must be given for the electrons to be transferred. The phenomenon occurring is the Schottky barrier we mentioned before. The necessary energy is usually given in bibliography as Φ_B and is known as Schottky potential.
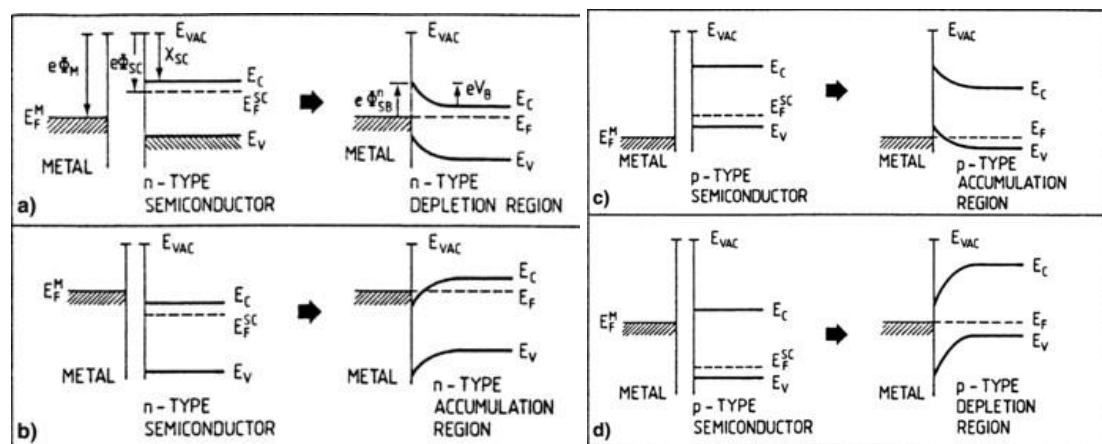

Figure 11 : Metal - Semiconductor junction for p and n types.

Quantitively we can extract a formula which can calculate the necessary energy for the overlapping of the barrier. For the metal its work function can be calculated quite simply by subtracting energy in the vacuum from the Fermi level:

$$\Phi_M = E_{vac} - E_{F,M} \tag{1.10}$$

Similarly for the semiconductor we have:

$$\Phi_S = \chi + E_c - E_{F,S} \tag{1.11}$$

For the n type semiconductor case we can calculate the Schottky potential using the following equation:

$$\Phi_B \equiv \Phi_M - \chi \tag{1.12}$$

Lastly for the case we have a p-type semiconductor in the Schottky barrier, changes should be done in the last equation so the bandgap of the material can also be inserted in the formulas. Therefore, we have:

$$\Phi_B = E_g - \Phi_M + \chi \tag{1.13}$$

Besides the MS junction there is another important device than can be created by inserting an oxide between the band alignment of the metal and the semiconductor. The device that occurs is the MOS capacitor which is the heart of the MOSFET (Metal Oxide Semiconductor Field-Effect Transistor) transistor. The MOS capacitor is almost identical with the MIS capacitor but instead of an oxide, which usually refers to another semiconductor, we have an insulating material with the most known case to be SiO_2. The oxide in the device has the role of the dielectric.

1.1.6 Solar Cells and modern problems

Solar cells technology is one of the most studied for the production of alternative power sources for energy purposes. As solar cell (or photovoltaic) is defined the electronic device which creates electricity through the collection and the conversion of the energy of light. It is based in the photovoltaic effect, a physical phenomenon in which the exposure of a material to light results in the production of current and voltage. Solar cells can operate not only in sunlight, but under artificial light as well and they can be used for extra uses like photodetectors and, electromagnetic radiation.

Figure 12: A crystalline silicon solar cell.

Some solar cells can be created either with a single junction or a multi junction so the mechanism of charge carriers can be exploited accordingly. A proper solar cell is made of semiconductors, such as Si which has been fabricated into a junction (p-n

junction for the case of Si) just like the one from Figure 12. Silicon junctions are usually made with the doping method that was explained before for the creation of the p and n types. When a light photon hits the cell, it is absorbed by the semiconducting material. After the photon absorption electrons from the valence band are transferred to the conduction band producing electron-hole pairs creating the exciton. An exciton is a bound state of a semiconductor in which an electron and a hole are jointed by a Coulomb force. Near the junction the exciton will break, and its components will move to one electrode each, collecting the carriers. In an unconnected solar cell, the carriers are recombined into the exciton. The whole process is repeated into a respectable number of solar cells so a usable amount of electricity can be procured.

For the operation of a solar cell, three basic principles must be taken into consideration. The first principle is the generation of excitons, plasmons or unbound electron-holes pairs. A plasmon can be defined as a quantum of plasma periodic movements. In a material, mostly metals it is used to describe the oscillations of the electrons in the nanoscale. The second principle is the separation of charge carriers of opposite types and as a third basic attributes the charge carriers must be extracted to an external circuit separately as well.

In the first generation of solar cells (or traditional solar cells) the most used material is the crystalline c-Si. The Si one can either be polycrystalline or monocrystalline. The most known type of photovoltaic is the p-n junction silicon solar cell which was described above. Besides the silicon one, because of the high demand of the industry for creating sustainable energy there were developed many different types of solar cells. This led to the development of the next generations of solar cells. The second generation of solar cells is the thin films solar cells. They mostly used at utility-scale power stations, or small systems. The idea behind the use of thin film coatings as a photovoltaic is the reduction of the production costs and materials while the phenomena at nanoscale can take effect. Amorphous silicon (a-Si) thin films solar cells are some of the most utilized cells of the second generation because they are a direct evolution of the traditional ones. Other known types are the cadmium telluride (CdTe) thin films solar cells, gallium arsenide monocrystalline solar cells (GaAs), and CIGS (cooper indium gallium selenide solar cells). Lastly, the third generation of solar cells is the evolution of the second generation of solar cells, and they are still in the research and development phase. They mostly consist of other types of recently developed thin films cells and the evolution of the second-generation ones. The main purpose of the generation is the reduction of the manufacturing process of the thin film photovoltaics. Some types of the new researched materials are perovskites (14), CZTS solar cells (15), quantum dots solar cells (16) etc. Specifically, perovskite solar cells research is contained onto the third generation. In these solar cells a perovskite material -which is a material with the chemical formula $A^{2+}B^{4+}(X^{2-})_3$ - is used in the layer.

Thin film solar cells are the photovoltaics that consist of semiconducting thin film layer (or even multi-layers) onto a substrate. The thicknesses of these types of solar cells vary from some nm up to several μm. As it was mentioned before most of the thin film solar cells belong to the second generation and their further advances in the third. Their creation originates back in the 1970s from Zhores Alverov, the creator of

the GaAs solar cells. In the following decades the technology of the creation of thin films as a renewable energy source have been studied thoroughly.

Compared with the original p-n junction Si solar cells they are quite simpler, lighter, and transparent. In thin films solar cells many of them consist of transparent conducting materials that allow the light to enter inside the material of the photovoltaic. As a result, a lot of the charge carriers are activated resulting in the generation of current that can surpass the amount of the p-n junction ones. Therefore, they could be used easily instead of the first-generation solar cells. The relatively cheap production costs and the easily procuring of the materials make them a quite attractive concept for the replacement of the old-fashioned silicon ones. The other main reason is the increase of a very important physical quantity for the photovoltaic called efficiency. More about the efficiency of solar cells and the challenges of the current era will be explained in the following paragraphs.

Efficiency as an amount is defined as the portion of sunlight energy that can be fully converted into electric current via the photovoltaic effect. It is often described as a percentage number that determines the usefulness of a solar cell as a source for energy production. This important amount has a big dependence on the environment and thus the climate the solar cell is placed. The materials used can also be an important factor for the efficiency as well. For example, when a photovoltaic panel is characterized with a 10% efficiency this means that only the ten percent of the solar energy is fully converted into electric current. Silicon solar cells had their effectiveness increase drastically over the past years and with the creation of multijunction solar cells the efficiency can be maximized up to 34%. This limit is known as the Schockley-Queisser limit (17) for a silicon solar cell under direct sunlight with temperatures not exceeding 300K and it has the form of Figure 13.
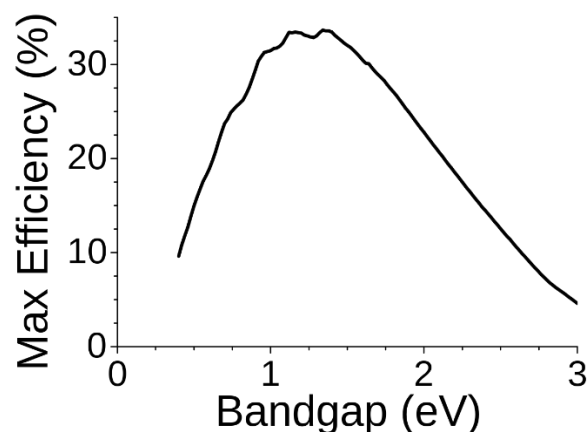

Figure 13: Schockley-Queisser limit of silicon solar cells.

The efficiency of photovoltaics can be affected by various factors ranging from the fabrication process to thermodynamic properties. The material the solar cell is built is one of the most important factors since as it was mentioned the Silicon solar cells have a relatively low limit at 34%, a value not achieved yet. Thin films solar cells, or various complicated, attractive ideas are still trying to improve this limit with the additional benefit of the cost reduction. Furthermore, it is crucial that the placement of

the solar cells to be done in areas brimming with sunlight for increasing the absorption of the sun's rays. The reflectance (effectiveness in reflecting radiant energy) of the cell is important as well. Although thin films solar cells are proposed as a great alternative their low thickness preserve a low absorption of direct sunlight. Therefore, in the modern solar cells reflectivity is one problem that needs to be considered. Other important aspect for the solar cells efficiency is the separation and the collection of the charge carriers in the semiconducting composite materials. The collection of the maximum charges as possible will gradually increase the efficiency of a solar cell. This is the reason heterojunction solar cells or solar cells with smaller bandgaps are being studied.

Despite all the advances in the photovoltaics industry some problems and challenges still persist. As it was thoroughly explained the relatively low efficiency of the modern solar cells and the high production costs of the mass-produced panels are major drawbacks of their current technology. Also, the maintenance costs with the combination of the low-life expectancy of the current solar cells make them not an attractive alternative energy choice. In this era the creation of economic solar cells with the highest absorption rate possible is still the major challenge of the researchers and the industries. Researchers are delving into innovative materials, advanced manufacturing techniques, and novel designs to push the efficiency boundaries and lifespans further.

1.2 Surface Science and Thin Films

1.2.1 Physics of 2D surfaces

Surface science is one of the most recently developed aspects of solid-state physics and materials science. Its goal is the study of the phenomena of the outer atomic layers of solid materials. As surface of a solid we can define the first atomic layers of a solid, which only consist in two dimensions instead of three because of its thickness. Major differences between the surface and the bulk material are often being observed because of the nature of the surfaces and thus new properties that are not encountered in the solid may appear. In the schematic of Figure 14 the sizes between solids and surfaces are compared. The goal of the science of surfaces is the research and the development of these new abilities and their utilization into the modern technology. The study of surfaces led to many technological achievements in optoelectronics (like semiconductor junctions), in metallurgy, in catalysis, in photovoltaics and in the development of nanostructured materials like thin films.
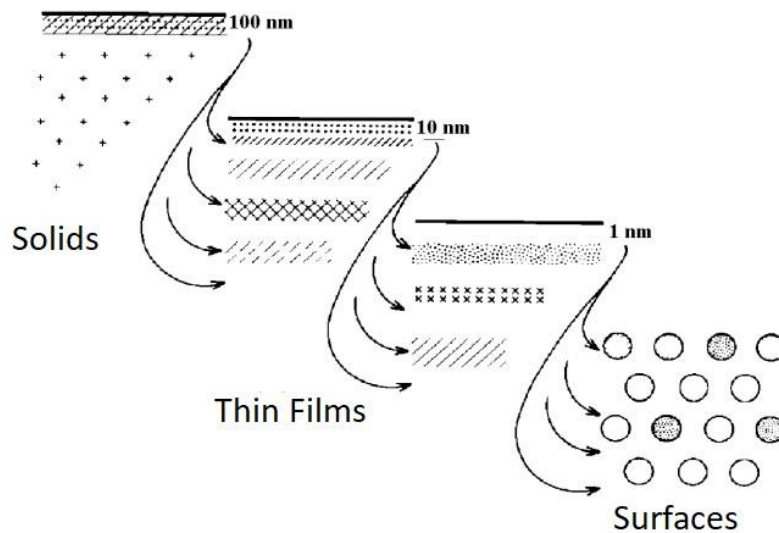

Figure 14 : A quick comparison between bulk materials (solids), thin films and 2D surfaces.

It was mentioned before that a surface is a part of a solid that consists of the first 3-5 atomic layers of a solid. Considering the average size of an atom (about 0.2nm) we expect that the three-dimensional properties would follow similar tendency from the surface ones. Despite the lack of one dimension, surfaces can attain atomic structures with periodicity, like the one of solids. In the two-dimensional space only five different crystal structures exist since the options in the atom combinations become more limited. The five structures are: tetragonal, hexagonal, rectangular, centered rectangular and oblique/parallelogram. The centered rectangular one is like a special case that can also considered as rhombic. A schematic approach and their basic quantities are shown in the following Figure 15 (18).
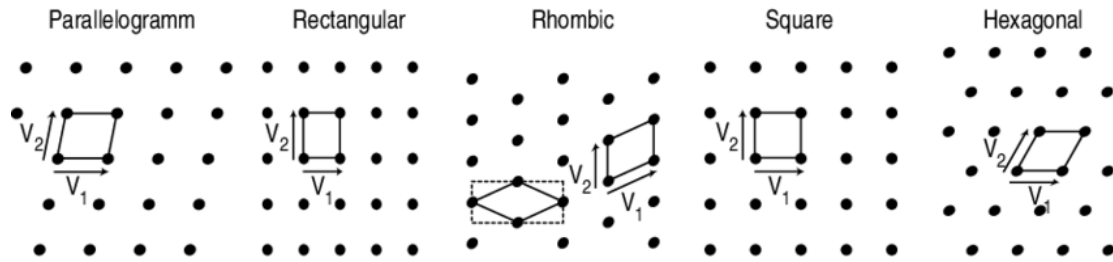
Figure 15 : The five lattice symmetries of a typical 2 dimensional solid.

The five following symmetries are followed by every type of two dimensional solid. Because of their idiomorphs some surfaces may inherit a different (special) structure. A surface follows certain crystal symmetry when their respective parallel crystal levels follow the same type of symmetry. The reason behind the change is symmetry is the phenomenon of reconstructions that happens because some atoms move into different atomic positions, minimizing their energy.

1.2.2 Introduction to Thin Films

As a thin film we can define the type of nanostructured material which is created by its attachment on a solid material or a layer, with a deposition mechanism, which can be physical or chemical. One of the dimensions of the material must be relatively smaller compared to the other two for the new material to be considered as a thin film. Unlike surfaces they are motley in fractal dimensions (2D thin films can also exist). Their thickness varies from some Å to some μm in extreme cases. Thin film technology is fundamental for many technological applications and its excessive study so far led to the development of many new innovative materials with brand new abilities. One breakthrough technology of thin films is the combination of the abilities of many different films in a combined layer or creating many thin film multi-layers in a "sandwich-like" layered formation. The multi-layer format is especially useful in the data storage technologies (19), (20).

Their creation usually is done at temperatures much lower comparing to the melting point of the used material. Because of this, sometimes impurities, defections and metastable phases are created. In the initial growth of the film a significant number of atoms or molecules condense, and they form many clusters or islands. This phenomenon is known as nucleation and growth, and it is the most known method for crystallite creation into a layer of material.

There are three basic ways of thin film growth, development in islands (Volmer – Weber method) or development in layers (Franck-Van der Merwe method). Also, there is the third, special method called Stranski - Krastanov and it occurs from the combination first two methods consisting of both layers and islands. A quick description of the three methods is shown in the following sketch, Figure 16, and they are described analytically:
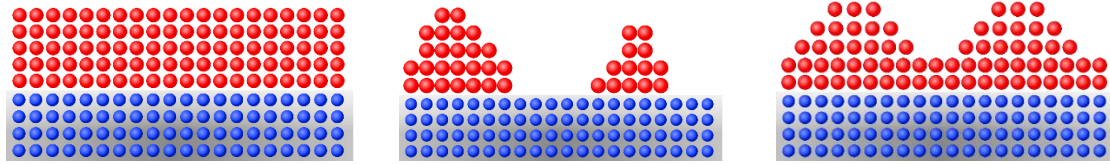
Figure 16 : Layers growth mode VW (left), islands growth mode(center), Stranski-Krastanov mode(right).

i. Development in islands (VW mode): The deposited atoms of this case interact strongly between them and weaker with the surface atoms of the substrate. This results in the creation of islands consisting of atoms of the depositor material. As the time passes, the islands nucleate, grow and coalescence each other.

ii. Development in layers (FM mode): In this method the deposited atoms are going to interact more intense with the atoms of the surface sheet compared with each other. Since, the atoms interact more with the material they will attach, the depositor will create thin homogenous layers of material beyond the substrate. The film we create is considered the ideal, since it requires perfect lattice matching between the atoms of the layer and the substrate. This method is also known as layer-by-layer method since more than one layers can be shaped, and it is most preferred for the creation of the smoothest films possible.

iii. Stranski-Krastanov type development (SK mode): The third development mode is the Stranski-Krastanov type and it acts like a combination of the two others. It is also known as layer-plus-island growth mode. At first the atoms interact more with the substrate layer crating a smooth monolayer film. As the time passes the monolayer will surpass a certain critical thickness. Beyond this point, it will be covered with islands of the atoms of the depositor that evolve according to the VW mode.

1.2.3 Mechanism of growth

During the deposition of thin films, atomic scale processes take place in the surface. Absorption and desorption processes happen when deposited atoms collide with the atoms of the surface of the substrate. Desorption mostly occurs because of possible anomalies of the substrate, usually referring to the lack of smoothness. The absorption phenomena in the film can be described by two different mechanisms, the Physical and the Chemical mechanism of absorption. In the Physical process, we don't have the occurrence of chemical bonds between the absorption atoms of the surface. Therefore, energies less than 0.5eV are created resulting in the creation of Van-Der-Waals weak forces. In the chemical absorption we have the formation of chemical bonds and stronger forces greater than 1eV are being created. Along with the attachment of the atoms in the substrate, phenomena of surface diffusion in which the deposited atoms move along the surface also occurring with a diffusion mean depending on the kinetic energy. The atomistic processes happening during the developed film are shown in the Figure 17 (21).
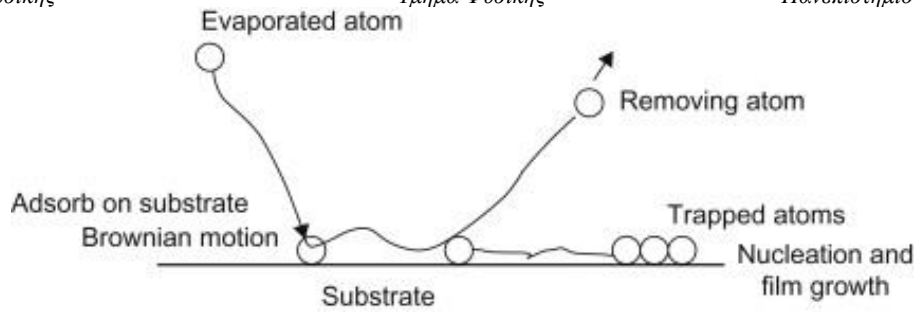
Figure 17: Atomistic processes of thin film growth in the surface.

Whether the material is deposited uniformly in layers, in islands or both it is deeply depended on the type of the material. The substrate can play an important role as well. The development of tensions during the deposition is crucial for the deposition of the atoms and they are related to the minimum energy required for the creation of the film. In the following relationship, Young's relationship describes the required free energies of the substrate (22) and the film for the thin-film formation type is determined by the φ angle between the tensions between the film and the substrate (23):

$$\gamma_S = \gamma_{S-F} + \gamma_F cos\varphi \qquad (1.14)$$

For φ=0, the free surface energy of the substrate is bigger than the energy of the film. In this case the development of the material in layers is preferrable than the islands, since with the angle of the tensions equal to zero there is more freedom of movement for the atoms in the substrate. For φ>0 the free surface energy of the film is bigger and therefore the development in islands is the preferable method. For the Stranski-Krastanov method to happen the lattice constants of the target material and the substrate must be dissimilar. Therefore, in this case the atoms of the film will try to coexist with the upper layer of the substrate initially by layering and after the required tension is achieved in islands.

Depending on the local conditions of pressure and temperature the atoms also can form different nuclei of different crystalline phases of the deposited material. The formed nuclei of the phases can keep growing if the conditions are appropriate. The last referred method is known as nucleation and growth. Nucleation is the first step of the formation of a brand-new phase in a material. It is usually referred as the process that determines the estimation time until the appearance of the new phase. From the thermodynamic scope nucleation is the most common method that describes first-order phase transitions, and they are quite sensitive in the impurities of the thin film.

Nucleation in thin film technology is a phenomenon that occurs beyond the deposition of the evaporated atoms in a substrate. It causes the atomic clusters formation, which create crystalline or even amorphous phase in the deposited film. The nucleation depending on the condition can attain a 2D or 3D formation and it is deeply connected with the Gibbs energy for the nuclei. The determination of the nucleation formation is usually done by studying the Gibbs energy of the system. The Gibbs free energy is a thermodynamic quantity that determines the type of the phase transition. The

25

thermodynamic equation of the First Law of Thermodynamics with respect for the infinitesimal quantity of Gibbs energy is given by the following formula:

$$dG = Vdp - SdT + \sum_i \mu_i \, dN_i \tag{1.15}$$

For a system in equilibrium with constant pressures and temperatures only the number of particles will affect the Gibbs free energy. The macroscopic Gibbs energy therefore will be given by the sum of the products of the chemical potential and the number of particles. It is given as:

$$G = \sum_i \mu_i \cdot N_i \tag{1.16}$$

In order the hypothesis of equilibrium to be totally solidified the first term should be equal to zero, so:

$$\sum_i \mu_i \, dN_i = 0 \tag{1.17}$$

Thus, an increase in the N_i particles of a system will reduce the number of particles of the other systems. Therefore, the chemical potential of all the systems should be identical, $\mu_1 = \mu_2 = \dots = \mu_i = \dots = \mu$. In every system in phase equilibrium all the phases should attain the same chemical potential value. Hence, the phase with the lowest possible chemical potential is the most stable one (Figure 18) (24).

For a state in equilibrium and stable conditions for pressure the entropy can be calculated as:

$$s = -\left(\frac{\partial \mu}{\partial T}\right)_P \tag{1.18}$$

The "s" is known as the entropy per particle and since it is positive quantity the derivative should be negative. As it is shown in Figure 18, the stability of a phase is maximized at the highest entropy (and temperature as well) (24). Since G and S have different sign, by maximizing S the G is minimized which is crucial for the formation of the nuclei in the thin film.
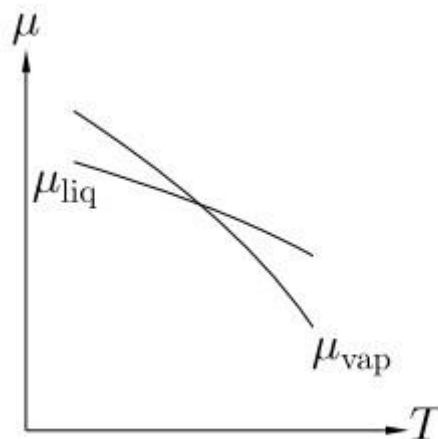

Figure 18: Chemical potential as a function with temperature.

1.2.4 Thin film deposition methods

Until now some basic characteristics of the thin films like their dimensions and their nucleation growth. Next is a very important chapter, the thin film production techniques. The most important techniques for creating thin films and coatings are Vapor Deposition and Thermal Spraying techniques. The first one is divided in three major categories depending on the method of production, PVD, CVD and ALD. Specifically, we have Physical Vapor Deposition (PVD) if the fabrication method follows a physical phenomenon like evaporation and Chemical Vapor Deposition (CVD) if the method follows a chemical reaction. The Atomic Layer Deposition (ALD) method creates thin films by using constantly gas-phase chemical processes. Some fundamental information about every deposition type is shown in Figure 19. For the selection of the best possible deposition technique each time, there are some characteristics about each method we need to know in advance. The most important is the mechanism of the deposited particles (ex. thermal energy and heat transfer, chemical reaction, plasma creation, chemical solution, momentum transfer, flame pyrolysis, high or low energy release.). After the mechanism, the knowledge of the sample and its deposition degree is also important. Atoms, molecules, particles, ions, clusters, we need to prepare a suitable substrate or layer as the film host.

In the thermal spray method instead of atomic, deposition of the particles occurs. The process consists in the production of high energies from flames or plasma with a great deposition rate, usually resulting in the creation of thick films mostly used for coatings. Since flames usually affect the material that will be used for the particles, the substrate of the film has almost no chance from getting damaged.

Property	ALD	CVD	PVD
Growth Rate	0.1-1 nm/min	10-100 nm/min	100 nm – 1 µm/min
Conformality	High; 100% coverage	Medium; Transport-dependent	Low
Materials	Oxides, nitrides, sulfides, metals, elements	Oxides, nitrides, sulfides, metals, elements	Metals, elements, alloys, some oxides/nitrides
Temperature	Wide range	High	Low
Growth Mechanism	Self-limiting	Continuous	Continuous
Directionality	Isotropic	Isotropic	Line-of-sight

Figure 19: Comparison of different thin film deposition methods.

Chemical Vapor Deposition (CVD) is one of the most widely used deposition methods for the creation of solid material thin films. The process concerning the CVD always happens in vacuum conditions and in a typical setup the wafer is exposed to certain types of chemicals named volatile precursors that react with the substrate in order to produce the expected film-coating. The extra volatile by-products are expelled from the system with gas flow as they are not anted in the creation of thin films. The formats CVD depend on the type of chemical reaction that takes place in the vacuum chamber.

Although CVD produces quite reliable thin films, the Physical Vapor Deposition (PVD) methods are rapidly increasing their influence over the thin film research. There are many fundamental reasons for this with the most basic one to be the cost of the creation. PVD methods usually consist of experimental setups much simpler compared to CVD and that fact has major repercussion in the department of industry. Also, the films created by most of the PVD methods are relatively "cleaner" from impurities compared to the CVD ones. One last reason is the freedom of the parameterization of many aspects of the film creation process like thermal, pressure change, different voltage usage etc. PVD methods divide into two major categories: (thermal) evaporation, and sputtering.
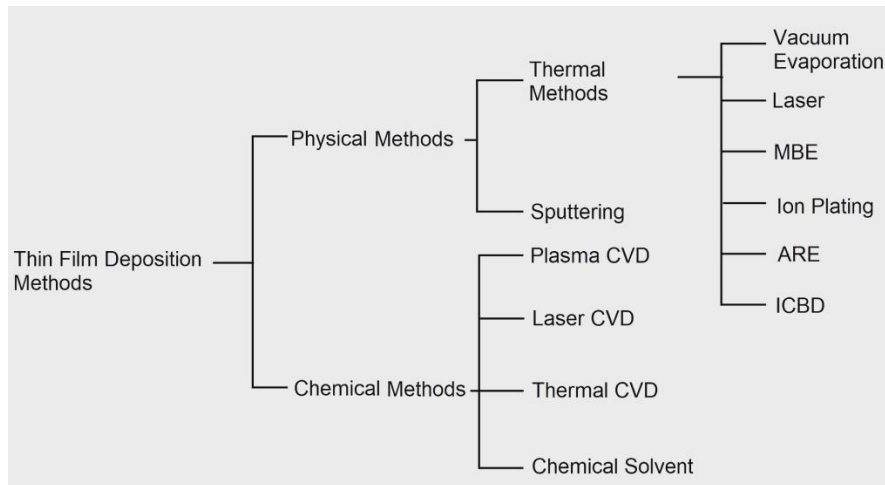

Figure 20 : A schematic of the most basic thin film deposition techniques.

Thin-film development via thermal processes is one of the most widely used deposition methods. The processes take place in high-vacuum conditions for increasing the film cleanness. Therefore, it is rather renewed for the quality of the film it produces with a relatively high deposition rate and low material costs. The number of materials that can vaporize though is quite limited and therefore it has limited uses. Also, the capability of interfering in the process of the deposition and hence the control of the film's properties is also limited.

The deposition with evaporation is determined by two important factors. The first is the Mean Free Path (MFP), which is a physical quantity which describes the average distance in which a moving particle travels before it changes its direction or energy usually by colliding with another particle(s). MFP is the factor that determines the cleanness of the films. High vacuum conditions in the chamber means that there will not be interactions with the atoms of the air, and therefore better-quality films. The other important factor is the Arrival Rate Ratio (ARR) (25) which describes the ratio of the flow of deposited particles with the flow of residual gases in the substrate. We need to control the conditions of the experiment, so the ARR factor is the highest possible, to avoid interactions of the material and residual gases to be attached onto the film. Concluding, it is of high importance the development of high-vacuum chambers with certain distances from the source and the materials to get the best possible result.

The other major category of PVD known as sputter deposition (or sputtering). Sputtering can also be considered as evaporation technique, but it's a quite different one compared to the most thermal methods and therefore it is considered as different category. The whole process is done in high-vacuum chamber conditions. A general schematic describing the most basic CVD and PVD methods is shown at Figure 20.

In the sputtering process, we have the ejection of particles (or atoms) from a target material, which is the source, onto a substrate material such as silicon wafer. The process of sputtering is depicted at Figure 21 (26). The target's surface is eroded by the bombardment of energetic particles and thus we have the ejection of the sputtered ions. Those ions fly from the target, and they are attached in the substrate and the chamber. The gas which is responsible for the erosion of the sputtering target and the flow of the ions in the chamber is usually an inert gas like Ar. The selection of an inert gas is because we usually want to avoid the formation of bonds between the target and the gas.
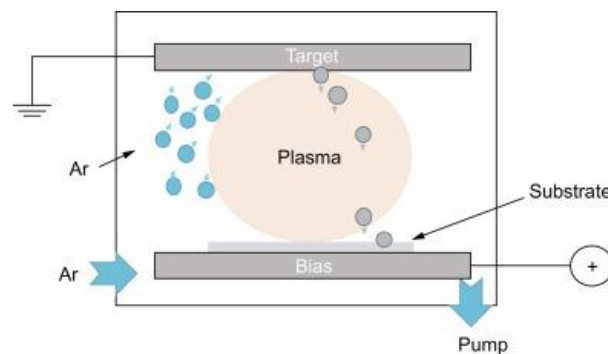

Figure 21 : The physical process of sputter deposition onto the vacuum chamber.

The simplest sputtering method is the DC diode sputtering which consists of a pair of planar electrodes. In the DC sputtering we mostly use metallic targets. One of the two electrodes is one cold cathode which contains the material-target to be deposited, and the other electrode is the anode. The anode is the host for the substrates of the film. In the vacuum chamber an inert gas (usually Argon) is inserted in the chamber and after the dc voltage application a glow discharge is created. Argon is the most frequently used inert gas because of its inventiveness and the relatively low acquisition costs (27). The Argon gas ions (Ar^+) are accelerated from the cathode to the target and then, they head towards the anode creating the thin film.

If instead of a metallic target there is the need of an insulator target (like ZrO_2), DC sputtering cannot create the discharge for the creation of the previously described process. The reason behind this is the creation of a surface charge process from the positive charged ions that collide in the insulating target. This problem is bypassed with the use of a RF diode sputtering (radio frequency sputtering) in the insulator target. Each RF source is characterized by a radio frequency which physically is the oscillation rate of the alternating current (AC). The frequency range varies from ≈30KHz and up to 300GHz. In RF sputtering the atoms of the insulating target can successfully be deposited in the substrate.

As it was mentioned before, the choice of the inert gas for the bombardment of the material-target was done so the formation of extra bonds can be avoided. Besides inert gases, reactive gases can also be used depending on the preferred properties of the thin film. The sputtering method allows us to freely control the flow of the gases in the chamber. There are many parameters that can be changed, which can make the process a bit complicated, but this allows the user to have freely control over the process. The sputtering process which contains extra reactive gases like (N_2) besides the inert ones is called reactive sputtering and is very useful for the creation of nitrides, etc. Reactive sputtering can be used with both types of voltage (DC or RF).

The most known and versatile method of sputtering is the magnetron sputtering. Magnetron sputtering contains all the other previously methods with the addition of an applied magnetic field in the cathode, which is parallel with the surface of the cathode. In almost all the cases the magnets of the sputtering are placed behind the target so they can alter the direction of the electrons in the plasma. The use of the magnetic field inside the chamber increases the ionization of the electrons, and therefore decrease the electron loses in the rest of the chamber. The reason is that the glow discharges of the electrons are moving within a circular orbit with the center to be directed in such a way so that a close loop is created. Furthermore, the use of magnetron sputtering in the stead of the plain RF/DC sputtering is the smaller voltages during the deposition and hence the protection of the sources from the higher voltages.

The magnetic field can be used in two different ways in order to minimize the electron loses. The first way is using a planar glow diode discharge system in which the electrons have a significant increase in their length of the flow before the collision with the anode. At the same time an applying magnetic field will keep the electrons in their course. The second way is the use of a special device in the chamber called magnetron. The magnetron, in which originates the name of the deposition technique, is a device which keeps the electrons enclosed to the surface of the target for as long as possible and therefore it increases the ionization drastically.

A more complex method is the Ion Beam Sputtering (IBS for short), which can be used for more specific types of materials and can guarantee some of the best possible results. In IBS the thin film is applied to the substrate with the help of an ion source firing the ions onto the target material, Figure 22. The advantage of this technique is the full control over the flow and the energy of the ions inside the chamber. Additively, the angles of the ions coming from the gun can freely change increasing the sputtering yield. This method has significant advantages over the DC-RF methods with the only drawback its complexity and the increasing deposition time. For these reasons, the magnetron sputter deposition is to this day the most frequently used method of sputtering and thin film creation in general.
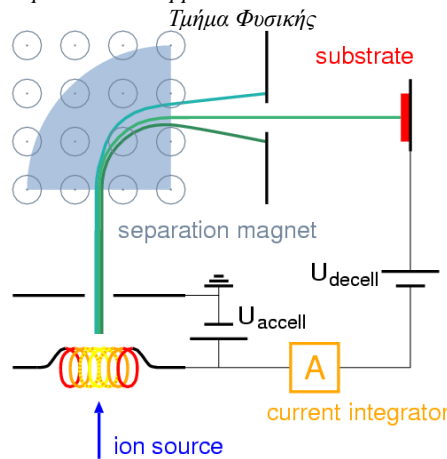
Figure 22: Ion beam sputtering schematic illustration.

1.2.5 Vacuum Physics

Most of the previously mentioned thin film deposition techniques belong to the vacuum sciences and thus they require a clean environment avoiding the atmospheric elements that could create impure final products. Therefore, vacuum conditions are crucial for a successful film growth. The first definition given to the term vacuum was a space clear from other materials. But realistically in physics a fully clear space of matter is not feasible to be achieved. Thus, the first definition had some problems because vacuum is a complex system which is neither inert nor it lacks matter. Therefore, as vacuum we can name a space where its basic pressure it's below the pressure of the atmosphere.

There are many measure units for describing the pressure of a certain volume. They are shown below, in Table 1:

	mbar	torr (mmHg)	pascal (Nm^{-2})	Atmospheres
mbar	1	0.75	100	9.87×10^{-4}
torr (mmHg)	1.33	1	133	1.32×10^{-3}
pascal (Nm^{-2})	10^{-2}	7.5×10^{-3}	1	9.87×10^{-6}

Table 1: The most basic units for measuring the pressure.

In surface physics the manometers, which is the device used for measuring the pressure of a vacuum chamber, mostly have mbar as its physical quantity. Other very important units are torr (mmHg) which is useful for medicine sciences, pascal (Nm^{-2}) which is the official SI measure and the Atmospheres (atm) used in Atmospheric Sciences. Depending on the values of pressure we can divide the vacuum in four basic regions. For units of mbar, we have the following division of areas:

- Low Vacuum (LV): from 1013.25 mbar (atmospheric pressure) to 1-10 mbar
- Medium Vacuum (MV): from 1-10 mbar to 10^{-3} mbar
- High Vacuum (HV): from 10^{-3} mbar to 10^{-7} mbar

- Ultra-High Vacuum (UHV): $<10^{-7}$ mbar

For the creation of the thin films and their study of the characteristics (structure, composition) an appropriate environment in vacuum conditions is necessary. The creation of the film in vacuum condition results in the creation of clean and smooth surfaces that are clean from impurities. Additively, a vacuum environment can minimize the collisions of X-Rays or ions with molecules of the atmosphere, something that will affect the result. That's because the atmosphere components cause extra chemical reactions unnecessary for the thin film. Besides the cleanness and the extra reactions, the vacuum pressure also guarantees the removal of extra impurities which reside in the substrate after it's placement in the chamber like dust or organic compounds. The achievement of the vacuum conditions in the deposition chambers is done by using vacuum pumps of all types.

1.2.6 Vacuum Chambers Technology

As it was mentioned before for a thin film deposition (and not only) chamber to achieve vacuum conditions we have the need of certain devices called vacuum pumps. A vacuum pump is a device that seals a certain volume (e.g. a chamber) for achieving certain pressure by drawing outside the gas particles and blocks the entrance of other external particles. Vacuum pumps can be categorized into three big categories, depending on their built-in function. The categories are the positive displacement pumps, the momentum transfer pumps and the entrapment pumps. Some examples of vacuum pumps used in thin film deposition are depicted in Figure 23.

The positive displacement pumps are pumps that create a partial vacuum condition after use. For the vacuum achievement the pump keeps creating cycles of pumping repeatedly. The device closes the gas in the entrance; it compresses it, and pumps again towards one of the exits in a series of successive cycles until it reaches the low or medium vacuum conditions. These types of pumps are unable to achieve high vacuum conditions and therefore the use of another type may be necessary. All the rotary and mechanical types of pumps belong in this category. The most characteristic pump of this working type is the classical water pump, which operates with the same philosophy even though is not a vacuum pump.

As it was mentioned the positive displacement pumps cannot achieve the high (or more) vacuum conditions which is fundamental for the use of techniques like sputtering. For this reason, there was the development of other types of pumps. The second category of vacuum pumps is the momentum transfer pumps. In these pumps the molecules of the gases of a volume are accelerated from the vacuum side to the exhaust side. At atmospheric pressures these pumps interact differently compared to an already made low or medium vacuum condition. That's because at high pressures the molecules interact each other and push other molecules creating a viscous flow. If the pressure decreases, the distance between molecules will decrease as well. In this case there will be more effective pumping than the first category pumps since the molecules will collide in the walls and not with each other. That means some types of these pumps can be combined with a rotary or mechanical pump for more effective

use. Therefore, with these types of pumps combined the achievement of high or ultra-high vacuum is possible.

The momentum transfer pumps can be divided into two categories, diffusion pumps and turbomolecular pumps. In the diffusion pumps the gas transfer is achieved with the use of high-speed gases from oils, which already reside inside the pump. Sometimes mercury (Hg) vapors are also used for this process. The pump functions by pushing the gases stage by stage with the coexistence of the oil gas of the pump, until it is released from the system. The turbomolecular pumps is quite similar since they both exploit the momentum of the gas molecules. This type of pump consists of a rotor with high-speed curved flaps which coexist with some flaps which stay totally still, of the same type and a stator. The gas molecules gain extra speed and a new direction of movement thanks to the collisions with the rotor.

Figure 23: Alcatel Adixen rotary pump (left). Turbomolecular pump side view (center). Ion pump (right)

The last category is the one of entrapment pumps. This category of pumps can enclose the gases into their sturdy walls, condense them or change their structure like soldering them. The most known type of these pumps is the cryogenic pump. The achievement of very low temperatures which result in the freezing, condensation, and finally their release from the pump. Solid residues may be created after the interactions. Another type of entrapment pump is the ionic pump or sputter-ion pump. The ionic pump uses an electromagnetic field for ionizing the gases of the chamber. The ionized gases can emit a strong electric potential up to 7000Volts. After the process, the ionized gases move onto a solid substrate. Those types of pumps can easily attain the ultra-high vacuum conditions with the combination of rotary and momentum transfer pumps. They are specifically made so they can be working in lower temperatures. Therefore, the use of coolant fluids like liquid nitrogen is crucial, especially for the cryogenic pump. Usually, the liquid nitrogen which is used because of the low costs is working on a closed circuit inside the pump. The nitrogen is keeping the pressure at bay, lowering it gradually while escaped molecules of air cannot manipulate the pressure.

1.3 Basic Elements of Plasma Physics

1.3.1 About Plasma

In the previous chapter details about the sputtering deposition methods were given in depth. The ionization of the material-targets by using reactive or inert gases will result to the etching of the targets atoms and thus in their attachment onto the substrates. During the ionization of the target by the energetic Ar^+ ions, the fourth state of the matter is being formed worldwide known as plasma. As plasma can be defined a gas which contains both charged/ionized and neutral particles, and it is characterized by the appearance of phenomena of both collective behavior and quasi-neutrality. Hence, the statistical behavior of the ionized gases of the sputtering chamber can be fully described by the plasma physics. The fabrication of thin films with plasma creation is not exclusively used in sputtering, since there are other methods like PECVD (Plasma Enhanced CVD) (28) as well. An example of experimental plasma during reactive sputtering (Sn nitrides) is shown at Figure 24.
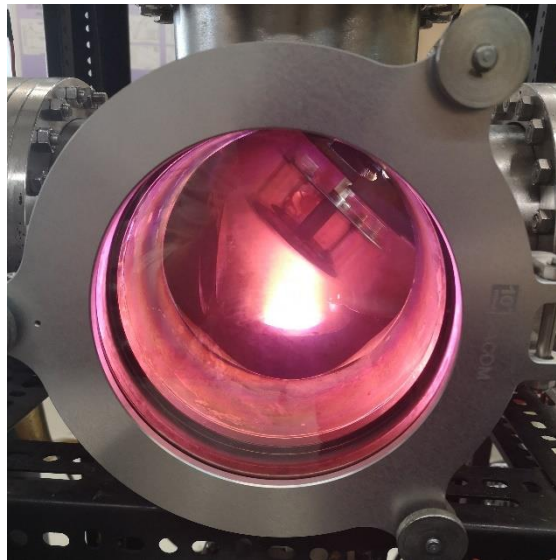
Figure 24: Sn nitride pink colored plasma during magnetron sputtering process.

Plasma as a term of physics was first used in 1923 by Langmuir for describing the states of the gases occurring in electrical discharges experiments. More than the 99% of the matter of the universe like the stars, the ionosphere of the Earth or the Sun consist of plasma. The North-South pole selas is a form of plasma occurring from magnetic phenomena in the ionosphere. Additively, experimental scale plasma has already been created mostly for the purpose of the nuclear fusion. The study of plasma is more complicated compared to a gas because of the Coulomb forces that acting inside the plasma.

1.3.2 Plasma Confinement

One very important utilization of the experimental plasma is the etching, which is referred as all the plasma processes used for the creation of plasma-based devices like semiconductor devices. During the process, the plasma etchers create plasma from

inserted reactive gases into a previously vacuum created chamber. Wafers of materials like silicon are placed onto the etcher for changing their properties. The plasma etching can also be used as a post-growth technique for changing the properties of thin films, like oxidation or nitridation (29), (30). Therefore, the etching process is quite useful to the thin film creation philosophy.

Although plasma etching is an interesting process, because of its Coulombic nature there are occurring crucial issues about its gathering and thus its effective utilization. Plasma has the property to be able to isolate an acting potential and to create a cloud of charge around that potential. The plasma confinement, as the process is called, is the collective phenomena used for maintaining the plasma into a discrete volume for utilizing its properties. Another name for this interesting property is the Debye confinement, and it can be described mathematically by using the one-dimensional Poisson equation with n_i and n_e the ion and electron numeric densities respectively. The Poisson equation reads (31):

$$\nabla^2 \varphi = -4\pi e(n_i(\varphi) - n_e(\varphi)) \tag{1.19}$$

With the hypothesis of big distances, the potential is close to zero. Then, the densities of electrons and ions can be approximated to be equal for simplicity. By using the Fermi-Dirac distribution the densities can be defined as:

$$n_e = n \cdot e^{\frac{e\varphi}{kT}} \ , n_i = n \cdot e^{-\frac{e\varphi}{kT}} \tag{1.20}$$

As it can be observed from the relationships the plasma confinement is deeply affected by the temperature. For very low temperatures, some ions may exit in cloud, resulting into an imperfect confinement.

Replacing the densities into the Poisson equation and applying Taylor's theorem for the equation it attains a final form:

$$\nabla^2 \varphi = 4\pi en(e^{-\frac{e\varphi}{kT}} - 1) \cong 4\pi ne^2 \frac{\varphi}{kT} \tag{1.21}$$

The solution of the equation will give the equation describing the potential of the process:

$$\varphi = \varphi_0 e^{-\frac{x}{\lambda_D}} \tag{1.22}$$

Where as $\lambda_D = \left(\frac{kT}{4\pi ne^2}\right)^{1/2}$,the Debye length of confinement is defined. The Debye length is very important for determining the length of the plasma confinement and it is depending on the electron density.

1.3.3 Types of plasma

As it was mentioned in the previous paragraphs, plasma can either exist naturally in the space (ex. from the Sun) or it can be created in experimental lab scale. As the following Figure 25 implies plasma can generally exist in many different forms depending on different factors like the number density of the electrons of the gas, the

temperature, the existence of magnetic fields, etc. The plasma density in high pressure arcs can surpass the values of 10^{18}cm^{-3} while in the experiments of energy created from nuclear fusion can generate heat more than 10^4eV.
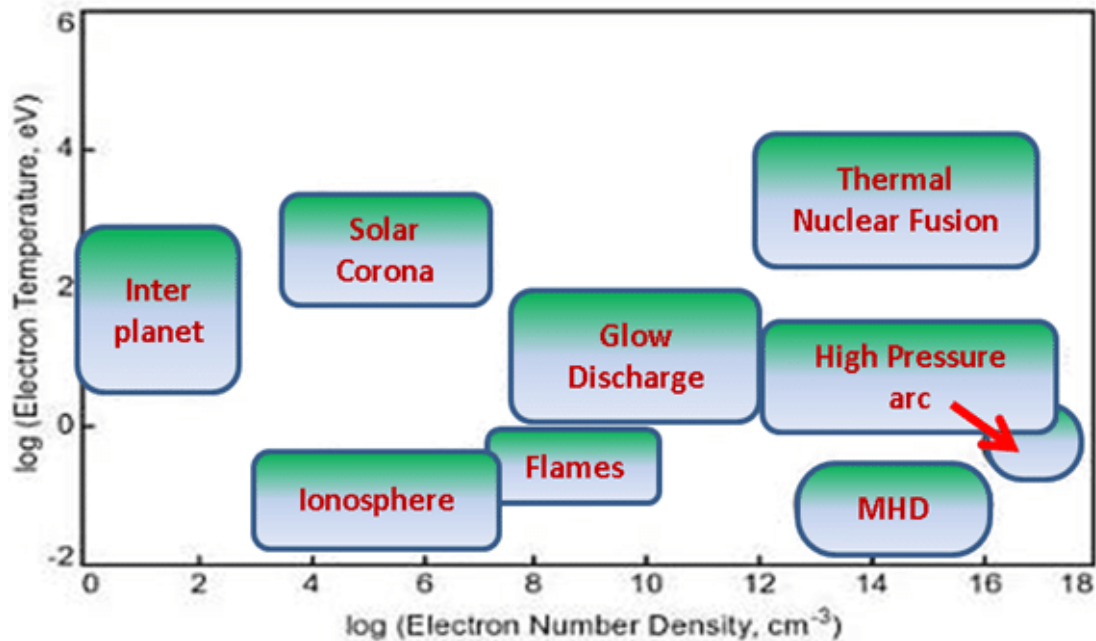

Figure 25: A schematic of types of plasma from different electron energies and densities.

There are many classifications of plasma. For example, categorization based on the degree of ionization. The degree of ionization of plasma is the degree of the number of charged particles divided by the total number of particles (charged and neutral). If n+ refers to the charged particles and n to the neutral, then it if defined as:

$$a = \frac{n^+}{n^+ + n} \tag{1.23}$$

The classification of plasma according to the degree of ionization has two basic categories:

1. Fully ionized plasma: In this type of plasma the degree of ionization is very close to 1. Example of fully ionized plasma is in the core of the Sun.
2. Partially ionized plasma: In this type of plasma the ratio is smaller than 1. The ionosphere or glow discharge tubes can attain this type of plasma.

The most important categorization of plasma though is via the temperature it can produce/the thermal equilibrium occurred in the plasma. By categorizing the plasma with respect to the temperature, three different categories can be mentioned.

1. Plasma in total thermal equilibrium
2. Plasma in local thermal equilibrium
3. Non-equilibrium thermal plasma

For the magnetron sputtering process the important type of plasma which is created in discharge tubes is the cold plasma. Specific details about the cold plasma will be analyzed in the next paragraphs.

1.3.4 Cold Plasma for sputtering

Plasma, which is characterized from total lack of thermodynamic equilibrium, even in local scale is known as cold plasma. In the cold plasma the electron temperature is many times bigger compared to the ions/neutrals temperature and hence the electrons heating can attain temperatures surpassing 10^4 degrees Celsius like the case of a fluorescent lamp with a reactive vaporized gas. While the electrons are surpassing those temperatures, the ions are still at room temperature. In the case of the fluorescent lamp the selective electron-only heating enables the user to be able to touch the bulb even while operating.

Cold plasma can be experimentally created and even utilized for commercial uses. For sputtering techniques, the cold plasma is crucial for the deposition of thin films while maintaining an operational chamber temperature low. The heating of electrons will create plasma of the material target with the essential contribution of the ionized Ar^+ gas. For the ejection of the particles the Ar^+ gas is supplied under a certain voltage to orient them to the vacuum chamber. Another emerging technology of cold plasma utilization with the sputtering technique is the cold plasma packaging in the food industry (32). The deposition of films of biologically based materials is an attractive alternative for decreasing the use of plastics for food packaging. This application has several positive effects like the cost reduction and environmental protection.

1.4 Aim of this Thesis

Technology regarding the utilization of the thin films properties has evolved rapidly over the recent years. To this matter we developed two materials systems one with its oxides forming heterojunction band alignment of Type I (Straddling gap) and one with band alignment of Type II (Staggered gap). For this work we used a two-step growth procedure consisting of a magnetron sputtering deposition and oxidation in oxygen plasma conditions. For the Type II heterojunction we selected the Sn oxides thin films that are formed upon oxidation of the metallic Sn buffer layer. The system which forms the Type I heterojunction oxides was a Zr-Ti-Cu alloy that was oxidized from its respective metallic glass used as precursor layer. The aim of this thesis is the creation of semiconductor heterojunction interfaces and the study of their potential utilization for solar cells, photocatalysis or sensing applications. Additionally, we want to confirm the fact that the heterojunctions belonging in Type II are more suitable from those of Type I for these applications because of the exciton recombination.

Chapter 2: Materials and Methods

2.1 Materials

2.1.1 About Tin

Tin (or Sn its chemical symbol) is a silver-colored metallic element (Figure 26), and its name originates from its Latin word, Stannum. It's rumored to originate from the Stone Age (3000BC) when studies of polymetallic ores from this era, shown some different properties from the expected cooper ores. Back in the Stone Age the combination of cooper, tin and other metals made it a high demanded material because of its metallic properties. Despite its metallic nature, tin is quite soft and brittle and hence it can permanently change its shape by hand. In the latter eras tin became one of the most used materials for the creation of alloys. The first tin alloy which originates back in Stone Age is bronze, which is a mixture of 1/8 tin and 7/8 cooper. Since then, many different alloys were created with the most famous to be pewter, which consists of Sn, Sb, Cu, Bi and sometimes Ag.
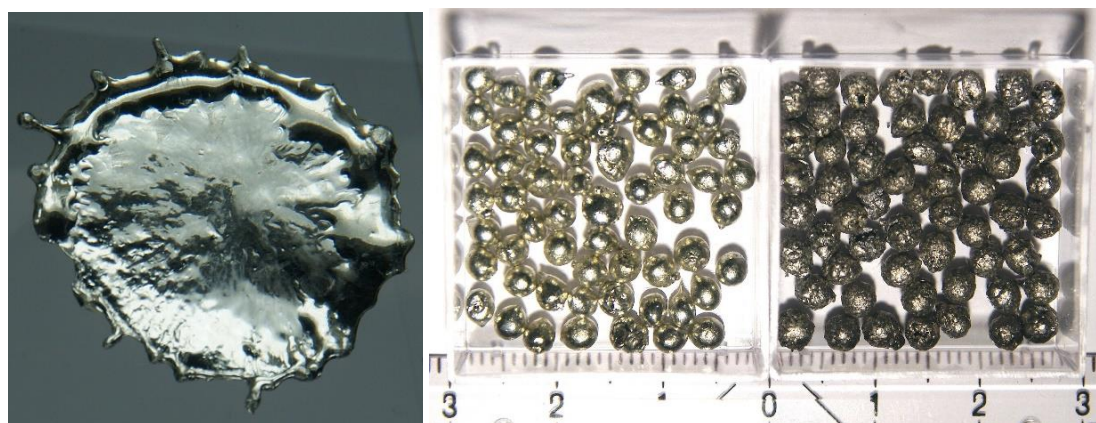
Figure 26: A droplet of solidified tin(left), 99%purity tin sample of its two allotropes(right).

It has an atomic number of Z=50 and it belongs in the group 14 of the periodic table of elements. The electronic configuration is $[Kr]4d^{10}5s^25p^2$. Metallic tin in bulk form cannot oxidize easily in the air, despite having the lowest melting point in group 14 at ≈230ºC. Tin nanoparticles, especially the ones with diameter smaller than 20nm have an even lower melting point by about 60˚C. As metal it consists of four allotropes (different metallic forms) which are α-Sn, β-Sn, γ-Sn, σ-Sn. The two first are the most basic ones, since the other two can be created at temperatures above 160˚ and pressures above GPa. Among these allotropes β-Sn (33) (white tin) is the most common one, since it can be stable even at room temperatures. It is metallic and it has a body-centered tetragonal structure (BCT structure). The other common form, α-tin (34) (gray tin) is non-metallic, and it is created at temperatures below 14˚C. The critical temperature of transformation is 13.2 ˚C, which can change by impurities. It can also occur by exposing the white tin in cold environments. Despite having a face-centered diamond cubic structure it is relatively brittle and it is only used in certain semiconductor applications.

2.1.2 Tin Oxides

Tin has many oxidation states with the 4+ state to be the most stable one, since metallic tin has 4 electrons in its outer shell. The 2+ state can be found as well but it's less stable because the metal's behavior tends to release two more electrons to reach the full filled configuration. The same happens with the 3+ state as well, a state which cannot be easily achieved by regular oxidation means. Therefore, the main oxidation states are 4+ and 2+, which result to the two native oxides of metallic tin, SnO_2 and SnO.

The most stable state when it is combined with oxygen ions is the Tin (IV) oxide (SnO_2). The mineral form of the main tin oxide is called cassiterite. Its empirical name is stannic oxide, and its main crystal structure is the rutile tetragonal structure (Figure 27). Under certain circumstances like high temperature, relatively high pressures, or a combination of both its atoms can move differently and therefore to form another structure. Some structures like the orthorhombic can also be formed in those extreme conditions with different properties. In bulk powder form it has a characteristic white color (like titanium dioxide) and it's insoluble in water. As for its physical properties it has diamagnetic nature and it is an n-type semiconductor with optical band gap around 3-3.5eV (35), (36).

The stannous or Tin (II) oxide (SnO) is the other native oxide of tin, and its main crystal structure is tetragonal as well (a-SnO). Rarely it can be encountered in nature as a component in the mineral romarchite. It has a characteristic blue-black form and can also be produced chemically. Additively, it has a metastable form that is characterized by a reddish color. The optical bandgap of the material varies from 2.5-3eV (direct gap) (37) and it's a p-type semiconducting material. Besides the main gap, the SnO thin films may also possesses an indirect band gap (38).
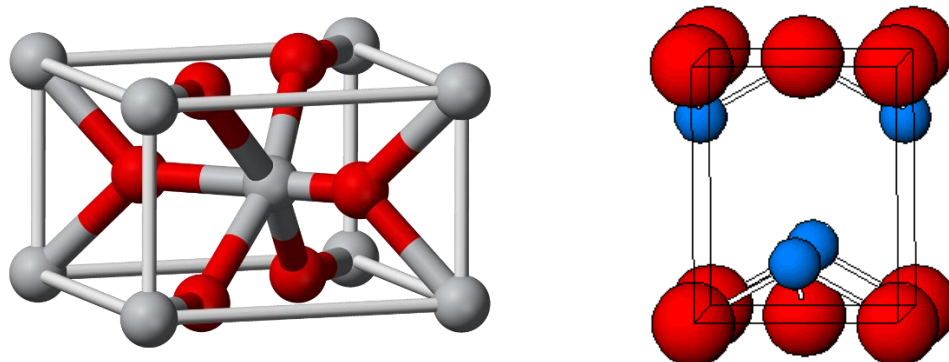
Figure 27: Tetragonal structure stannic oxide(left), tetragonal structure of stannous oxide(right).

The interface of the two main oxides of Sn can result into a p-n type heterostructure, which has the potential to be used into photovoltaic devices (39), an effective photocatalyst (40) , gas sensor (41) or photoresponsible sensor (42). The band alignment of the SnO-SnO_2 heterojunction is shown in the following band diagram of Figure 28 (41).
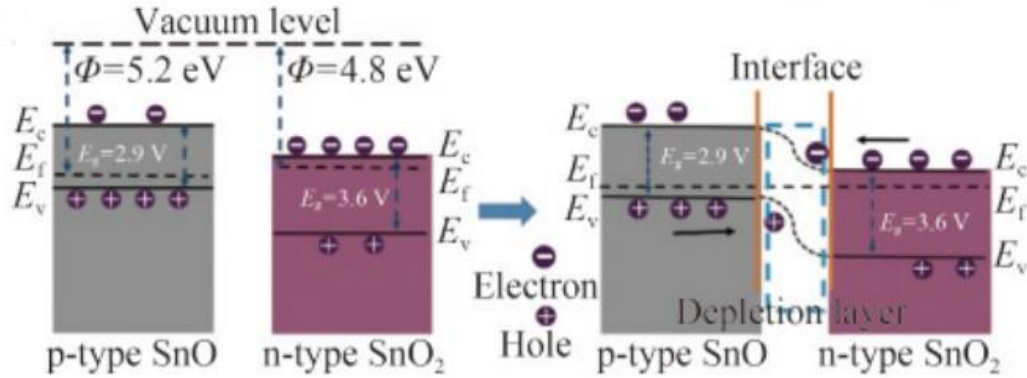
Figure 28: The SnO (p-type) - SnO2 (n-type) heterostructure.

Besides the main oxides, there are many metastable phases that can occur with thermal oxidation or by a chemical reaction. Therefore, between the stannic and the stannous oxide, other oxides of tin like Sn_2O_3, Sn_3O_4 and Sn_5O_6 can occur. One of the most studied cases of metastable tin oxides is the intermediate oxide Sn_3O_4. The intermediate tin oxide Sn_3O_4 is a mixed valence tin oxide which consists of both Sn^{2+} and Sn^{4+} oxidation states. It has the general chemical type $(Sn^{2+})_2Sn^{4+}(O^{2-})_4$, but the lack of the Sn^{3+} oxidizing state makes this oxide to be distinguished from the spinel (and reverse spinel) structure materials like Fe_3O_4. The distinguishment from the spinel class of materials creates an interest as for its crystal structure.

In the beginning there were many confusions regarding the formation of Sn_5O_6 until the proven existence of Sn_3O_4 from F. Lawson (43). Lawson proved the existence of Sn_3O_4 as the intermediate oxide between the two main tin oxides by heating the Sn (II) oxide at temperature reaching up to 1050K. The X-Rays diffraction in the crystallites of the experiments proved the existence of the intimidate oxide with a triclinic (anorthic) crystal structure (Figure 29).
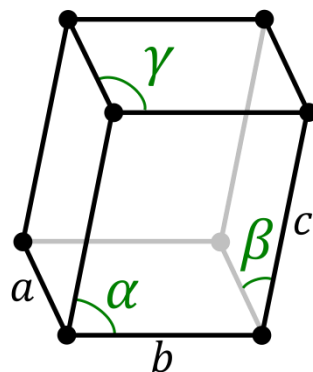
Figure 29: A general triclinic structure unit cell with its parameters.

This triclinic structure as Lawson discovered from his experiments consisted of the following lattice parameters with a≠b≠c and α≠β≠γ for the angles of the structure. Therefore, he found that:

- a (A): 4.8600
- b (A): 5.8800
- c (A): 8.2000
- Alpha (°): 93.0000
- Beta (°): 93.3500
- Gamma (°): 91.0000

The further heating of this metastable oxide will eventually create the Sn (IV) oxide which is the most stable oxide of Sn.

According to Lawson two chemical reactions were necessary. The first is the fast heating of the SnO so SnO_2 won't be formed immediately.

$$4SnO(s) \rightarrow Sn3O4(s) + Sn(l)$$
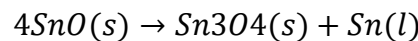
The second reaction is the slow heating of the metastable oxide for the final production of the SnO_2. In both reactions metallic Sn in melted form was procured as a byproduct.

$$Sn3O4(s) \rightarrow 2SnO2(s) + Sn(l)$$
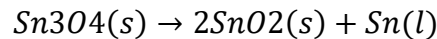
Just like the SnO-SnO_2 heterojunction, the metastable phase of Sn3O4 can also form interfaces with both types of main oxides. The Sn_3O_4 has an experimentally calculated bandgap around 2.2-2.6eV (44), (45) which is relatively lower compared to the main oxides. In general materials containing the Sn^{2+} state have relatively lower bandgaps compared to Sn^{4+} (46). Even though, as a material it is highly recommended as a photocatalyst just like the other tin oxides since the formed levels above the O 2p state make the material suitable for absorption of visible light. The band alignment with the oxides is shown in the Figure 30 (47).
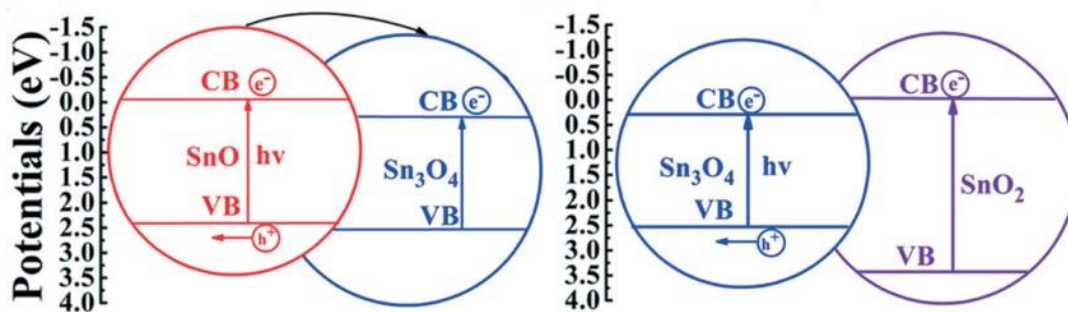
Figure 30: The heterojunction band alignments formed from the interface of Sn3O4 with SnO (left), SnO2 (right).

2.1.3 Transparent Conducting Oxides

The oxides of metals like Sn, In, Cd and Zn are very important oxides in the physics of semiconductors, since at nanoscale depositions they belong to the very small category of materials called Transparent Conducting Oxides (TCOs) (48). Transparent conductors are a group of materials that have a high electric conductivity and simultaneously they are optically transparent (or semi-transparent). The TCOs occur

from the oxidation of those transparent conductors, and they most exist in the form of thin films. Because of their optical transparency they can absorb many electrons. Therefore, they can be used in various optoelectronic applications such as modern thin film solar cells and LEDs (Figure 31).
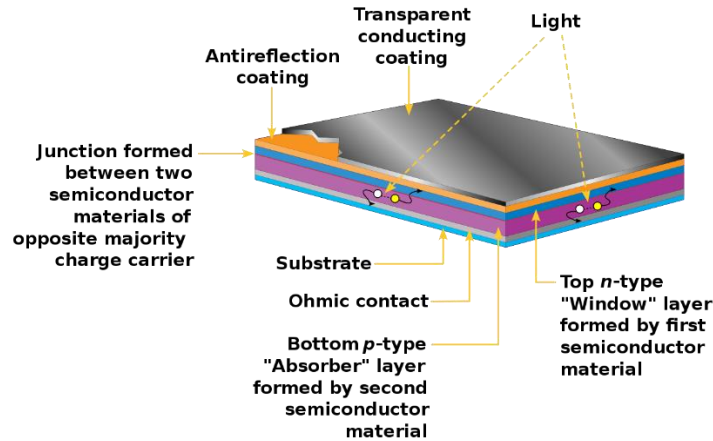

Figure 31: A cross-section image of a TCO thin film solar cell.

The materials in the category of TCOs usually have a wide bandgap (>3eV) (48), and they have high optical transmittance in the range of visible light. As for the metals which are the most suitable to become TCOs, after experiments it has been proved that the oxides of Indium (In), Cadmium (Cd), Gallium (Ga), Zinc (Zn), and Tin (Sn) are the best possible transparent conductors. Indium Tin Oxide (commercially known as ITO) is the most known case (49) and it's mostly used in high quality LEDs or as photovoltaic buffer layer. A cheaper alternative is ZTO (Zinc Tin Oxide) (50), which is also used widely and has similar properties to ITO. The oxides of tin are also used because they are cheap, and they can be produced easily by many deposition techniques.

2.1.4 Zr-Ti-Cu Alloys Metallic Glasses

The metallic glasses (also known as amorphous metals) are a special category of materials that attain a non-crystalline structure like glasses. They are mostly in the form of alloys (two metals or more) and they can be produced by various methods like PVD. As a ternary system we refer to the system that is consisted of three different inorganic compounds. The metallic glasses of three different elements are ternary systems. The major advantage of metallic glasses over the classical silica glasses is that they attain high electrical conductivity since they don't lose their metallic nature. One of the mostly utilized metals in the metallic glass alloys is the Zirconium (29), (30).

Zirconium (Zr) is a lustrous metallic element with a melting point around 1850ºC and electronic configuration of $[Kr]4s^2 5s^2$. It belongs in the same group of transition metals like Titanium (Ti) and Yttrium (Y) and the second in order. Hence, the elemental configuration of Ti is $3d^2 4s^2$. Both materials form the hexagonal closed package (hcp) crystal structure. The hcp structure has a very dense positioning of the

atoms and thus the materials with hcp structure are characterized from big bulk modulus. The materials of the group of Zr are also known about their biocompatibility as coating materials (51).

The addition of other metals in the interface between the Zr and Ti alloys can result in additional benefits with the biocompatibility. Some of the most potent cases are the addition of Cu, Mg or Zn. Cu is a metallic element with atomic number Z=29 with electronic configuration of $[Ar]3d^{10}4s^1$. It has a vast amount of uses in alloys, electric wires, building materials and jewelry. Its crystal structure is the face centered cubic (FCC), Figure 32. The addition of metals like Cu or Zn in the alloys will result in rather improved glass-forming properties (52).
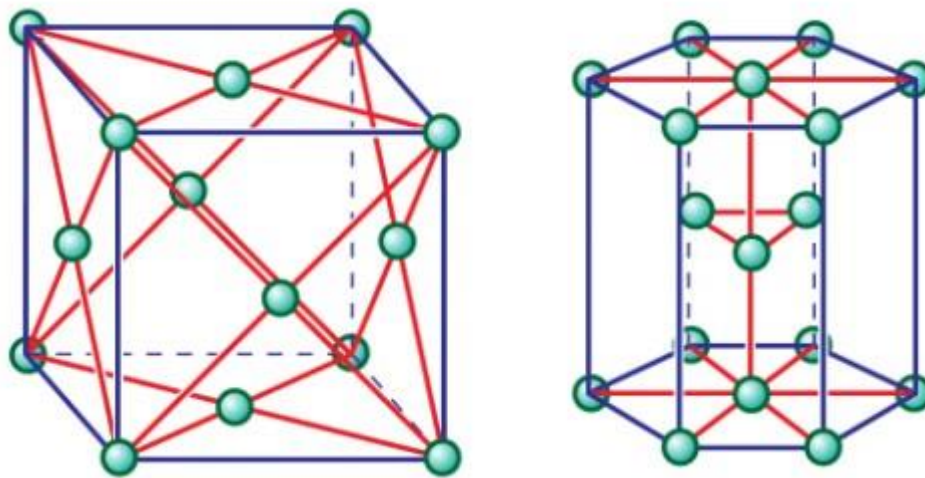
Figure 32 : A schematic of the FCC structure found on Cu (left) and the HCP structure of metallic Zr and Ti (right).

2.1.5 Zr-Ti-Cu Oxides

The oxides formed from oxidation of metallic glasses will form multiple heterojunctions depending on the band alignment and the composition of the elements present. For the Zr-Ti-Cu metallic glasses there are three main oxides formed at conditions close to room temperature. The main oxide of Zr is ZrO_2 (zirconium dioxide or zirconia for short). Its electron state is Zr^{4+} and upon oxidation it attains insulating electrical properties with optical bandgap around 5eV. ZrO_2 at room temperature forms the monoclinic crystal structure (m-ZrO_2), while at higher temperatures the tetragonal (t-ZrO_2) or cubic (c-ZrO_2) structures can also be formed (29). The required temperatures for the forming of t-ZrO_2 exceed the 1100 ºC while for the c-ZrO_2 temperatures between 2350 ºC and 2670 ºC are necessary (53). The three crystals structures are shown in the Figure 33.
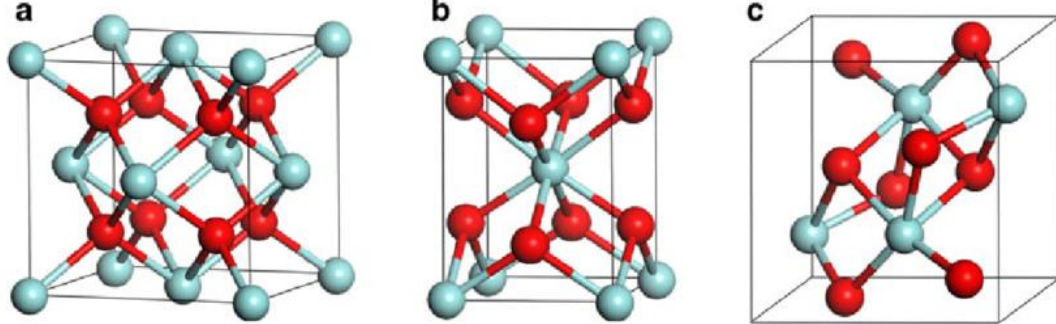
Figure 33: The three crystal structures of ZrO2: a) monoclinic, b) tetragonal and c) cubic.

As for Ti, its main oxide is the TiO_2 (titanium dioxide or titania). It has the electron state of Ti^{4+} like the Zr and its main crystal structure is the tetragonal, in which it crystallized in two different forms: rutile and anatase. Rutile and anatase are both tetragonal crystal structures, but with different space groups and lattice constants. The rutile tetragonal structure is the primary crystal structure, and hence is more stable. Meanwhile anatase is most observed for further process of TiO_2. Besides the rutile and anatase TiO_2 has another one mineral form that crystallizes in the orthorhombic crystal structure, and it is referred as brookite. All the three structures can be observed in a temperature range varying from 300°C to 1100˚C. The crystal structures for the TiO_2 structures are shown in the Figure 34.
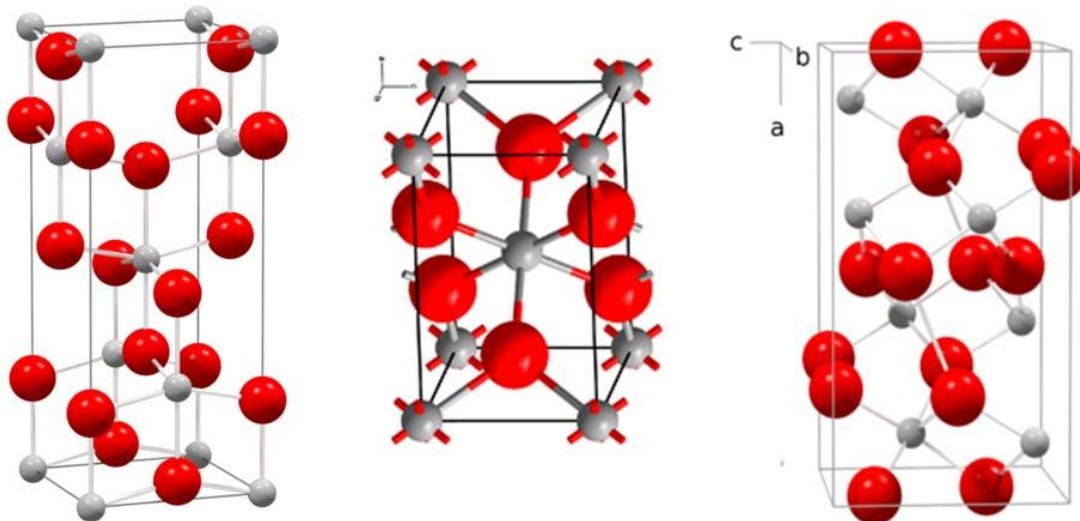
Figure 34: The three crystal structures of TiO2: Anatase (left), Rutile (center) and Brookite (right).

As for its electrical properties TiO_2 is an n-type semiconducting material with bandgap energy varying from 3.0 to 3.3eV depending on the crystal structure. Specifically, for the anatase structure it is ≈3.0eV, for the rutile structure ≈3.2eV and for the brookite ≈3.3eV (54). The three semiconducting crystal structures band alignments (55) are shown at the Figure 35.
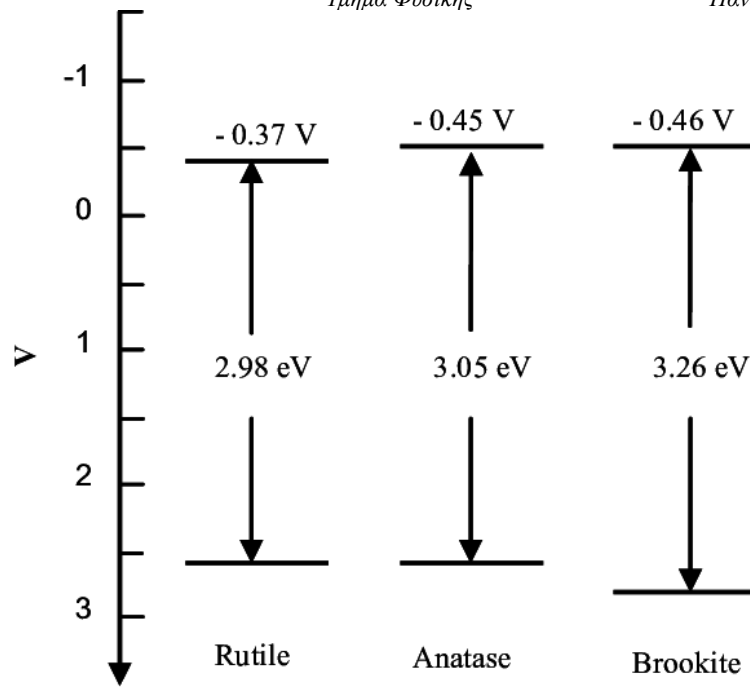
Figure 35: Band alignment of the three TiO$_2$ crystal structures.

As we saw in Chapter 4.4 Cu belongs to different periodic table group and thus different oxidation states will exist. The most common state is the Cu^{2+} that results in the formation of CuO also known as cooper (II) or cuprous oxide. The atoms in the lattice form the monoclinic structure (56), (57). The other main oxide is the Cu$_2$O which is named cooper (I) oxide or cupric oxide. Cu$_2$O just like pure metallic Cu has the FCC crystal structure (58). The Cu$_2$O oxide is formed at 250-320°C upon oxidation of metallic Cu and after the temperatures are exceeding the 350°C it is oxidized further, resulting in the formation of CuO (59). Both two main oxides of Cu are p-type semiconductors with bandgaps of 1.3eV - 1.7eV for CuO and ≈2.0eV – 2.4eV for Cu$_2$O (60) (61).
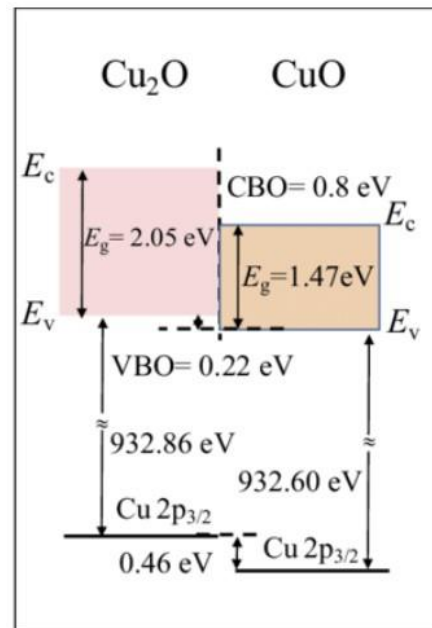
Figure 36: The band alignment of the main Cu oxides.

The oxides of Cu have already been studied for potential same material heterojunctions (62) and their band alignment is represented in Figure 36.

As it was already analyzed in the Sn oxides section the heterojunctions can greatly increase the properties of materials by combining their properties. Not only semiconductors are used for these alignments. Using insulating materials with the combination of semiconductor has already been studied a lot and the transfer of charge carriers is highly possible depending on the interface type (63).

The interfaces between TiO_2 and ZrO_2 has recently caused great interest because of their potential uses as photocatalysts mostly because of the already known properties TiO_2 (64) (65). The heterojunction TiO_2 and ZrO_2 belongs to the Type I category (staggered gap) and their heterojunction band alignment can solve major problems the plain TiO_2 photocatalysts face, like the exciton (electron hole pair) recombination (66). The lifetime of the exciton can greatly be extended by the transfer of charge carriers in the energy bands of ZrO_2. The band alignment between the two oxides is depicted in the Figure 37 (67).
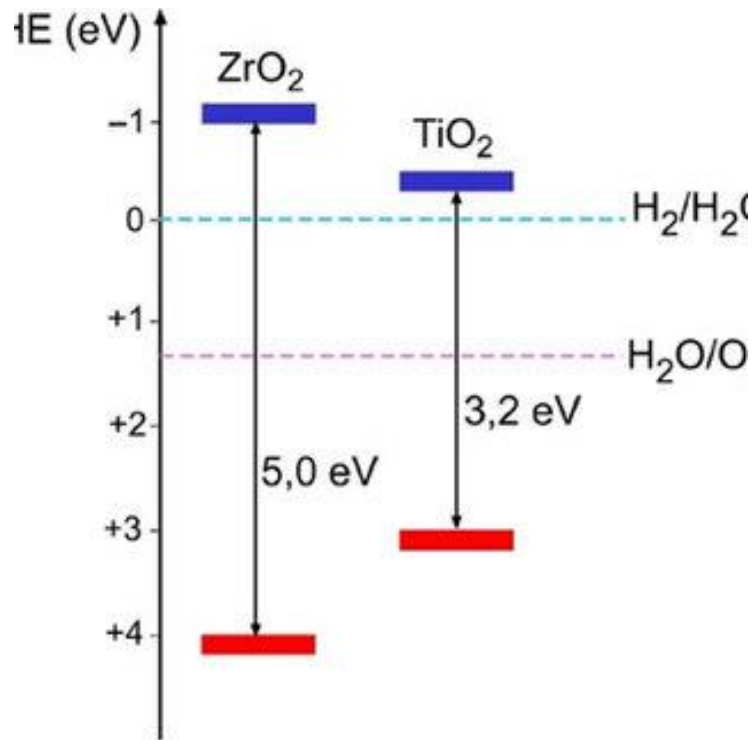
Figure 37: Band alignment between ZrO_2 and TiO_2.

As we mentioned the heterojunction between TiO_2 and ZrO_2 produces some interesting results. The referred system has been further evolved so it can attain even better properties. For this reason, ternary oxides thin films with this heterojunction as a base have been fabricated. One of these systems is the heterojunction between ZrO_2, TiO_2 and SiO_2 and its potential use in photocatalytic dye degradation (68). One promising idea is the combination of ZrO_2 and TiO_2 with the oxides of cooper, and more specifically CuO and Cu_2O. Both systems of ternary oxides (Zr-Ti-Cu oxides) are not thoroughly researched, and they exhibit potential as suitable photo-application systems. The band alignment of CuO with TiO_2 are shown in Figure 38 (69). The Cu_2O-TiO_2 band alignment is of the same type.
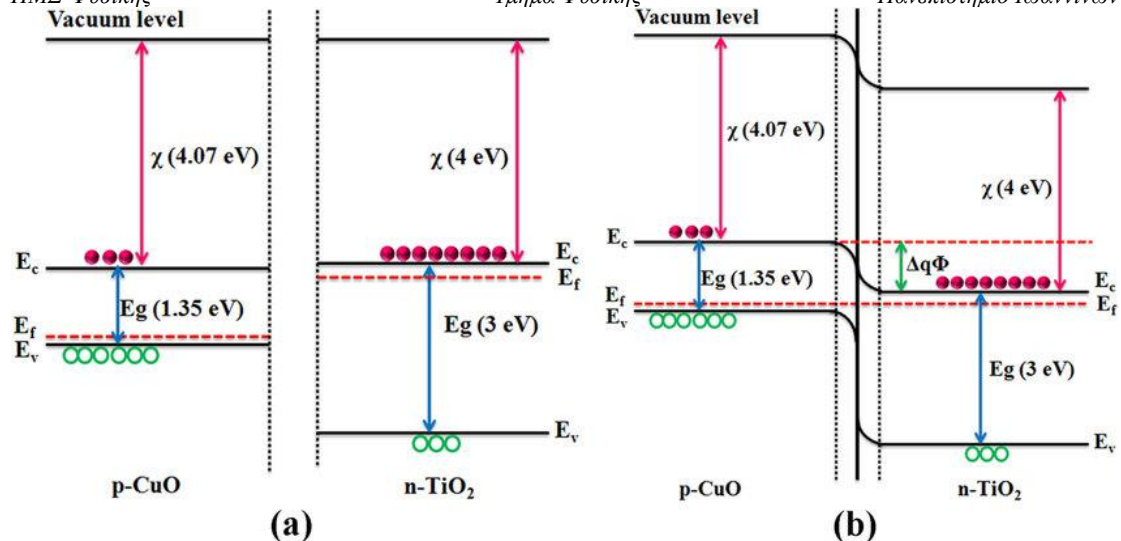
Figure 38: The heterojunction formed between CuO and TiO$_2$.

2.2 Methods

2.2.1 Introduction

For this thesis we choose to study two materials systems each for a heterojunction band alignment type. The first system is a Sn oxides thin film consisted of SnO, SnO$_2$ and Sn$_x$O$_y$. As for the second system we choose to use an oxidized Zr-Ti-Cu metallic glass. The development of these materials systems will follow a two-step procedure of a) growth of a metallic buffer layer by magnetron sputtering b) oxidation of the upper area of the buffer layer via oxygen plasma treatment. This two-step method has already been proposed as an alternative method in recent studies (29) (30) (56). The as-grown thin films were afterwards characterized by means of X-Rays Diffraction for determining their structural properties and by X-Rays Photoelectron Spectroscopy (XPS) as for chemical and compositional characterization. For determining their photovoltaic/photoelectric properties, I-V characteristics and photocurrent I-t measurements were conducted. The experimental details of the techniques are thoroughly expained in the following paragraphs.

2.2.2 Magnetron Sputtering

Back in the theoretical section magnetron sputtering was defined as a thin film physical vapor deposition (PVD) method which uses magnets behind the position of the material-target. Those magnets are arranged in circular arrangement, and they have the purpose of boosting the process of film creation by using magnetic fields to control the behavior of the charged ion particles in the chamber. The magnetic field causes a major increase in the ionization and the redirection of the eroded atoms from the target making easier the deposition onto the substrates. The magnets are positioned in a circular range behind the metallic sputter targets. A magnet is also positioned in the center of the magnets facing the opposite orientation. The magnetron sputtering setup used in this thesis is shown at Figure 39.
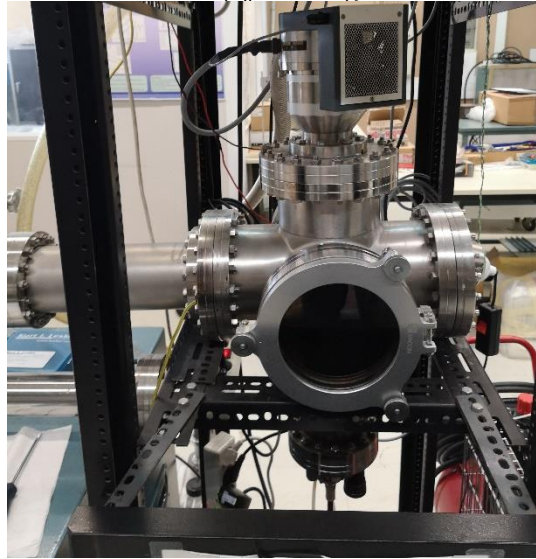
Figure 39: Magnetron sputtering experimental setup of University of Ioannina.

Depending on the experimental procedure the overheating of the target from excessive voltage is a possible major problem (70). Additively, the magnets are quite sensitive to heating and disfunctions from the excess temperature are possible. For the protection of the magnetron sputtering deposition machines appropriate cooling systems are applied. The sputtering system used in this thesis uses a deionized H_2O cooling system used in both DC/RF sources that is constantly working during the whole process. The experimental setup in this work contains a system for the cooling of magnets of the same logic working in a closed circuit.

The thin films grow by using a confocal dual cathode magnetron sputtering unit using two unbalanced magnetron sources at 45º with respect to the sample holder. This geometry is already known from other similar works (29) (30) (56). The chamber contains a spherical chamber from stainless steel. The sputtering chamber is supported by an ALCATEL Adixen Pfeifer rotary vacuum pump and a turbomolecular pump ALCATEL ACT 200T capable of reaching 27000 rpm and can attain high-vacuum conditions. As for the supported gases, they are inserted with an AALBORG SDPROC 4-channel command measure unit which precisely controls their flow. Whether the gases are inert or reactive they can safely be inserted onto the chamber. Therefore, both magnetron sputtering and reactive magnetron sputtering can be performed. As for the power supplies, there are two RF/DC sources perpendicular to each other. Each side has a material-target, the magnets, and the water-cooling system separately. The magnetron sources are placed at 45º with respect to the sample holder, a common geometry for Dual Cathode systems (29), (56). Cu shutters can be manually controlled so the deposition can be fully controlled for the cases of multi-layer films. High purity targets of metallic materials purchased from Kurt J. Lesker Company with diameter of 2 inches are used at the magnetron sources. The further processing of the materials is done by a two-step growth method of a) the previously explained magnetron sputtering deposition technique and b) post-growth plasma treatment (usually oxidation).

2.2.3 Oxygen Plasma Treatment

Depending on the wanted result, sometimes the thin films from the deposition are undergoing further treatment. The extra process performed in this thesis is the post-growth treatment and just as its name implies it happens after the deposition of the metallic thin film. This extra step can result into complete changes of the material's surface properties by enhancing some special characteristics. One of the most used post-growth methods is the oxidation of metallic thin films done separately from the deposition. There are many ways of oxidizing the film like thermal oxidation, hydrothermal methods or chemical reactions. The oxidation method proposed in this thesis is by annealing the thin films with oxygen plasma (the setup is depicted in Figure 40).

Oxygen plasma is the method where oxygen is introduced to a vacuum chamber for plasma treatment. Other reactive oxides like Nitrogen can also be used for even more exotic compounds like nitrides. The vacuum is created by a rotary pump applied to a borosilicate glass tube. The sample is placed in the middle of a coil and the oxygen plasma is created by the application of RF power source. Usually, a power >500W is necessary for a proper oxidation of harder metals creating plasma in H mode, while E mode plasma with small powers can also be formed (71). The treatment can either can be done step by step, or at once.

Figure 40: Oxygen plasma setup of post-growth thin film treatment.

Treating the grown film with plasma after the deposition offers many advantages compared to using O_2 in the chamber alongside other gases (29), (71). Especially, when other reactive gases like N_2 exist in the chamber other compounds like nitrides can be created. With the appropriate temperature conditions exotic phases and crystal structures can also be formed with utmost precision. Hence, new properties like optical transparency can be added to the films. Even compared to classic methods like gas oxidation, oxygen plasma treatment offers many advantages. Plasma chamber is relatively safer, since only the vacuum tube and the heatproof substrate holder are exposed to high temperatures, which are considerably lower than the classical methods.

Besides the basic plasma physics of the creation and the spreading of the plasma which were shown in previous chapter thermal physics is also important in the process. When a sample is heated because it is radiated by a considerable amount of heating it can be considered as a blackbody. The blackbody radiation is a type of radiation emitted by all matter upon heating. The intensity of that thermal radiation can be approximated by using the Stefan – Boltzmann law (72):

$$I(T) = \sigma \cdot T^4 \qquad (3.1)$$

Where σ, is the Stefan-Boltzmann constant. This law attempts to create a relationship between the radiation and the temperature of the blackbody. The temperature in the chamber which can be estimated by devices like thermistors, thermocouples or pyrometers can extract a first idea about the phases and crystal structures formation, and it is deeply depended on the annealing time. Therefore, the temperature has a major dependence from the treatment time either done step by step, or continuously.

2.2.4 X-rays Diffraction (XRD)

One of the most known types of high-energy radiation is the X-Rays and it was discovered by Wilhelm Conrad Röntgen in 1895 (that's why is also known as Röntgen radiation). Their name originates from their initially unknown nature as a type of radiation emanating from discharge tubes during certain experiments. Their wavelength is shorter than UV rays and they have a wavelength area from 10 nanometers to 10 picometers (Figure 41). They are used in a wide variety of applications like medical applications and materials science.
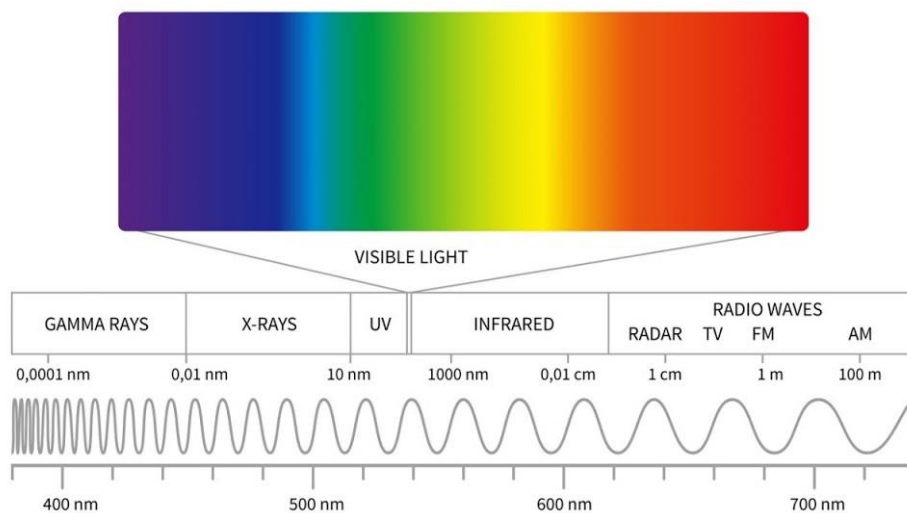

Figure 41 : The visible spectrum compared with the other Electromagnetic radiations.

The typical production of X-Rays is taken place with the deceleration of thermally produced electrons by a thermal filament. Those electrons are at first accelerated by a potential difference that gets values up to 40kV and therefore they are very fast moving. The decelerated electrons bombard targets of certain metallic materials like Cu, Al, Mo, Co, etc. The most widely used one is the Cu radiation, while other types

like Co are also being used. Different metallic filaments will result in the same diffraction peaks but different peak positions because of the different wavelengths.
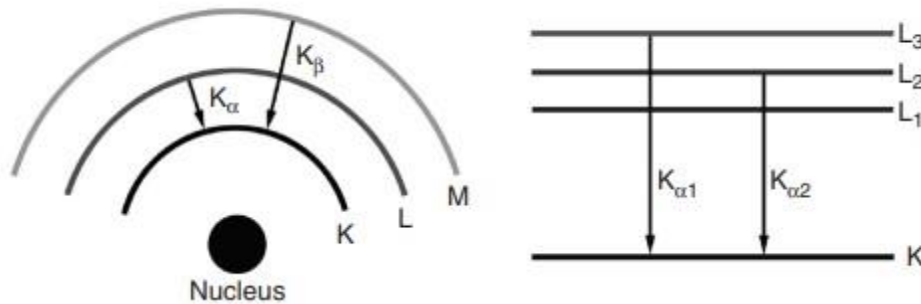

Figure 42 : Electron transitions in the atom that cause the X-Rays radiation.

From this process a continuous spectrum of photons (Bremsstrahlung radiation) occurs. At certain wavelength there are the electron transitions K_a, K_b, L_a, L_b, etc from the expelled electrons that were described in the previous process (Figure 42) (73). Those transitions will finally result in the characteristic diffraction lines. For each of the transitions we may observe more than one line. This is because of the orbital spin of the outer shells. For example, in K_a transition we see K_{a1} and K_{a2}. The K_{a2} usually gives no useful information and special filters are used to cut-off their signal. The most used is the metallic Ni filter with a K absorption edge ≈1.488 Å. An example of characteristic K lines for Molybdenum is shown at Figure 43 (73).
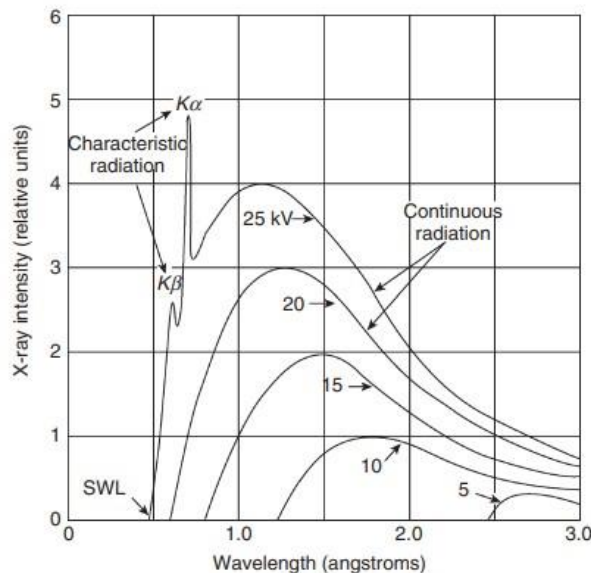
Figure 43 : The characteristic K lines for a Mo target material operating at 25kV.

One of the most fundamental material characterization techniques is the X-Rays Diffraction (XRD for short). XRD is one of the most widely used techniques for the phase/material recognition of a solid. Also, XRD is the most important technique for acquiring information about the crystal structure of a solid material. Crystal structure,

lattice constant, Miller indices of the materials are some of the information we can extract from the technique. The instrument used for applying the technique is called X-Ray Diffractometer, name which originates from the nature of the technique. At first, it was developed for studying the crystal structure of powder-like samples, but nowadays it is expanded in a wide variety of samples like bulk solids, surfaces, or even thin films.

The basic theory behind the technique is based in Bragg's law of diffraction, which obeys to every type of crystal structure. The formula of Bragg's law is given without proof by:

$$n \cdot \lambda = 2 \cdot d \cdot \sin(\theta) \tag{3.2}$$

Where λ is the wavelength, θ is the angle of incidence beam and the lattice plane and the d are the spacing between two parallel crystal lanes in the solid, which is also known as d spacing. A schematic for the process of Bragg diffraction is depicted in Figure 44 (74).
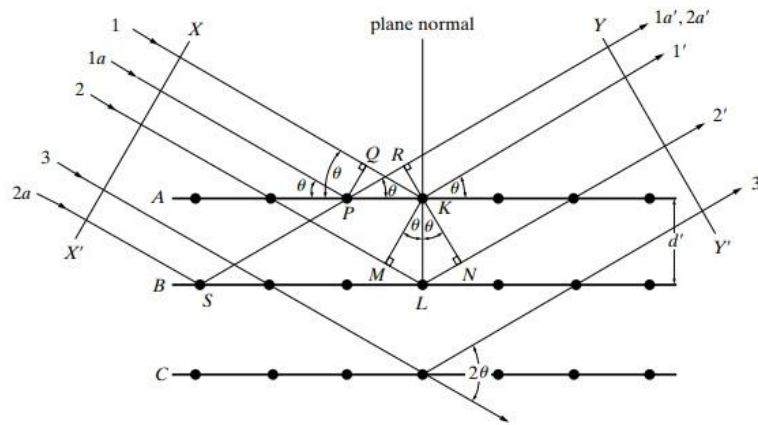
Figure 44 : Braggs law of diffraction.

The d-spacing (or the angle) is one parameter, which when it is combined with the knowledge of Miller indices (a set of three integers that represents a family of parallel planes in a crystalline solid), that we will gain from the experiment we can estimate the characteristic lattice constants of the materials. The formula varies, depending on the type of the crystal structure of the material. For example, the formula for the tetragonal system is given without proof in the following equation:

$$d = \frac{a}{\sqrt{h^2+k^2+l^2(\frac{a^2}{c^2})}} \tag{3.3}$$

A combination of the equations (1) and (2) will create the mathematical relation between the incident angle and the Miller indices:

$$sin^2\theta = (\frac{\lambda}{2})^2 \cdot (\frac{h^2+k^2}{a^2} + \frac{l^2}{c^2}) \tag{3.4}$$

As already mentioned above the device used is called X-Ray Diffractometer. The diffractometer uses an X-Rays source of a single wavelength for measuring mostly

polycrystalline materials. Despite there is a single wavelength within the source, the capability of changing the angle of the X-Rays gun (therefore the change of incident wave results in an angular change in incidence and diffraction covering a large area). The result of the measurement is a plot of the intensity of the X-Rays with the angle between the incident and the diffraction beam. The angles that result in peaks in the diffractogram, correspond to the identification peaks for the phase of the material and a triplet of numbers hkl characterizes the peak. Besides the angle, sometimes the d-spacing is also plotted.
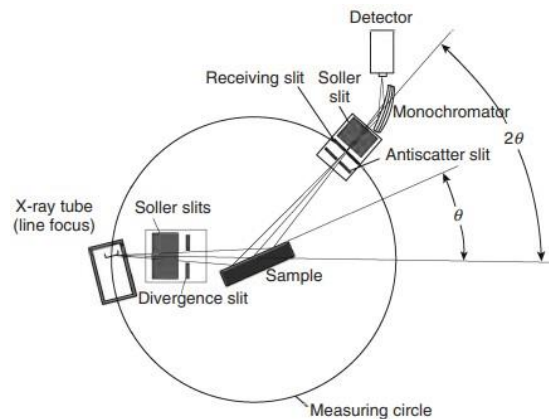
Figure 45 : X-Ray diffractometer basic geometry of Bragg-Brentano geometry.

The most widely used geometry of an XRD setup is known as Bragg-Bertrano geometry and it is the most known geometry for the technique, Figure 45. In this geometry the X-Rays source remains fixed during the measurement, since we have the movement of the sample holder in the range of θ. We also have movement of the detector for an angular range of 2θ. Therefore, we have a θ-2θ geometry of the system. This geometry is commonly used in measuring powder samples.
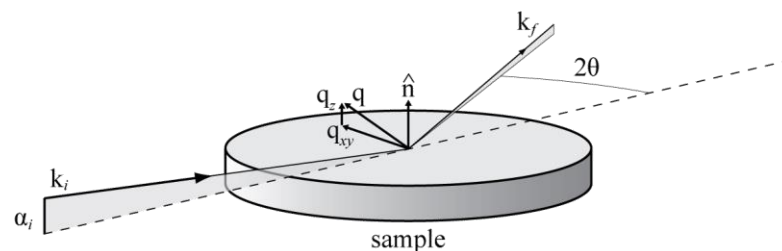

Figure 46 : Grazing Incidence geometry for thin films measure.

However, for the measurement of surface-like samples like thin films the previously mentioned geometry is not the most appropriate for the analysis. In *Figure 45* the geometry θ-2θ is shown, and in Figure 46, geometry most suitable for surface sciences (73). The Grazing Incidence XRD (GID for short), which is suitable for materials produced by coating uses a special optical arrangement for detecting the crystal structure of films. The X-Rays source is positioned so that the incident beam is directed at the sample at a very small angle (<1º) as it is shown and at Figure 47. With that setup only the detector moves in order to obtain the signals of diffraction.

ΜΕΤΑΠΤΥΧΙΑΚΗ ΔΙΠΛΩΜΑΤΙΚΗ ΕΡΓΑΣΙΑ ΟΝΟΜΑΤΕΠΩΝΥΜΟ: ΙΩΑΝΝΗΣ ΠΑΓΩΝΗΣ
ΤΙΤΛΟΣ: Growth and characterization of Type I (Straddling gap) and Type II (staggered gap) heterojunctions alignment in thin films for potential photovoltaic applications
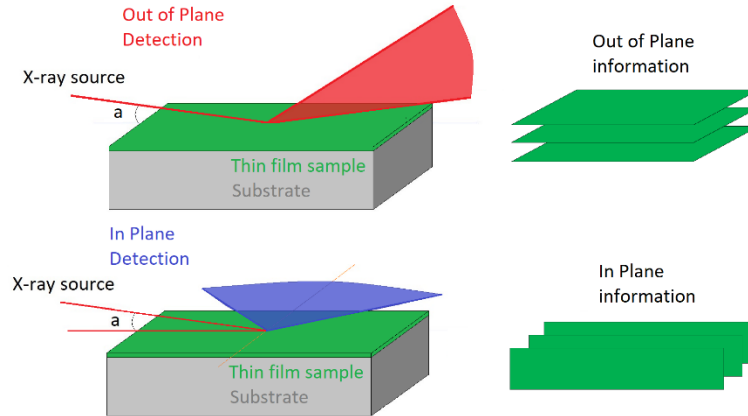*ΠΜΣ-Φυσικής*   *Τμήμα Φυσικής*   *Πανεπιστήμιο Ιωαννίνων*

Figure 47 : Grazing incidence for out/in plane measurements.

The GID geometry has the great advantage that there is no need of extra sample preparation for the measurement like grinding, since there is no need to create the totally flat surface of powder-like samples. The preparation for the thin films was already done by the deposition part of the experiment. This also means that because the deposition of the film may include "islands", the crystal planes of the material won't be so well defined. Therefore, the pattern of XRD is not as sharp as the one of the Bragg-Brentano geometry.

In an ideal XRD graph a diffraction peak should be a perpendicular line similar to a delta function without any width, something that never occurs in a typical measurement because of many factors that must be taken in account. An example of a real peak compared to an ideal peak is shown Figure 48 (73). The first one is because of the instrument itself, which may include different factors that occur in the experiment. One of the factors is the intensity of the X-Rays. Most commercial XRD systems for cost efficiency have limits to their power supply. The second and most interesting reason is that the peak width can help in X-Rays the calculation of the crystallite size of the material. The Full Width at Half Maximum (FWHM) is mathematically defined as the difference between the two values of the independent variable at which the dependent variable is equal to half of its maximum value.
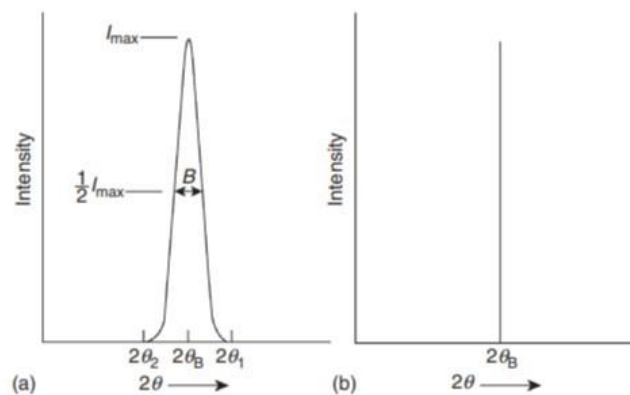

Figure 48 : a) FWHM for a diffraction peak b) Ideal diffraction line.

A third reason that determines the height and width of a diffraction peak is the residual stress applied to a material, that results in a strained material as shown in Figure 49. Depending on the way the stress applies, we can either have a uniform strain that results in an angular shift or a nonuniform strain and extra width of the peak. The relationship that describes the change of crystallite size with the stress can be obtained by creating the Williamson-Hall plot for our peak. Without proof, the Williamson-Hall (75) relationship that occurs is given by the following relationship:

$$B \cdot \cos(\theta) = \frac{\lambda}{t} + 2 \cdot \eta \cdot \sin(\theta) \quad (3.5)$$

Whereas t is the grain size of the material and η is the non-uniform strain factor. An example of a result of the W-H plot is depicted in Figure 50 (76). The Williamson-Hall relationship can be simplified even

Figure 49: The effect of stress and strain in the peak position and peak width.

further by supposing that the stress factor is equal to zero. This approximation will lead us to the most known method for calculating a materials' crystallite size, the Scherrer equation:

$$t = \frac{k\lambda}{B_{1/2}\cos(\theta_B)} \quad (3.6)$$

The Scherrer equation is the most known way of calculating a crystallite's grain size with the only drawback to be the fact that it works for particles diameters smaller than 150nm. In (3.6), k is known as the Scherrer constant and in the most cases it is given the value 0.9, $B_{1/2}$ is the previously mentioned FWHM in radians and θ_B is the center of the diffraction peak we study.
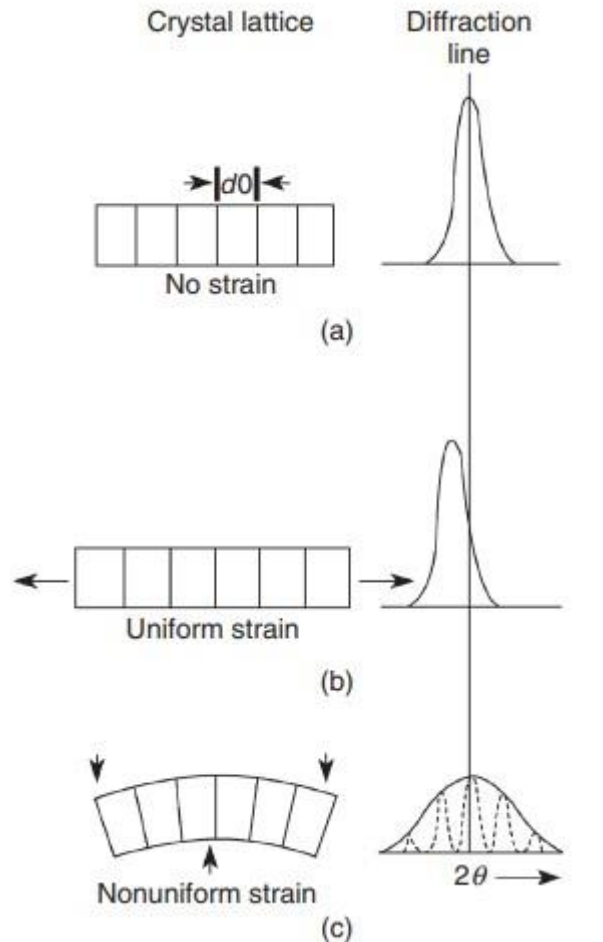
ΜΕΤΑΠΤΥΧΙΑΚΗ ΔΙΠΛΩΜΑΤΙΚΗ ΕΡΓΑΣΙΑ ΟΝΟΜΑΤΕΠΩΝΥΜΟ: ΙΩΑΝΝΗΣ ΠΑΓΩΝΗΣ
ΤΙΤΛΟΣ: Growth and characterization of Type I (Straddling gap) and Type II (staggered gap) heterojunctions alignment in thin films for potential photovoltaic applications
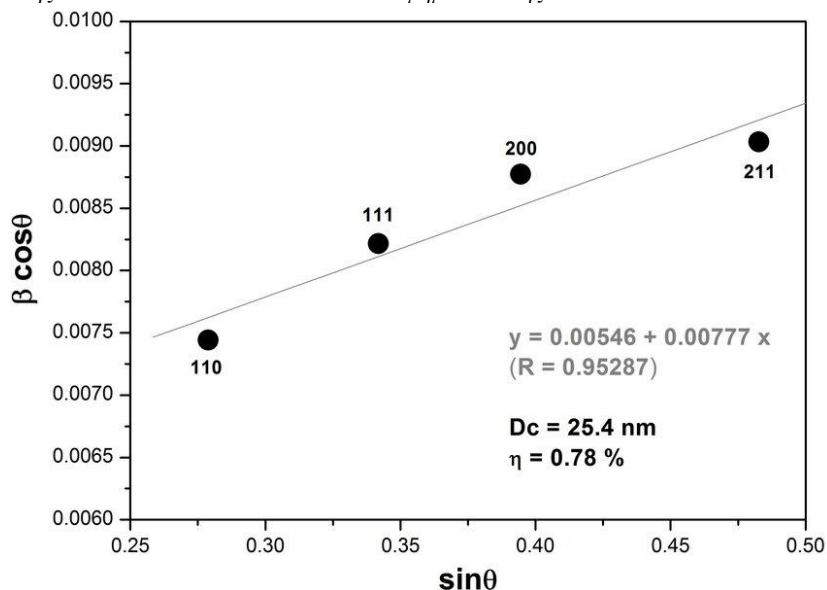*ΠΜΣ-Φυσικής*   *Τμήμα Φυσικής*   *Πανεπιστήμιο Ιωαννίνων*

Figure 50 : Williamson-Hall plot for SrTiO3 perovskite material.

The technique so far only referred to crystalline materials, most of the studied materials with X-Rays diffraction. However, the technique can partially analyze amorphous solids, with amorphous referring to the materials that lack a crystalline periodicity. One very known case is the diffraction pattern of the room temperature SiO_2 which is a ceramic glass and therefore amorphous. Also, for the case of deposited materials the XRD pattern can determine the formation of metallic glasses on the thin film. As metallic glass is defined the combination of two or more metals that acquire an amorphous structure (i.e. lack of periodicity) after the deposition. Partly crystalline materials usually have great disarrays bust in some cases (mostly at low temperatures) they become more organized at some spots in the molecule and form crystallites. Those physically formed crystallites can now be observed and give diffraction peaks that tend to be very broad.

Concluding what was shown before an X-Rays Diffractogram can be the "identity" of a studied material. By known the diffraction peaks information about the materials and their crystal structure can be learned. By using the diffraction peaks and the corresponding miller indices additional information about the crystal structure can also be calculated.

The most important part of the analysis is the confirmation of the materials in the sample and their crystal structure. Different structures are characterized by different peaks since their d spacing gradually changes as well. The most known way of identification of a diffractogram is by a qualitative comparison with another similar one from the bibliography. The things that are compared are the structure of the crystals, the peak positions, and the Miller indices. This method is not the most appropriate one because it is mostly suitable for checking the structure of known materials. For an unknown material or a multi-phases, the diffractogram can become rater complicated. Another qualitative method of matching XRD data is by using the diffraction data of a crystallography database. The most known base of data for this technique is the International Center for Diffraction Data (ICDD) which contains

ΜΕΤΑΠΤΥΧΙΑΚΗ ΔΙΠΛΩΜΑΤΙΚΗ ΕΡΓΑΣΙΑ ΟΝΟΜΑΤΕΠΩΝΥΜΟ: ΙΩΑΝΝΗΣ ΠΑΓΩΝΗΣ
ΤΙΤΛΟΣ: Growth and characterization of Type I (Straddling gap) and Type II (staggered gap) heterojunctions alignment in thin films for potential photovoltaic applications
ΠΜΣ-Φυσικής   *Τμήμα Φυσικής*   *Πανεπιστήμιο Ιωαννίνων*

almost all the important information of a phase of a material (peaks, Miller indices, crystal structure, Wyscoff vectors etc). They are stored into Powder Diffraction Files (PDF) and they can either be bought separately, either they are provided with a specific software suitable for the analysis of experimental data like Bruker EVA, or X'Pert Highscore Plus. A free alternative but with a smaller database is the Crystallography Open Database (COD).

Qualitative analysis offers a good first view of the characteristics of the material, but for the case of an unknown structure of a material it is not completely trustworthy since one peak may belong to another dissimilar material that doesn't belong to the material. However, to gain the complete information of the characteristics for an unknown material the qualitative analysis is of utmost importance. The most known method of quantitative analysis is the Rietveld refinement which can reproduce the whole XRD pattern with theoretical models and it can be done with special programs like (FullProf or GSAS). It uses the least squares method for reproducing the refinement matches the whole profile.

The theoretical background for quantitative method is the calculation for a structure the theoretical peak positions (angles) by using the types of d-spacing just like the tetragonal structure one that was mentioned before. The combination of Bragg's law and the d-spacing can give the exact theoretical peak positions for every triplet of hkl in existence and the correspondence with the experiment can easily be done by comparing theoretical and experimental angles. For the creation of a complete model of theoretical calculation of the expected peaks, the calculation of the theoretical X-Rays intensities (or the normalized intensities) is also important. The general formula that describes the expected intensities of the diffracted X-Ray radiation is the following.

$$I = |F|^2 \cdot p \cdot \left(\frac{1+cos^2 2\theta}{2sin^2\theta cos\theta} \right) \cdot \frac{1}{2\mu} \left(1 - e^{-\frac{2\mu t}{sin\theta}} \right) \cdot e^{-2M_T} \tag{3.7}$$

In the above relation we have the product of several dependence factors that will be thoroughly explained. The first term is the squared $|F|^2$ which is defined as the squared structure factor of a peak. The structure factor F_{hkl} by which occurs is the mathematical expression of the scattering of matter with radiation.

$$F_{hkl} = \sum_{j=1}^{M} N_j f_j e^{2\pi i (hu_j + kv_j + lw_j)} \tag{3.8}$$

Where M is the total number of atoms in the unit cell, f_j is the atomic scattering factor, N_j is the occupation factor, which is mostly considered equal to 1 for simplicity and u_j, v_j and w_j are the positions of the atoms in the unit cell. The three numbers represent each dimension of the crystal, and they are commonly expressed in 1/2 form.

Another important quantity for calculating the intensities of the theoretical peaks in powder samples is the second term of the product, also known as multiplicity, p. This term is a single number, and it is very important for multi-crystalline samples of powder because all the Miller levels with the same d-spacing will be consisted of a

single peak at a certain 2θ angle. The discrimination of those levels for the same family of Miller indices can be only done by using single-crystal diffraction patterns.

The third important term which consists of an angular part is known as the Lorentz polarization factor (it occurs from the combination of Lorentz and the polarization factors). The polarization factor can be calculated from the angular distribution of the scattered radiation for a non-polarized X-Rays beam, whereas the Lorentz factor describes the changes in the intensity of the diffraction in a 2θ angular range. The combination of those two factors will result in the following angular distribution formula:

$$Lorentz - Polarization\ factor = \left(\frac{1 + cos^2 2\theta}{2 sin^2 \theta cos \theta} \right) \tag{3.9}$$

Those three factors are very important parameters for determining the intensities of the radiation of a pattern. Besides them there are other, secondary factors that can be also taken account for the best possible result. The absorption factor is one of them and it has dependence on the thickness of the materials for study. The linear absorption coefficient, μ is responsible for the existence of this factor. Lastly, there is the temperature factor which describes the thermal fringes because of the broadening of the crystallites. Furthermore, the temperature factor can directly affect the value of the atomic scattering factor, f in the following dependence:

$$f = f_0 e^{-M_T} \tag{3.10}$$

2.2.5 X-ray Photoelectron Spectroscopy (XPS)

The X-Ray Photoelectron Spectroscopy (XPS) is one the most known technique from the family of the electron spectroscopy techniques. Electron spectroscopies are spectroscopic techniques for elemental analysis, which use excited electrons of a material for revealing their nature.

The XPS is a surface-sensitive technique based in the photoelectric effect, Figure 51, with a maximum penetration depth of 10nm, in which an X-Ray source (gun) fires X-Rays photons in a surface or a thin film. In the photoelectric effect, a phenomenon occurring naturally in space, an incident ray of light directly hits a metal surface, and it results in the ejection of excited electrons called photoelectrons.
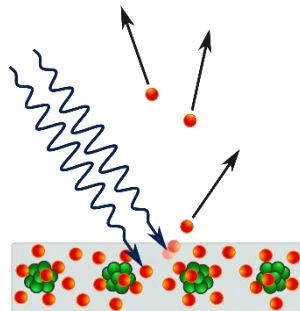

Figure 51 : A schematic representation of the photoelectric effect.

The kinetic energy of the electrons is given by the Einstein equation for the photoelectric effect:

$$K.E. = hv - B.E. - \varphi \qquad (3.11)$$

In this relationship φ is the work function of the metal (the minimum energy in order to remove an electron from the surface to the "infinity"). In the XPS the work function is mostly acting as correction factor, and it is absorbed to the instrument. Even though there have been some attempts for the absolute calculation of work function from spectroscopies (77). The term "hv" is referred the X-Rays energy of the anode of the source gun. In the XPS the anode is usually Magnesium (Mg) or Aluminum (Al). Depending on the anode used, the photoelectron peaks positions will differ, since the binding energy of the peaks will change drastically. The last term refers to the Binding Energy of the material (B.E.), which is the necessary energy that is needed from separating a particle from a system like the metal we previously mentioned.
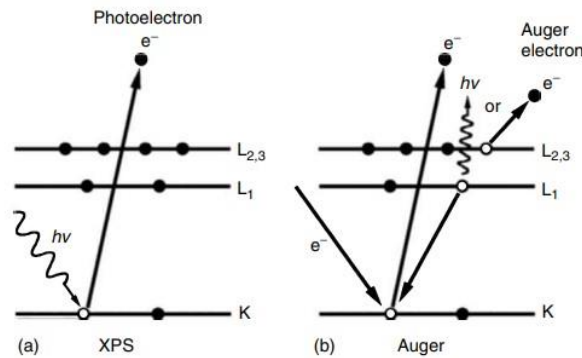
Figure 52 : The Auger effect, the secondary phenomenon that occurs after the photoelectric effect.

Besides the photoelectrons we also can study a secondary effect that occurs naturally after the photoelectron excitation, and it is known as the Auger effect and it the Auger electron which occurs balances the states after the photoelectron excitation. The process is clearly represented in the upper picture, Figure 52 (73).

After a photon/electron beam hits in the K shell, we have the ejection pf the photoelectron outside of the material creating a vacancy in the K-shell. For maintaining balance, an electron from L_1-shell drops to the K-shell since the system becomes more stable with the combination of excited radiation from the L_1-shell electron. Since now there is another vacancy in L_1-shell now, the system becomes totally stable with the excitation of another electron from the $L_{2,3}$-shell which has lower energy. The ejected electron is named Auger electron and the process Auger effect.

The Auger peaks instead of the photoelectron (spin-orbital e.g $2p_{1/2}$) they are recognized by three letters that symbolize the shells that take effect (e.g. KLL). The kinetic energy of the Auger electron is given by:

$$KE_{KL_1L_{2,3}} = BE_K - BE_{L_1} - BE_{L_{2,3}} \qquad (3.12)$$

60

Most modern XPS devices can create a spectrum that include both XPS and (Auger Electron Spectroscopy) AES peaks, in a single X-Ray chamber. The electron spectrometer as the device capable of producing the X-Rays, housing the sample, and analyzing the spectrum is called is represented schematically in Figure 53.
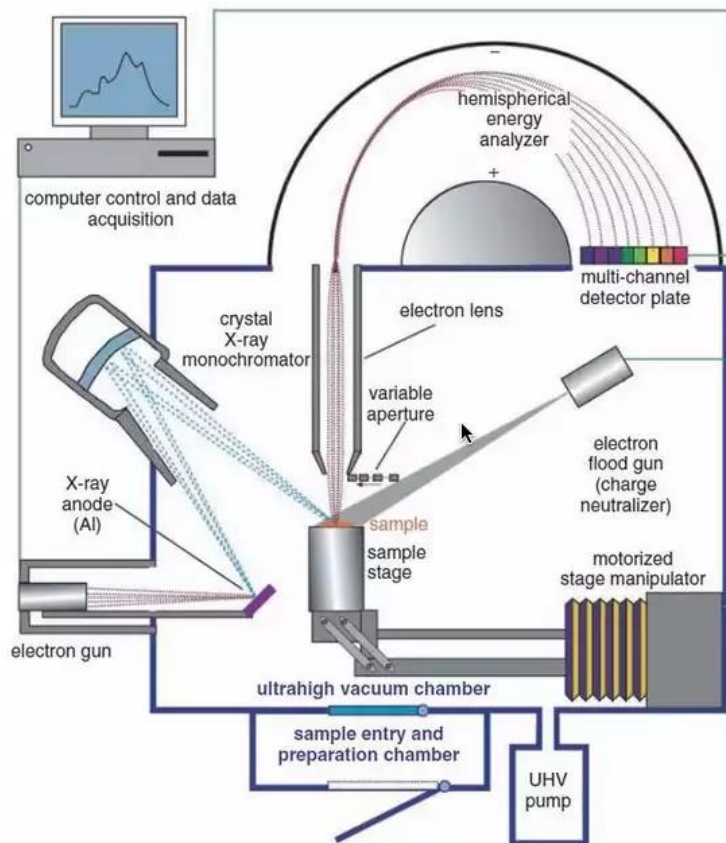

Figure 53 : The electronic spectrometer for XPS analysis.

Although the source has a single energy depending on the anode, by the analyzer we can record the entire spectrum of energies from core to valance electrons and even the Auger peaks. The spectrum consists of the X-Rays intensity and the kinetic energy (or binding energy). For XPS spectra we are interested in the binding energy and for AES the kinetic one.

In the XPS spectroscopy we have a material, unknown or known and we want to confirm its components, or check the existence of any impurities in the sample. There are two types of scanning: the basic/survey scan and the detailed/high-resolution scan. The survey scan is a fundamental first step in case the type of the material is unknown. In this method the analyzer creates a broad scan of the entire spectrum to confirm the elements that there are present in the material from the excited photoelectrons and Auger electrons. The spectrum covers a wide variety of energies and depending on the anode we have a survey scan in energy areas ≈1253.6-0eV for Mg anode and ≈1486.6-0 eV for Al anode. The high-resolution scan is used for material phase (e.g. metal or metallic oxide from the electron states energies), for chemical identification (e.g. chemical bonds). The first with the deconvolution of the

detailed peak mostly with mathematical fitting we can exactly know all the phases of the material under study.

Eventually, we may need to identify the elements and their phases, that we got from the measurement. The most known way is a qualitative analysis of the spectrum compared to theoretical ones from the bibliography or databases and matching them with our peaks. In XPS high resolution scan the spectra we obtain may be a result of one or more curves that can be deconvoluted into parts with Gaussian fitting process, as we mentioned before. Something that is important for the analysis is a phenomenon called chemical shift, which results to different energy positions of the peaks. This occurs mostly because of the sensitivity of hydrocarbon elements, and it can easily be fixed comparing a carbon peak (e.g. C 1s) experimental value with its theoretically expected value. The result is subtracted from the binding energy values of the spectrum.
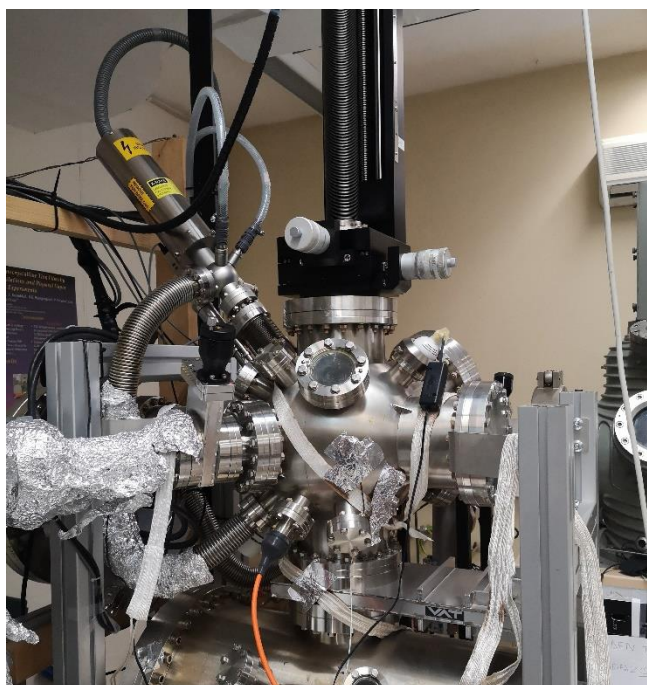
Figure 54: The SPECS GmbH XPS setup of University of Ioannina.

The XPS instrumentation we used, is the SPECS GmbH system equipped with the Phoibos HSA-Phoibos 100 analyser. The X-Rays chamber is capable of ultra-high vacuum conditions supported by ion pump and the X-Rays can be produced from anodes of two different metals: Mg and Al. The spectrometer is depicted in Figure 54. An example of survey for an Aluminum oxide is shown in Figure 55 (78). In the survey scan a first idea of the present elements can be extracted. To be more precise three elements are present, Al, O and C which implies that the sample is devoid of impurities.
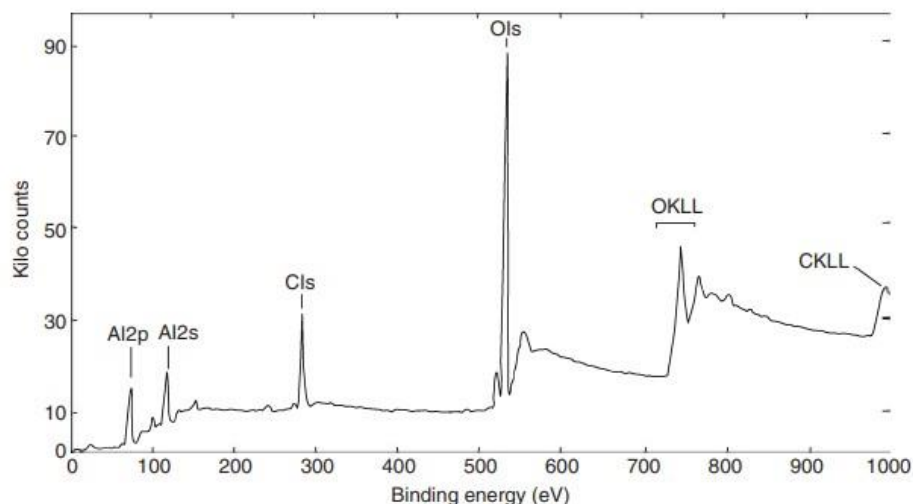
Figure 55 : An example of a survey scan of a multi-atom surface.

In the high-resolution scan we can extract most of the information about the sample. From the deconvolution of the Gaussian curves of the spectra, as we mentioned before we can make a phase identification of the material. The deconvolution of the photoelectron peak can be done with Gaussian fitting with an appropriate code or with special analysis software like CasaXPS. For example, a high-resolution spectrum for poly(vinyl trifluoroacetate) is shown in Figure 56 (79). For double peaks in high resolution scan the spin orbit splitting of electron takes effect.
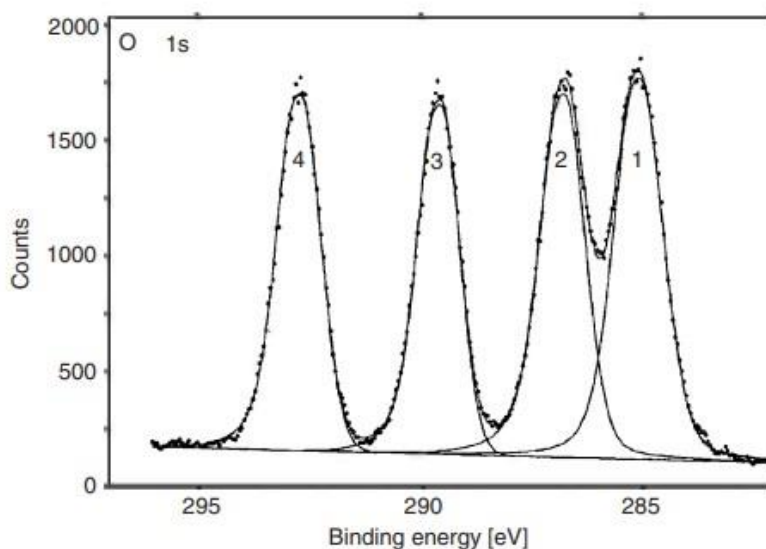
Figure 56 : A high resolution scan of an oxidized silicon wafer of 2p orbital.

In most high resolution scans the Oxygen and Carbon peaks must be scanned because except the energy shift, XPS is able to identify the chemical bonds that occur with these elements (e.g. Carbon single or double bond). As it was mentioned, the double photoelectron peaks in high-resolution scan are due to spin-orbit coupling of the p, d and f orbitals in the electronic configuration of the structure. Additionally, extra peaks

in a variety of materials are also likely to be observed. The secondary peaks are generally categorized in three major groups.

The first category is the "shake-up" satellites, which is probably the most usual type of extra peaks, and they tend to appear in materials like CuO (73). Their occurrence emanates from the interaction between photoelectrons and electrons from the valence band. They tend to attain higher binding energy compared to their respective photoelectrons, because the latter can excite the valence electron in an energy level which is higher than its normal one. Therefore, it results in the creation of a "shake-up" peak. For the CuO which was previously mentioned is one useful characteristic for distinguishing between the Cu_2O (56) (73). The Cu_2O oxide does not possess those extra satellite peaks or possesses one very weak extra satellite peak (80).

Another common type of extra peaks in the spectrum is called multiplet splitting in core-level peaks (73). The phenomenon of multiplet splitting usually occurs in an element or a compound with unpaired valence electrons. It is mostly studied in the 2p orbitals of transition metals like Ni, Cr, Mn but they are not the only cases. Despite its existence makes the spectrum more difficult to understand, if the material phase for study is known it can be used for phase recognition with qualitative comparison with another phase of the material that lacks the extra peaks. One common comparison is NiO, in which multiplet splitting occurs with $Ni(OH)_2$. The understanding of this property of the spectrum is based in the quantum theory of the electronic structure.

The last widely known type of extra peaks is the peaks created from plasmonic loses (73). The satellite peaks from plasmon loss are not useful for the analysis of the spectrum since they only complicate it without giving any information about the specimen. The plasmonic losses are expressed from the loss of kinetic energy because of the excitation of collective vibrations from conductive electrons (plasmons) in metallic materials like Ag.

Now let's return to the analysis of the deconvoluted peaks of the high-resolution scan. As it was stated before each fitted curve can be matched to a chemical bonding that occurs to the studied specimen. The C 1s and O 1s peaks exist almost in all photoelectron scans, since they are important atmospheric components, and some residues may still exist in the vacuum chamber. Besides them for the study of a material like Sn the deconvolution of the peaks will also reveal if there are any oxides (or some other type of combination like nitrides). Each Gaussian fitted curve has a designated area, which can be calculated by using a finite integral of the Gaussian or normal distribution curve:

$$Area = \int_1^2 A \frac{e^{-\frac{1}{2}\left(\frac{x-\mu}{\sigma}\right)^2}}{\sigma\sqrt{2\pi}} \tag{3.13}$$

The "1" and "2" limits in the integral refer to the lower and upper limits of the binding energies of the Gaussian respectively, A is a normalization factor that can be considered as the X-Rays intensity of the y-axis, μ is the mean value that can be explained as the center of the Gaussian and σ the standard derivation at the FWHM of the curve. This formula works for all types of Gaussians fitted curves, including the photoelectron peak itself. That means that by dividing the deconvoluted peak with the

area of the total area of the peak, it is possible the calculation of the %composition of the phase in the surface without using any extra technique. The %composition is given in the following process:

$$\%Phase\ Composition = \frac{Area\ of\ deconvoluted\ curve}{Area\ of\ photoelectron\ curve} \qquad (3.14)$$

This is a versatile method that works regardless the intensities measuring unit because of the remnant between two similar quantities and it is useful even if the raw data are not normalized since it also works like a type of normalization of the peak. For compositions between many photoelectron peaks the last statement is true only if the high-resolution scan for these peaks was performed with the same parameters.

ΜΕΤΑΠΤΥΧΙΑΚΗ ΔΙΠΛΩΜΑΤΙΚΗ ΕΡΓΑΣΙΑ ΟΝΟΜΑΤΕΠΩΝΥΜΟ: ΙΩΑΝΝΗΣ ΠΑΓΩΝΗΣ
ΤΙΤΛΟΣ: Growth and characterization of Type I (Straddling gap) and Type II (staggered gap) heterojunctions alignment in thin films for potential photovoltaic applications
ΠΜΣ-Φυσικής   *Τμήμα Φυσικής*   *Πανεπιστήμιο Ιωαννίνων*

65

Chapter 3 : Experimental Results

ΜΕΤΑΠΤΥΧΙΑΚΗ ΔΙΠΛΩΜΑΤΙΚΗ ΕΡΓΑΣΙΑ ΟΝΟΜΑΤΕΠΩΝΥΜΟ: ΙΩΑΝΝΗΣ ΠΑΓΩΝΗΣ
ΤΙΤΛΟΣ: Growth and characterization of Type I (Straddling gap) and Type II (staggered gap) heterojunctions alignment in thin films for potential photovoltaic applications
ΠΜΣ-Φυσικής   Τμήμα Φυσικής   Πανεπιστήμιο Ιωαννίνων

66

3.1 Experimental Results for Sn Oxides Thin Films

3.1.1 Growth of the Sn thin films samples

In this chapter the experimental details and results from the deposition of the Sn thin films samples will be discussed. The deposition of metallic Sn thin films as a buffer layer were created in the rutile tetragonal structure. The geometry and the capability of the sputtering chamber were already mentioned in previous chapter. All the Sn films follow a certain sputtering process for easier comparison that is characterized by the deposition with RF power with a frequency of 13.5MHz, and a total deposition time of 25 minutes with periodic breaks in order to avoid possible melting of the target.

For the deposition of the Sn films as substrate there were used single-crystalline Si (001) foils. The foils were fitted to the sample holder with the use of a diamond cutter avoiding damaging the substrate. For the complete preparation of the surface, the Si substrates were cleaned with acetone and methanol. Clean substrate is important for a smoother deposition of the material in the vacuum chamber and the removal of extra organic substances. The sample holder can hold up to three substrates and is diagonally placed in the chamber so both target's ions can be attached onto the surface. For a smooth deposition it can spin in varying speeds. In the chamber high-vacuum conditions, which achieved with the combination of mechanical and turbomolecular pump, are characterized by basic pressure that varies from about 10^{-5} to 10^{-6} mbar depending on the duration of pumping. For every sample the chamber was filled with Argon gas with a flow of approximately 50sccm. The pressure of the working conditions due to the insert of the gas was reduced by three measurement units.

Presputtering in Ar conditions was performed for 5min with the same conditions as the sputter deposition. For avoiding the melting of the low melting point metallic Sn, the deposition was done in separate steps and with a relatively low working power. The conditions of the depositions are shown below (Table 2), with MS in the samples to stand for Magnetron Sputtering.

Sample	p_{basic}(mbar)	$p_{working}$(mbar)	P_{RF} (W)	Deposition Process
MS731	2.5×10^{-5}	3.6×10^{-2}	5	5min deposition, 5 min wait
MS732	1.2×10^{-5}	3.6×10^{-2}	5	5min deposition, 5 min wait
MS733	1.2×10^{-5}	3.6×10^{-2}	5	5min deposition, 5 min wait

Table 2: Sputter deposition conditions of the samples. MS stands for Magnetron Sputtering.

3.1.2 Oxygen plasma oxidation of the Sn thin films

In the last chapter the deposition conditions for the film creation were thoroughly explained. After the sputtering process, which was the first growth step, every sample for the creation of the potential heterojunctions between the tin oxides, the thin films

were processed further in the oxygen plasma treatment chamber, which is the second step of the growth process. The upper surface of the films was oxidized for all the samples in a fixed amount of time but with a different annealing step each time. Meanwhile the Sn metallic layer will now act as a buffer layer. The difference in annealing step was necessary for two basic reasons. The low melting point of metallic tin is the most basic reason and the second is the observation of surface differences in the nucleation of each crystalline phase of the tin oxides by implicitly controlling the chamber temperature.

In the oxygen plasma enter the placing of the sample below the coil, vacuum conditions are applied by a rotary mechanical pump for achieving pressure conditions about 8-9 x 10^{-2} mbar. The plasma is produced by ionizing O_2 gas which is inserted onto the treatment chamber. The plasma is formed in H mode (inductive mode) by the usage of RF power supply (13.5MHz). The H mode of plasma is formed by applying high RF power and it is characterized by high electron density (81). The high electron density results into the formation of atomic oxygen, which is reactive and boosts the oxidation process. The details for the oxidation of the Sn samples are shown in the following Table 3.

Sample	p_{basic}(mbar)	$p_{working}$(mbar)	P_RF(W)	Time (sec)	Treatment Process
MS731_OP69	9.5 x 10^{-2}	2 x 10^{-1}	550	70	Annealing 5sec, wait 1,30 min
MS731_OP70	9.5 x 10^{-2}	2 x 10^{-1}	550	70	Annealing 3sec, wait 1,30 min
MS731_OP71	9 x 10^{-2}	2 x 10^{-1}	550	70	Annealing 7sec, wait 1,30 min
MS732_OP72	9.5 x 10^{-2}	2 x 10^{-1}	550	70	Annealing 9sec, wait 1,30 min
MS732_OP73	9.5 x 10^{-2}	2 x 10^{-1}	550	70	Annealing 11sec, wait 1,30 min
MS733_OP74	9.5 x 10^{-2}	2 x 10^{-1}	550	70	Annealing 8sec, wait 1,30 min
MS733_OP75	9.5 x 10^{-2}	2 x 10^{-1}	550	70	Annealing 13sec, wait 1,30 min

Table 3: Summarization for all the treated samples with oxygen plasma.

3.1.3 Structural Characterization of Sn oxides thin films

For the study of the identification of the phases and the crystalline structure of the Sn oxidized thin films measurements of X-Ray Diffractions were taken place. The films were measured in a Bruker D8 Advance diffractometer with the Bragg-Bertrano geometry consisting of a Cu X-Rays tube (λ=1.5406Å). A wide angular range was scanned for each sample. Since, all the samples have almost all the same sputtering conditions it was expected that the results will be quite similar. Some of the peaks may differ from sample to sample indicating the effect of the annealing time. As for the Sn oxides, with the peak identification from the bibliography, it occurs that the oxidized thin films have multiple phases and exotic crystal structures.

As for the main Sn oxides, with the accurate peak identification from the bibliography, it occurs that the oxidized thin films have multiple phases of different tin oxides: SnO_2 in the rutile tetragonal crystal structure, SnO in rutile tetragonal crystalline structure. The peaks corresponding to the SnO_2 are matching with the (101), (111), (211), (220), (002) directions- (82) (83) (84). As for the SnO we have matching of the (001), (101), (110), (002), (200), (102), (211) directions- (85) (86). Some peaks metallic Sn from the buffer layer can be seen as well in the same tetragonal structure at the (301) direction- (87) (88). Additively a peak corresponding to the Si (002) was recorded at 33º. The Si (002) peak is because of the detection of Si from the substrate, and it is considered as a forbidden reflection (89). It can be attributed to Si lattice disorientations because of its incompatibility with the buffer layer (90).

Furthermore, the metastable phase of the intermediate oxide of Sn_3O_4 in triclinic (anorthic) crystal structure was also found. For the metastable, sub-oxide of Sn_3O_4 the main peak (003) was measured as it can be seen from the intensities of the diffractograms according to the crystal structure Lawson proposed (43). Additively, we also find the ($\bar{1}$12) and (112) diffraction peaks for the Sn_3O_4.

It can be observed from the diffractograms for all the samples the existence of the metastable phase is due to the post-growth plasma treating. The oxygen plasma treating of the metallic Sn thin films tends to create some uncommon cases of the Sn oxides not often found on the bibliography. Furthermore, the most logical reason behind the theoretical explanation of those changes is probably due to the high temperatures inside the oxidation chamber.

For the complete study of the characteristic values of the materials an approximate study of the crystallite's grain size was also done. Both the Scherrer's equation and the Williamson-Hall method were applied to the samples for a first evaluation of the grain size. The grain size for was estimated to be about 21nm to 89nm with the use of Scherrer's method to calculate bigger grain sizes compared to the fitting from the Williamson-Hall plot. The results from the W-H plots differ slightly with an average grain size for the samples around 36nm to 110nm. The difference in the values of the two methods indicates the effect of microstrains in the lattices of the samples according to equation (3.5).

The results of the XRD patterns of the samples with the 5sec, 7sec annealing step and their respective Williamson-Hall fits, are shown in the following figures. We can conclude not only the existence of the multiple phases with the directions we mentioned above but the additional decrease of the metastable oxide of Sn_3O_4 with the increase of the annealing step.

MS731_OP069 (5sec)
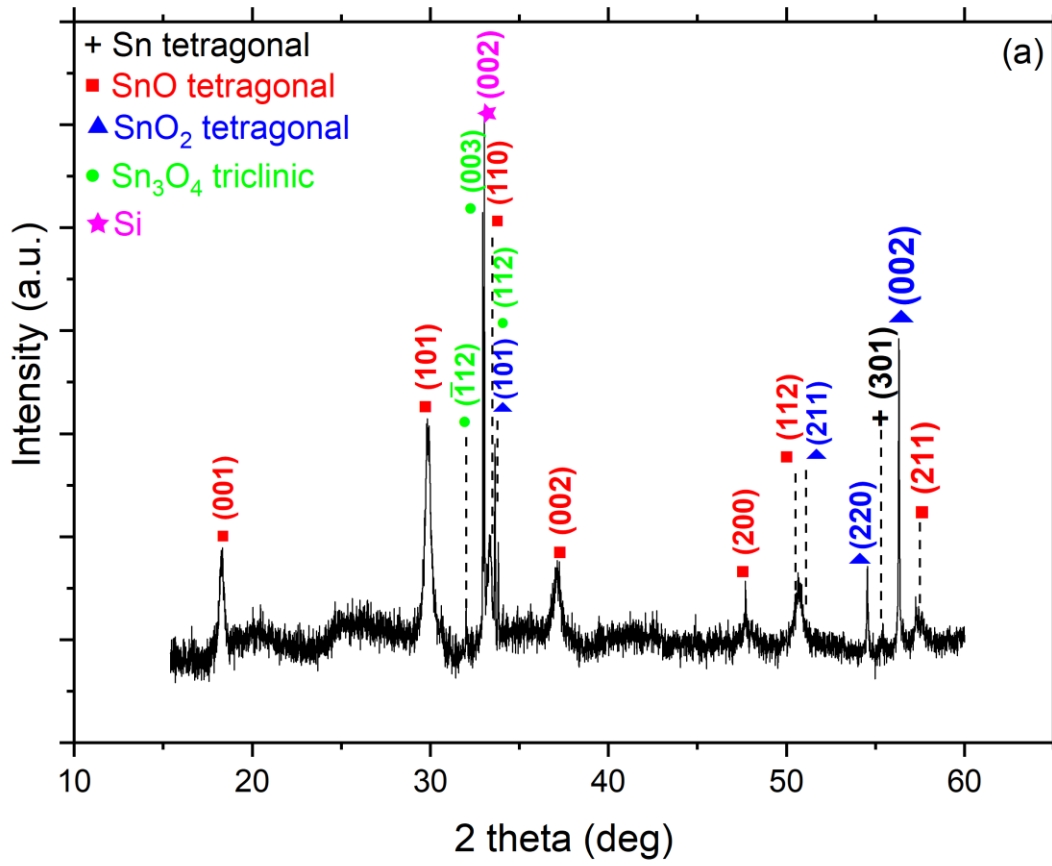
Figure 57: The XRD pattern for the Sn oxides thin film with 5sec annealing step.
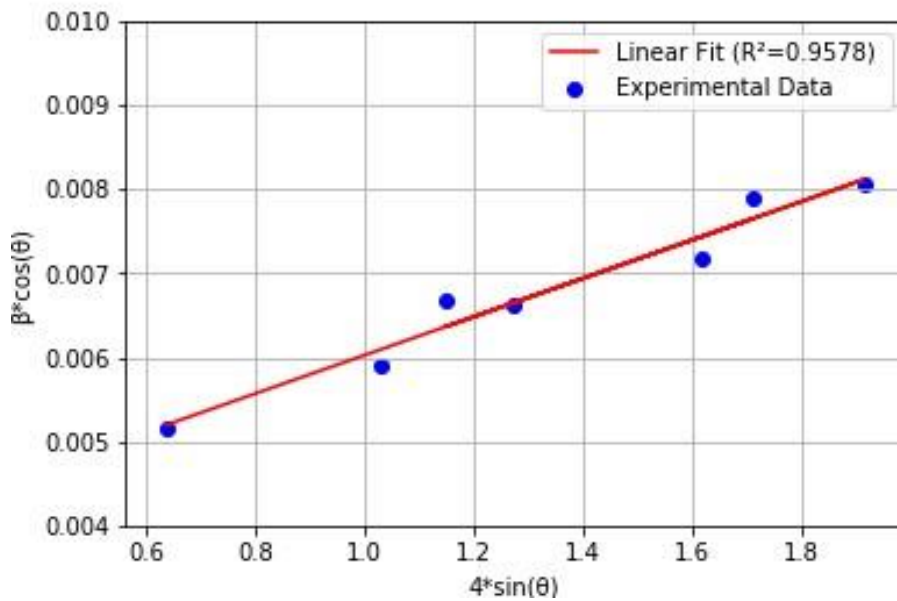
Figure 58: The W-H plot for the Sn oxides sample with 5sec annealing step.

MS731_OP071 (7sec)
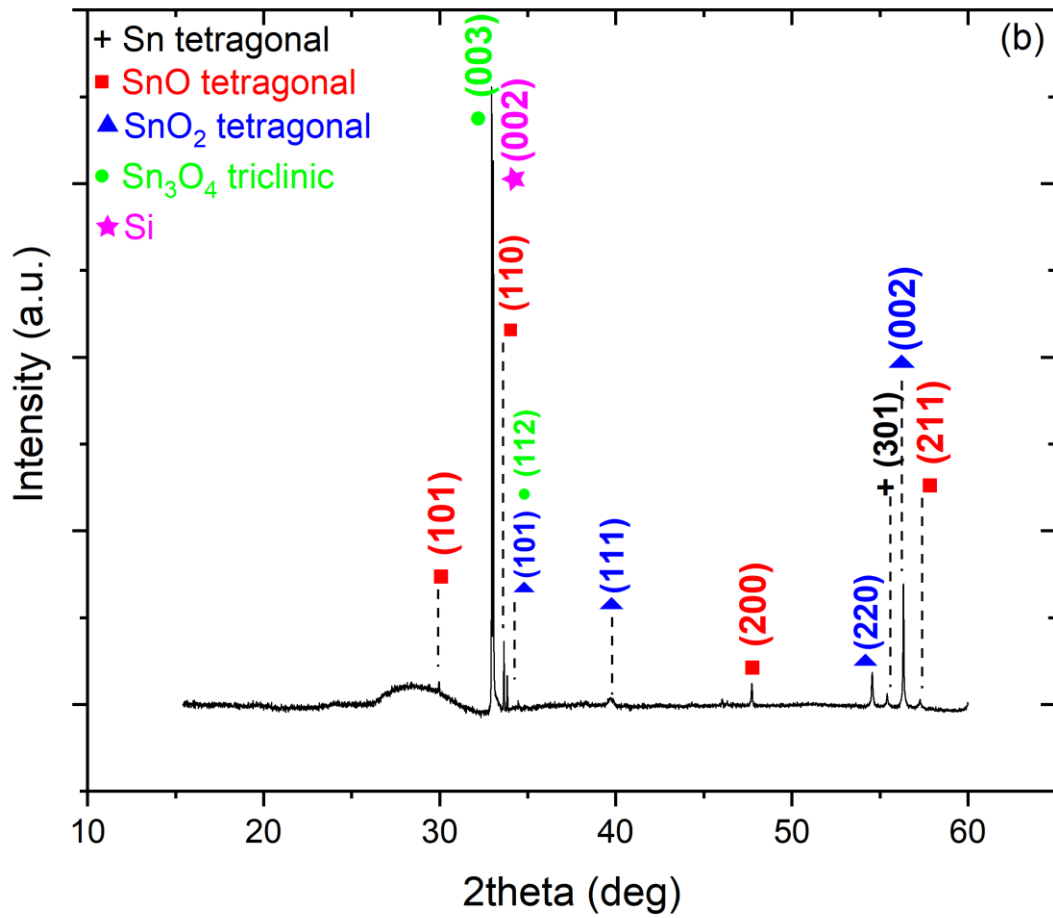
Figure 59: The XRD pattern of the Sn oxides for the 7sec annealing step.
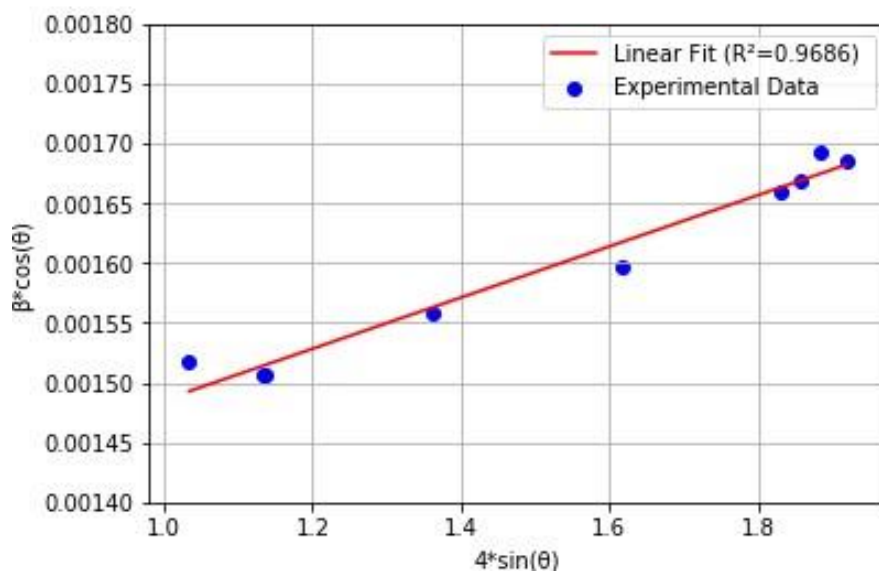
Figure 60: The W-H plot for the 7sec annealing step.

3.1.4 Chemical Characterization of Sn oxides thin films

The X-Rays Diffraction results showed some promising results for the components of the oxides in the films. Both native oxides and the metastable phase Sn_3O_4 coexist uniformly in the layers of the deposited material. Their crystalline structure was also determined by the matching of the diffraction peaks. With the additional use of Photoelectron Spectroscopy, the existence of the corresponding phases can be confirmed. Additively the concentrations of the phases in the surface can be calculated.

With the use Mg anode for the XPS spectra for each sample the survey scan recorded photoelectron peaks and Auger for three different elements: Sn, O and C. The existence of only three elements indicates the cleanliness of the two-step process we followed. High resolution XPS spectra were obtained in the Sn 3d, O 1s and C 1s photoelectron peaks which are considered the main peaks of these elements. The existence of a rich O 1s peak is crucial since the films were oxidized and therefore it is expected the corresponding bonds of Sn and O to be shown as well. The C 1s peak is due to atmospheric elements since there is not perfect vacuum. The survey scan for all the samples remained almost interchangeable indicating that all the samples have been successfully fabricated. It is shown for the sample with 3sec oxidation in the Figure 61 with no differences existing in the other samples.
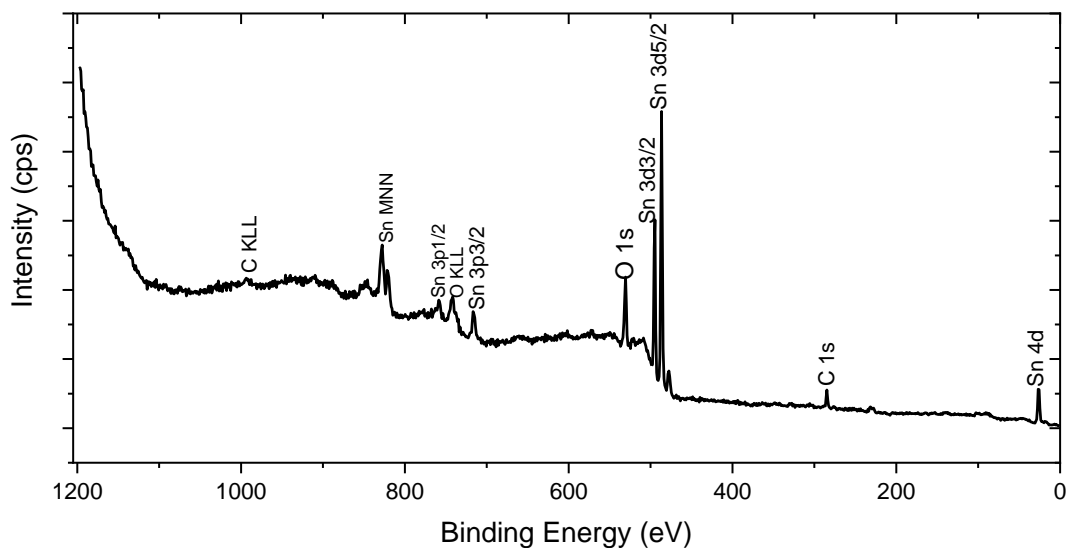
Figure 61: The survey scan for the Sn oxides thin films.

For the main photoelectron peaks high-resolution scan were conducted and by the deconvolution of the Gaussian peaks, complete details about the bonding were matched with the corresponding phases. The Gaussian fitting of the high-resolution peaks was done with CasaXPS v2.3 analysis software, which is suitable for analyzing XPS data directly from the analyzer. From the deconvolution of the peaks a lot of information can be found. In the C 1s peak which exists in all samples the single and double bonds of C and the single bond of C and O can be measured. Additively the C 1s peak was used for the removal of the chemical shift that existed during the scanning. The C 1s peak is depicted in Figure 62 and remains interchangeable for the samples indicating the quality of the vacuum conditions.

72

The interesting part is the deconvolution and the comparison of the O 1s and Sn 3d, the main peaks of O and Sn respectively. From the Gaussian fitting of the Sn $3d_{5/2}$ peak totally three or four phases of the Sn components can be found in fully agreement with the XRD data. Those phases are metallic Sn, SnO, SnO_2 and Sn_xO_y. The Sn_xO_y oxide is highly possible to correspond to the Sn_3O_4 (91) as we expected from the results from XRD. The binding energies of the centers of the Gaussians of each the oxides and the metallic Sn are matching with the expected binding energies from bibliography (47) (92) (93). It is expected the same phases to exist in the Sn $3d_{3/2}$ peak due to spin-orbit coupling with a binding energy difference about 8.4eV. By numerically integrating the deconvoluted high-resolution peaks of the Sn 3d orbital (both $3d_{3/2}$ and $3d_{5/2}$ photoelectron peaks) some first information about the hundredth percentage compositions in the surface can be extracted. The concentrations are calculated automatically by CasaXPS and the mathematical formalization of the integration of the curves is explained at the **APPENDIX A** : XPS Concentrations Script (Sage Math v9.1), where an exemplary code is shown. The results of the high resolution XPS spectra for all samples are shown below.
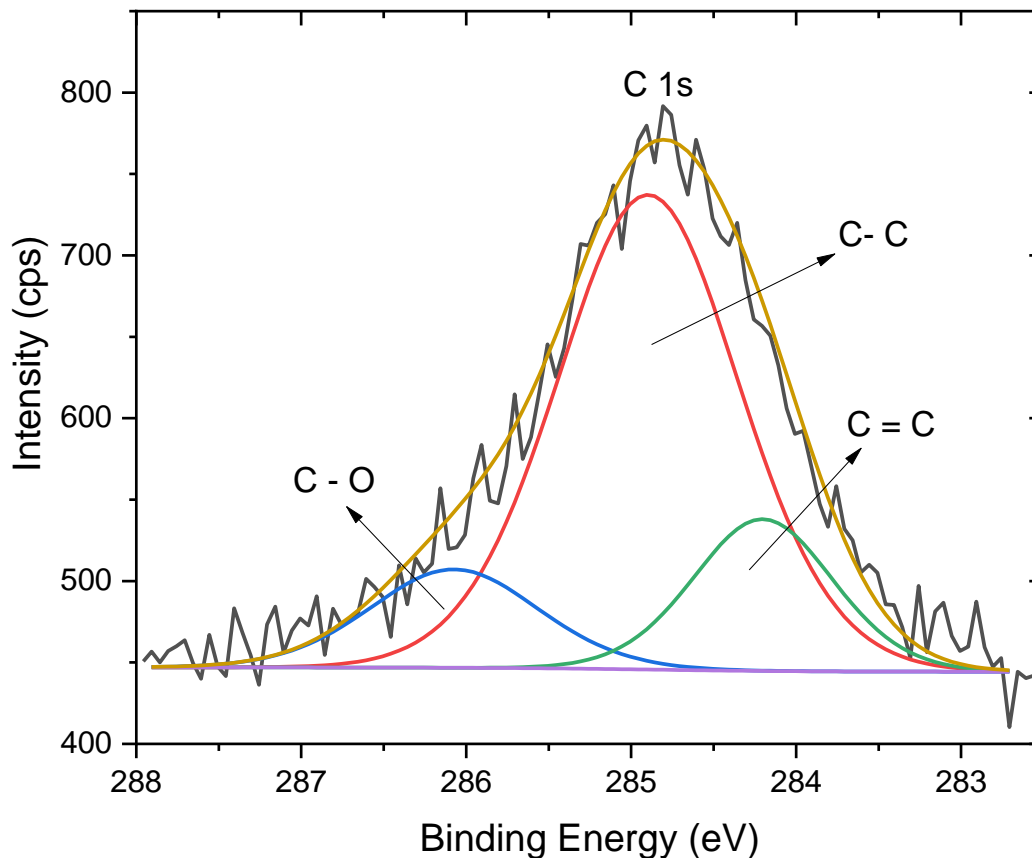
Figure 62: High resolution XPS spectra of the C 1s peak.

Sample MS731_OP070 (3sec)
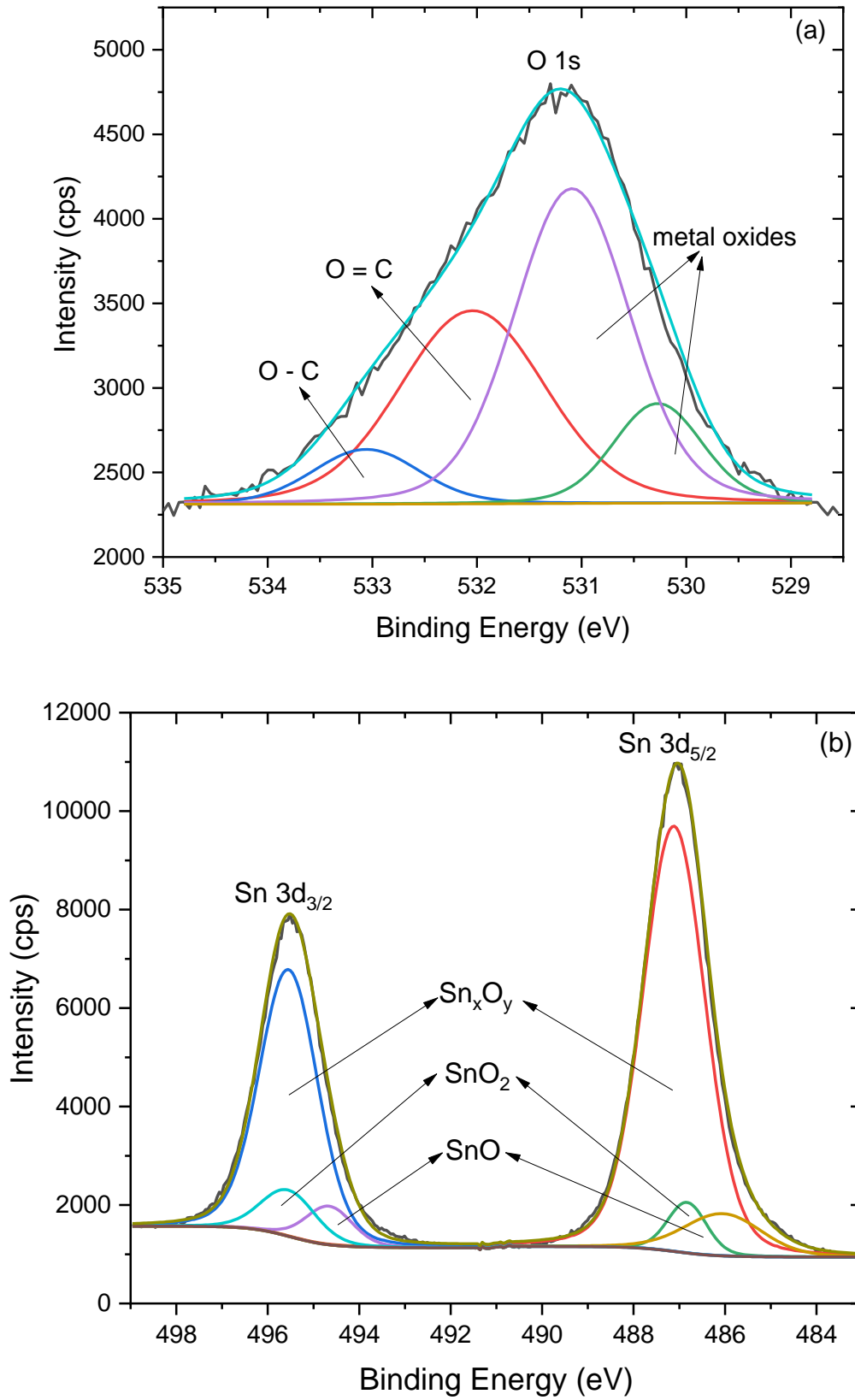
Figure 63: High resolution XPS spectra for the 3sec oxidation step (a) O 1s (b) Sn 3d.

ΜΕΤΑΠΤΥΧΙΑΚΗ ΔΙΠΛΩΜΑΤΙΚΗ ΕΡΓΑΣΙΑ ΟΝΟΜΑΤΕΠΩΝΥΜΟ: ΙΩΑΝΝΗΣ ΠΑΓΩΝΗΣ
ΤΙΤΛΟΣ: Growth and characterization of Type I (Straddling gap) and Type II (staggered gap) heterojunctions alignment in thin films for potential photovoltaic applications
ΠΜΣ-Φυσικής   *Τμήμα Φυσικής*   *Πανεπιστήμιο Ιωαννίνων*

Sample MS731_OP069 (5sec)
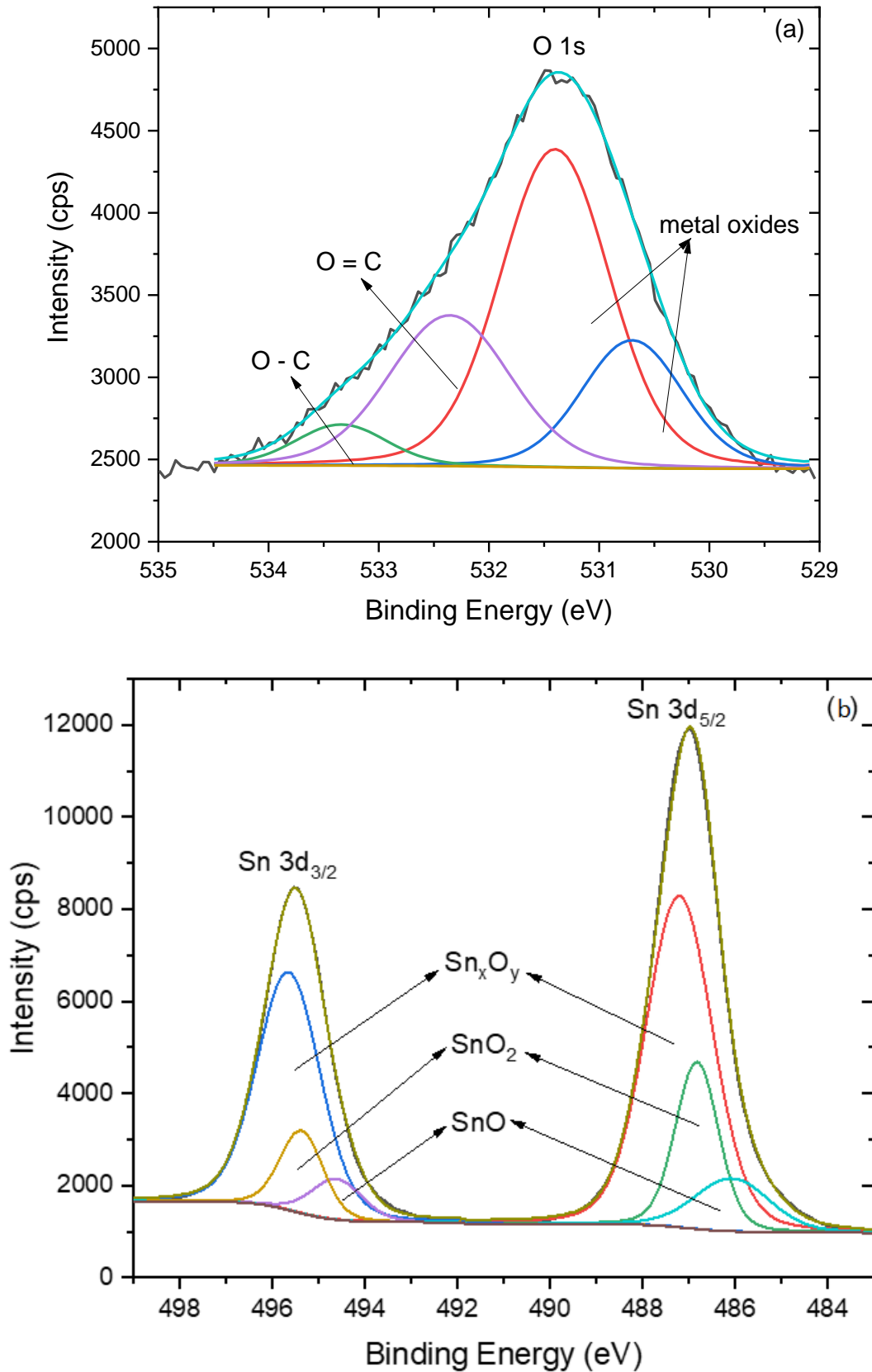
Figure 64: High resolution XPS spectra for the 5sec oxidation step (a) O 1s (b) Sn 3d.

Sample MS731_OP071 (7sec)
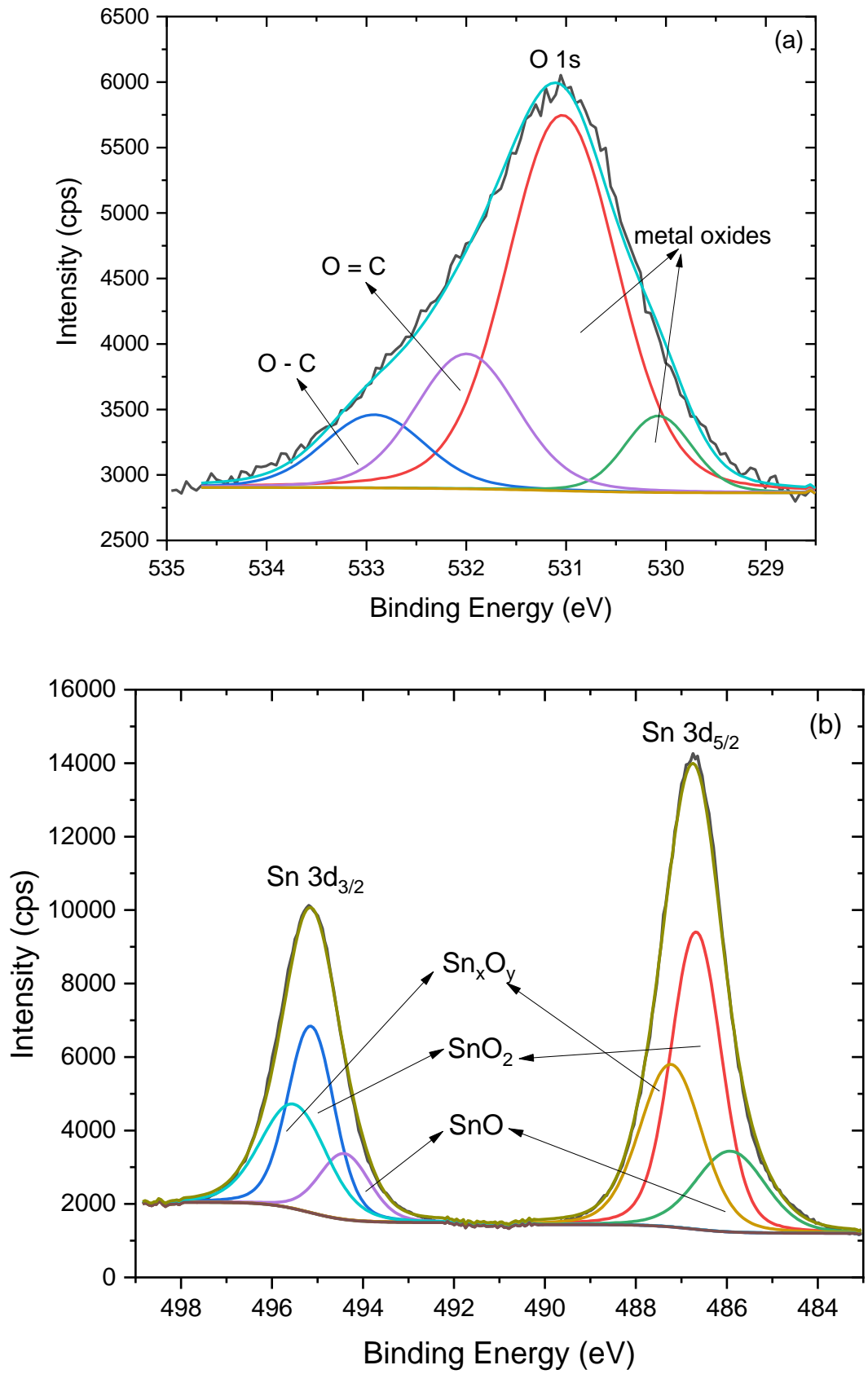
Figure 65: High resolution XPS spectra for the 7sec oxidation step (a) O 1s (b) Sn 3d.

Sample MS733_OP074 (8sec)
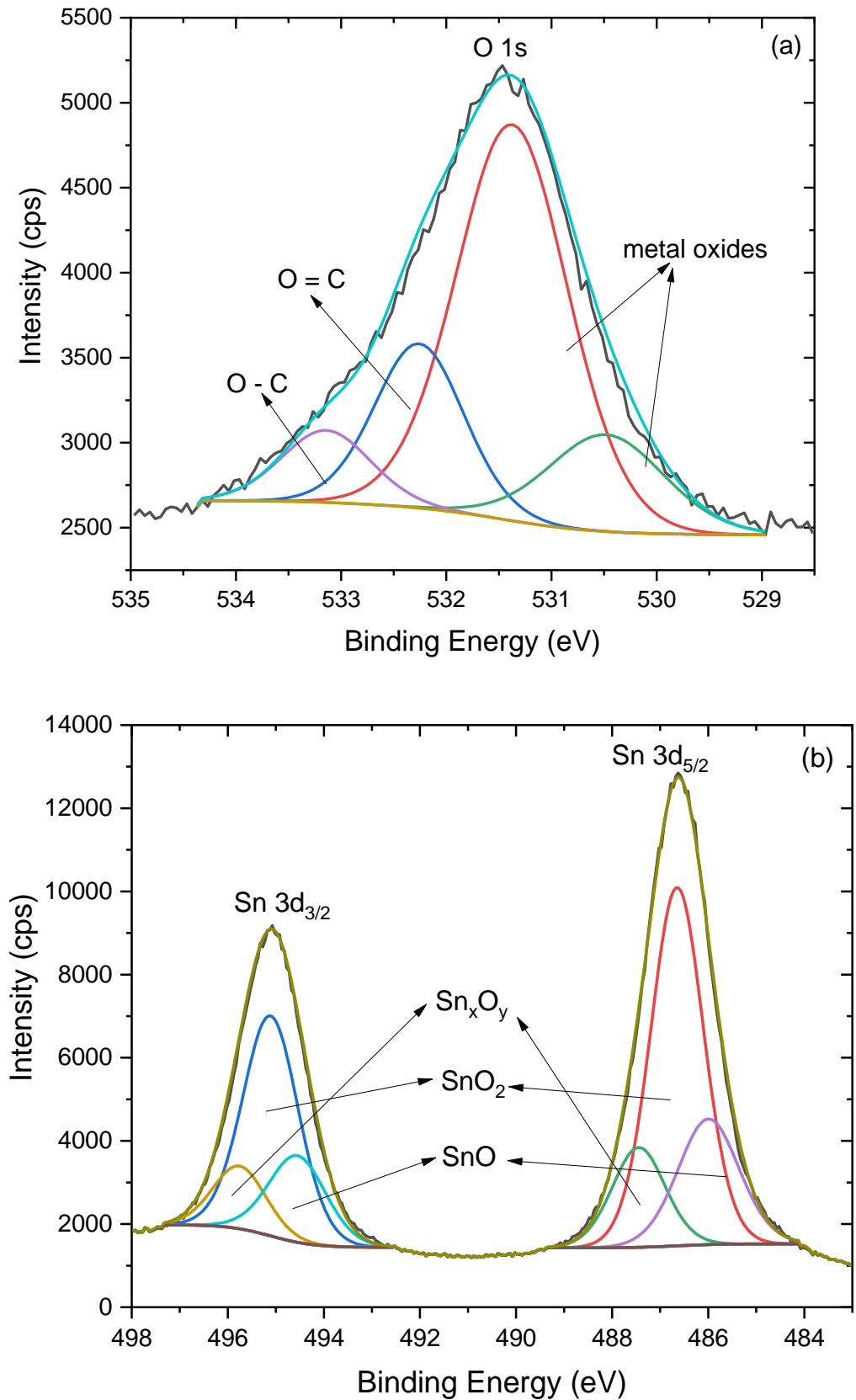
Figure 66: High resolution XPS spectra for the 8sec oxidation step (a) O 1s (b) Sn 3d.

ΜΕΤΑΠΤΥΧΙΑΚΗ ΔΙΠΛΩΜΑΤΙΚΗ ΕΡΓΑΣΙΑ ΟΝΟΜΑΤΕΠΩΝΥΜΟ: ΙΩΑΝΝΗΣ ΠΑΓΩΝΗΣ
ΤΙΤΛΟΣ: Growth and characterization of Type I (Straddling gap) and Type II (staggered gap) heterojunctions
alignment in thin films for potential photovoltaic applications
ΠΜΣ-Φυσικής   *Τμήμα Φυσικής*   *Πανεπιστήμιο Ιωαννίνων*

Sample MS732_OP072 (9sec)
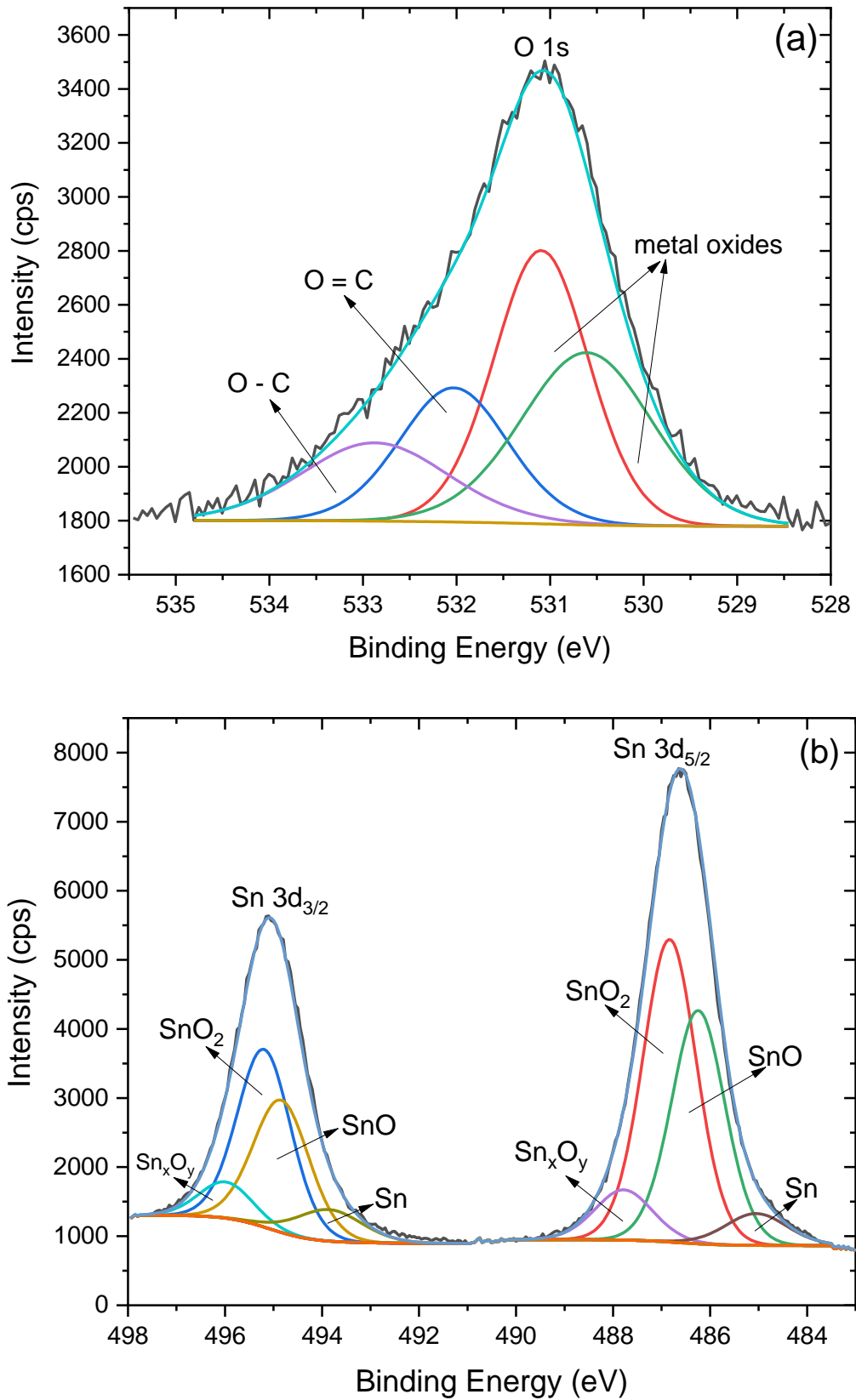
Figure 67: High resolution XPS spectra for the 9sec oxidation step (a) O 1s (b) Sn 3d.

Sample MS732_OP073 (11sec)
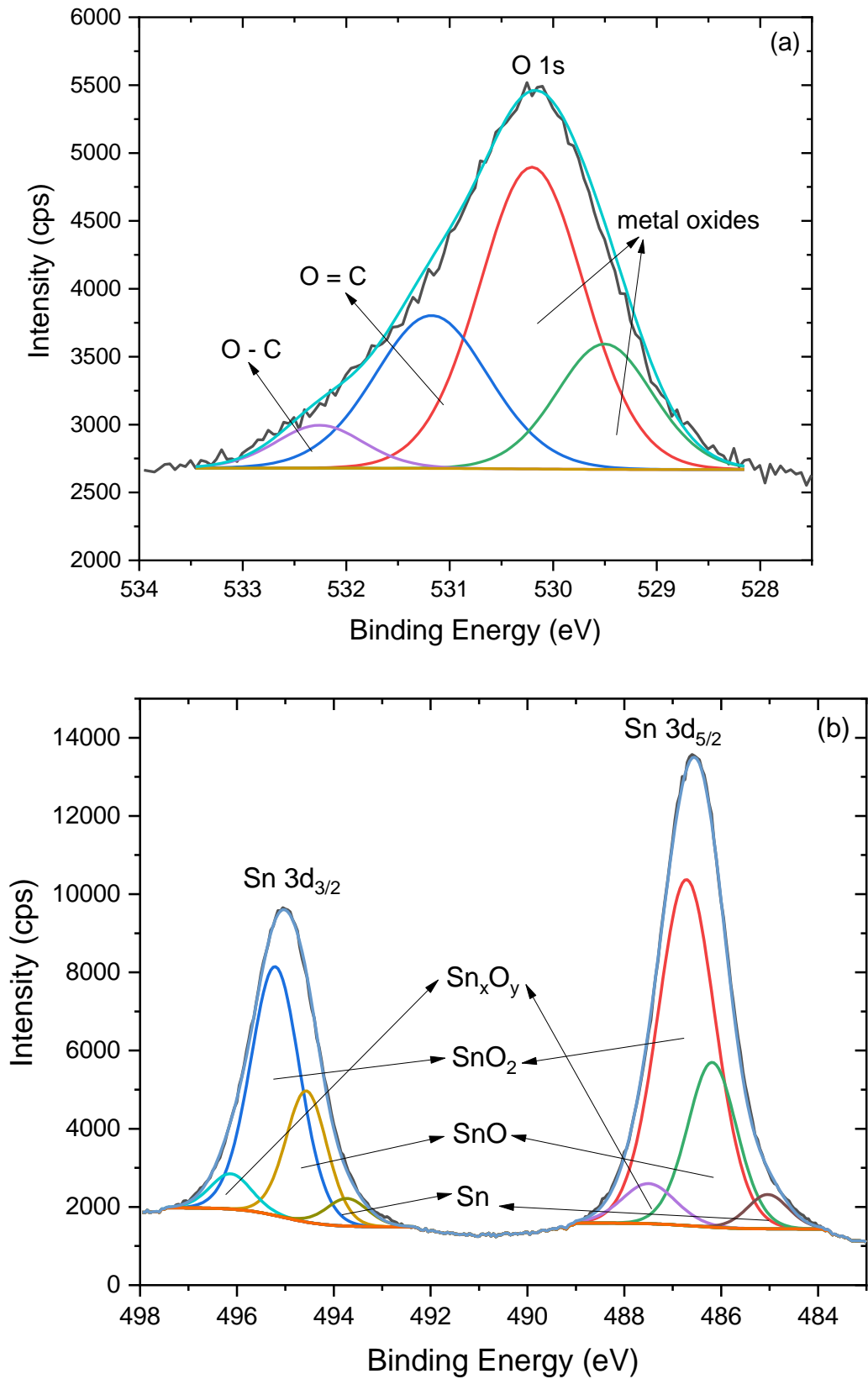
Figure 68: High resolution XPS spectra for the 11sec oxidation step (a) O 1s (b) Sn 3d.

Sample MS733_OP075 (13sec)
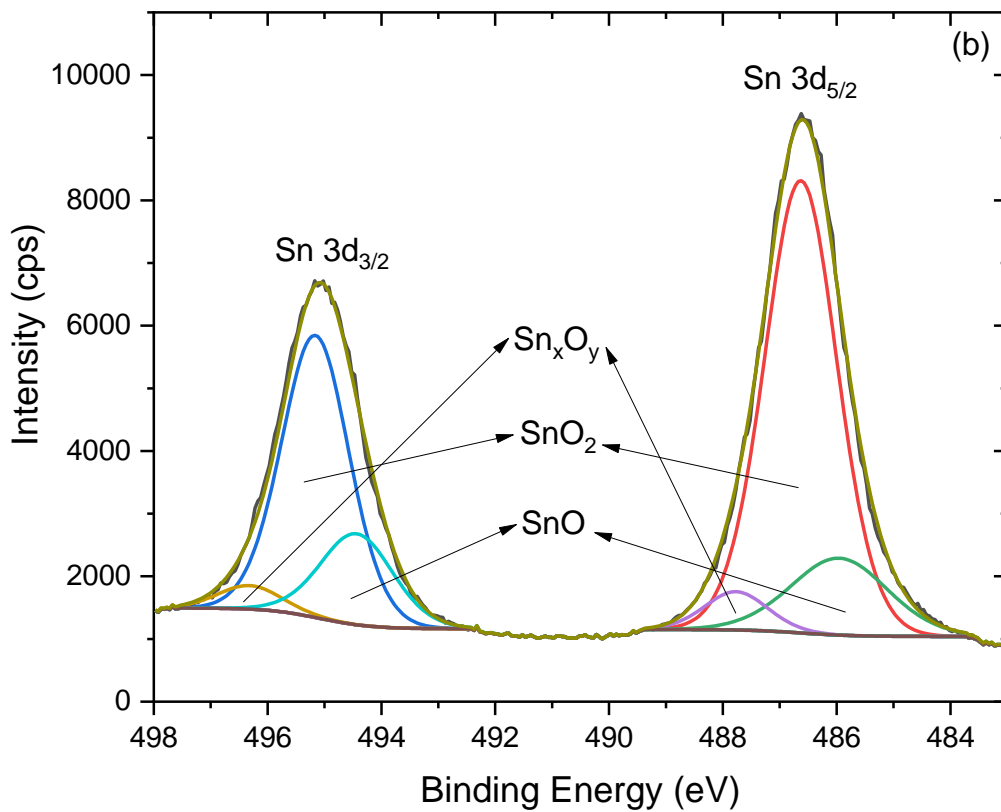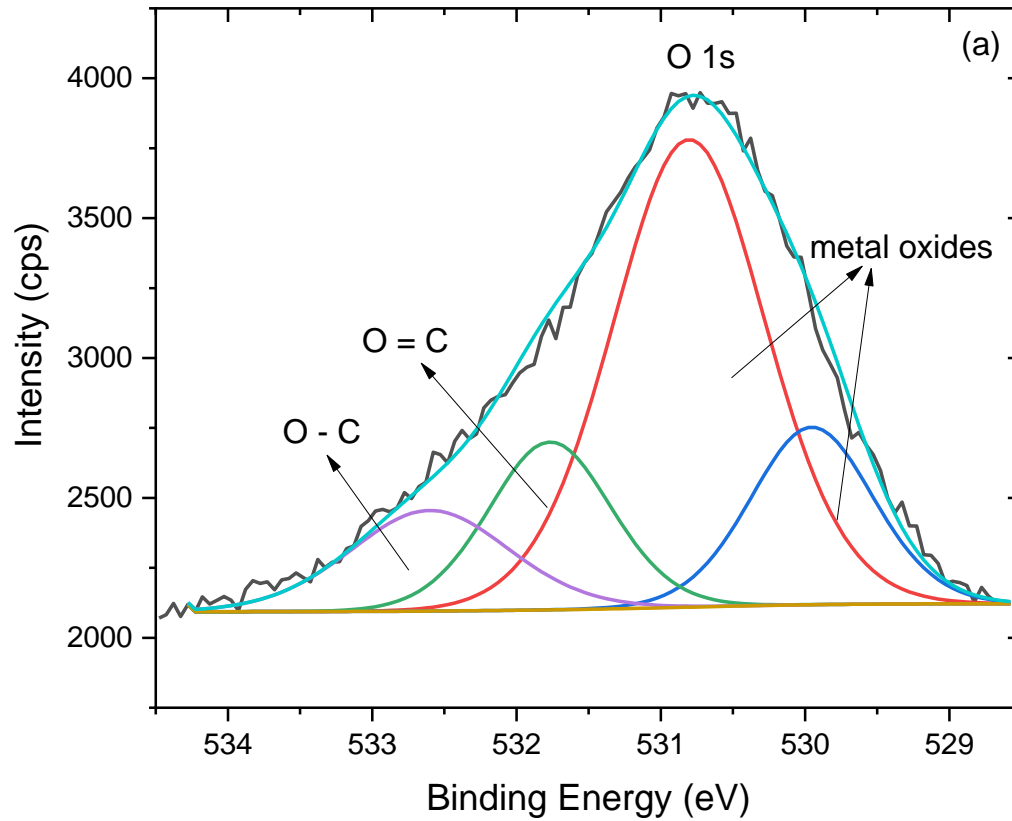
Figure 69: High resolution XPS spectra for the 13sec oxidation step (a) O 1s (b) Sn 3d

From the numerical integrations of the Gaussian fitting of the Sn 3d peak we gain the % (percentage) concentrations of the Sn oxides in the surface. The evolution of the concentration dependence on the oxidation time is depicted in the following graph, Figure 70. As we can conclude the concertation of the metastable oxide is decreasing with the annealing step, which is logical considering the higher temperatures that boost the formation of the main oxides and especially SnO_2. At the 9sec annealing step we have the closest ration of concentrations for the main oxides strongly indicating the maximum heterojunction alignments. The results from the characterization are crucial for the results of the following electrical measurements.
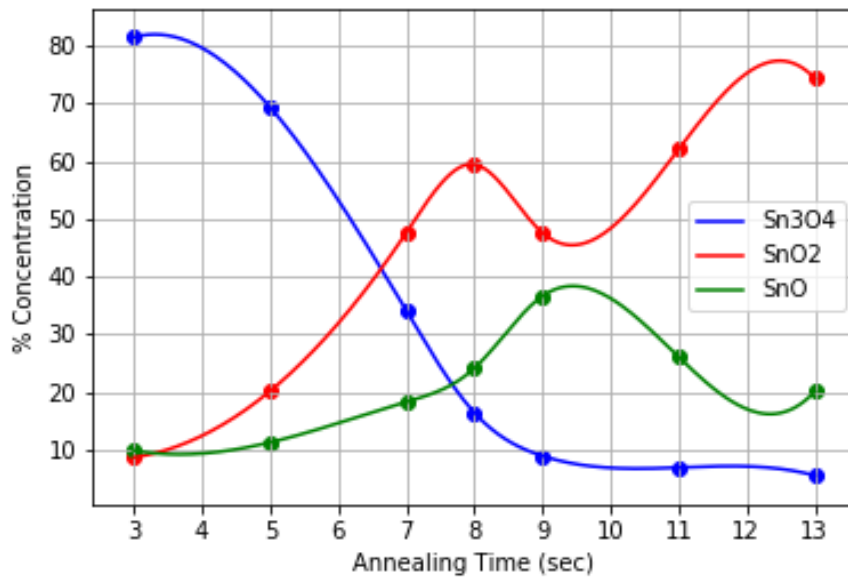
Figure 70: The evolution of the concentrations of the Sn oxides with the annealing step.

3.1.5 Electrical Measurements Results

In this chapter the results from the measurements of the electric properties of the samples are discussed. The I-V characteristics of the thin films were measured in a SUSS Microtek PM5 4-probe station and a Keithley 2400 Source Measuring Unit (SMU) multimeter under three different conditions, dark, yellow light, and white light. A DC power supply provided voltage to the film and the data were recorded with Tektronix Kickstart software with the add on I-V characterizer. The lamp spectra referred as yellow and white are shown in the Figure 71 and they correspond to halogen lamp and cool white LED respectively (94). The spectra of these lamps were already studied for the development of low-light indoor solar cells appliances. The yellow light emits at wavelengths greater than 600nm and it has an intensity of $20W/m^2$, while the white light emits at wavelengths of 450nm and 535nm and has a measured intensity of $450W/m^2$. Hence, both wavelength and lamp intensity affect the maximum current and regardless the annealing step white lamp produces stronger current.

From the electric measurements the average values, which were calculated by averaging each recording cycle, of the I-V are shown in the following graphs, and

they tend to have the characteristic form for a semiconductor interface. In most cases the resulting current attains values surpassing 2mA, especially in the cases of 9 and 11-seconds annealing step.
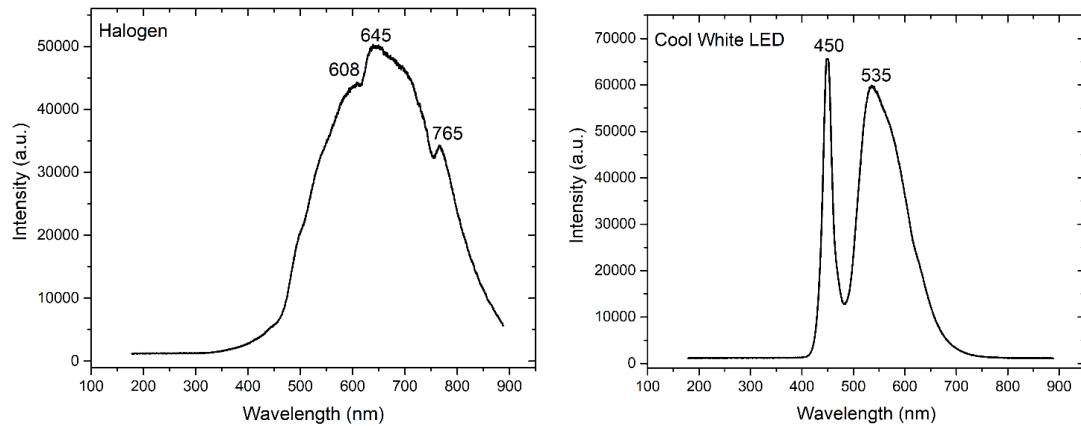
Figure 71: The emission spectra for yellow(left) and white(right) light.

The maximum current of the samples was plotted for V=±8V, and they are at similar values. The n-type semiconducting effects seem to be significantly stronger in the 3sec sample strongly suggesting the effect of the intermediate oxide as an n-type semiconductor. The values of current seem to be weaker for the samples with annealing step 8sec and less for this very reason. The reason seems to be the high concentrations of Sn_3O_4 which can act like an electron trap and decreases the effect of the main oxides heterojunction. The reason behind the behavior of the intermediate oxide as an electron trap is the possible existence of empty vacant oxygen positions and the creation of a new energy state within the range of the energy gap (95).

MS731_OP070 (3sec)
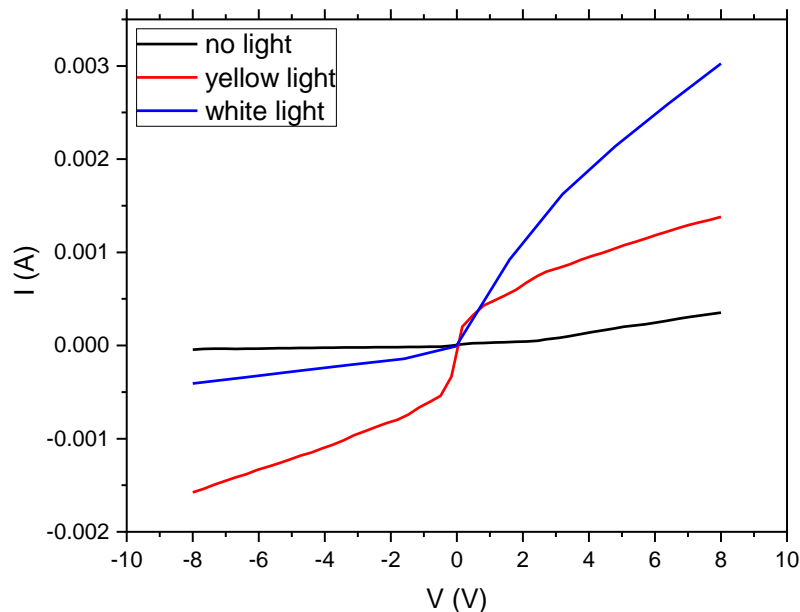
Figure 72: The I-V characteristics of the 3sec oxidation step sample.

ΜΕΤΑΠΤΥΧΙΑΚΗ ΔΙΠΛΩΜΑΤΙΚΗ ΕΡΓΑΣΙΑ ΟΝΟΜΑΤΕΠΩΝΥΜΟ: ΙΩΑΝΝΗΣ ΠΑΓΩΝΗΣ
ΤΙΤΛΟΣ: Growth and characterization of Type I (Straddling gap) and Type II (staggered gap) heterojunctions
alignment in thin films for potential photovoltaic applications
ΠΜΣ-Φυσικής   *Τμήμα Φυσικής*   *Πανεπιστήμιο Ιωαννίνων*

MS731_OP069 (5sec)
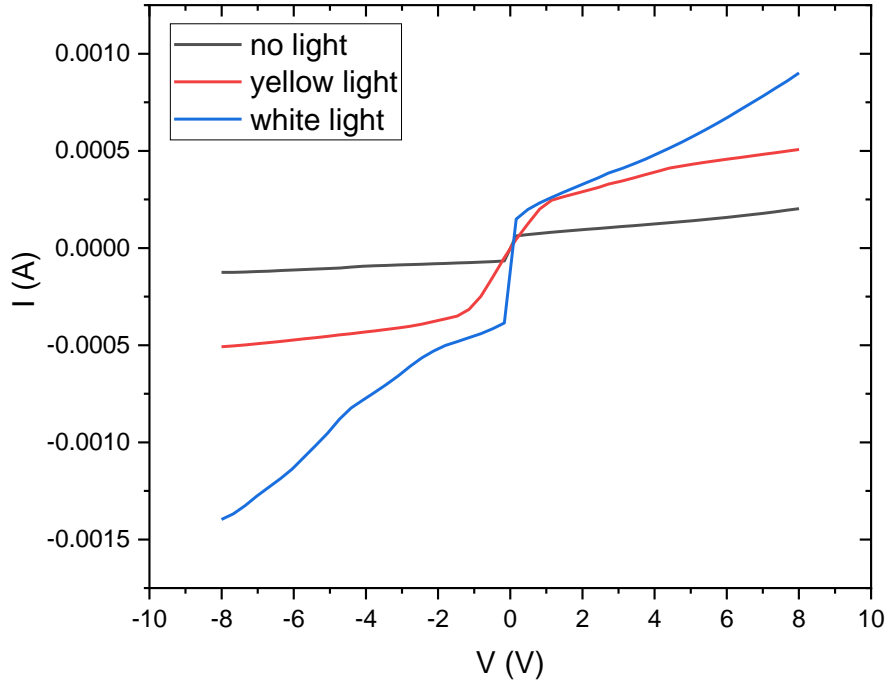
Figure 73: The I-V characteristics of the 5sec oxidation step sample.

MS731_OP071 (7sec)
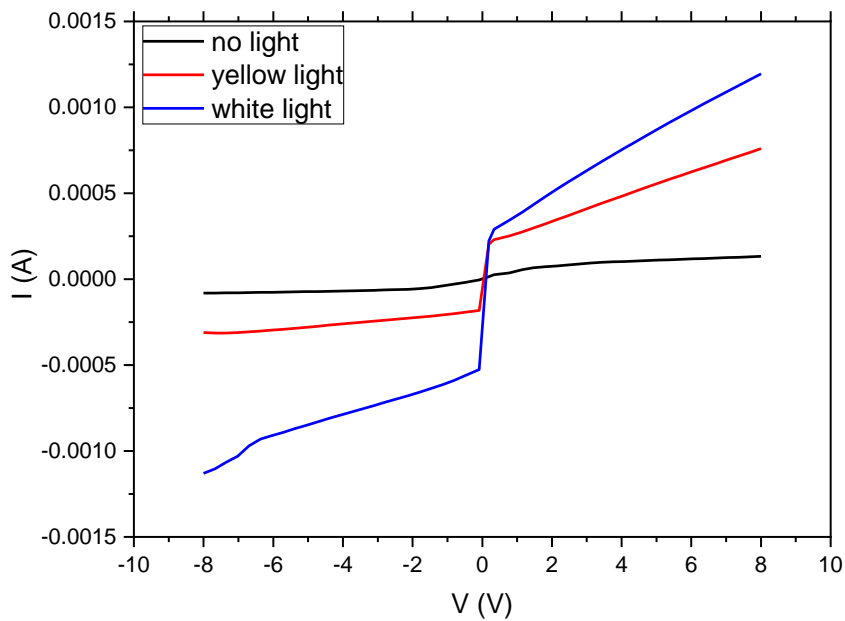
Figure 74: The I-V characteristics of the 7sec oxidation step sample.

ΜΕΤΑΠΤΥΧΙΑΚΗ ΔΙΠΛΩΜΑΤΙΚΗ ΕΡΓΑΣΙΑ ΟΝΟΜΑΤΕΠΩΝΥΜΟ: ΙΩΑΝΝΗΣ ΠΑΓΩΝΗΣ
ΤΙΤΛΟΣ: Growth and characterization of Type I (Straddling gap) and Type II (staggered gap) heterojunctions
alignment in thin films for potential photovoltaic applications
ΠΜΣ-Φυσικής   *Τμήμα Φυσικής*   *Πανεπιστήμιο Ιωαννίνων*

MS733_OP074 (8sec)
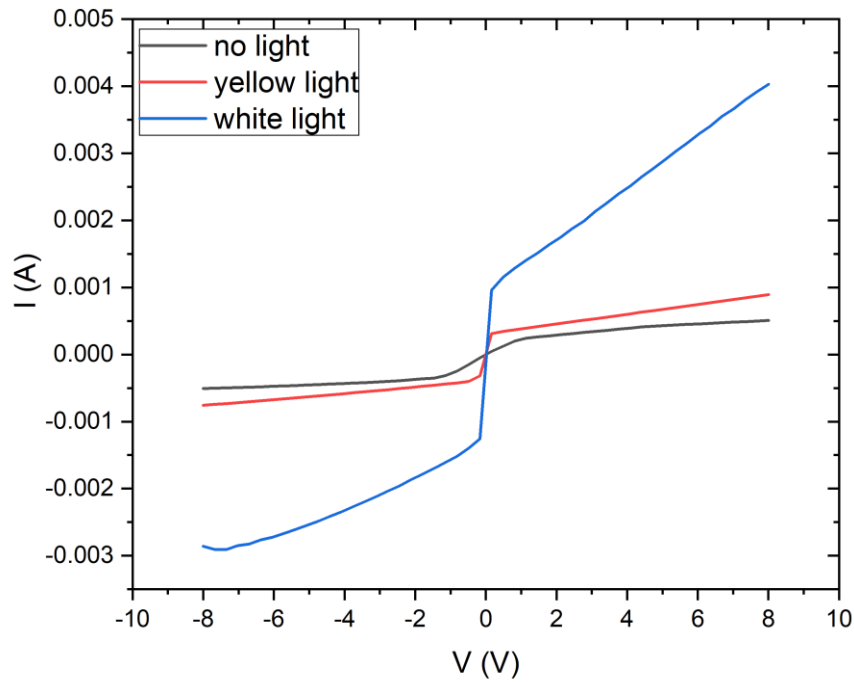
Figure 75: The I-V characteristics of the 8sec oxidation step sample.

MS732_OP072 (9sec)
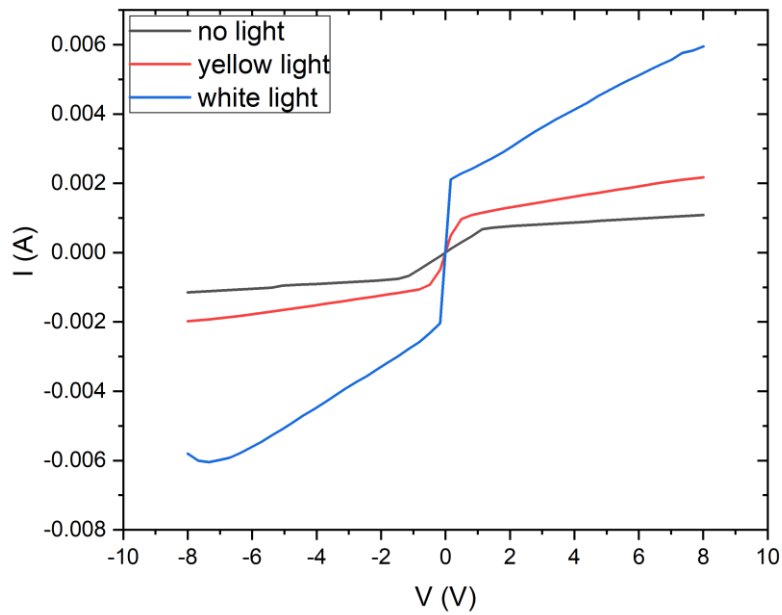
Figure 76: The I-V characteristics of the 9sec oxidation step sample.

ΜΕΤΑΠΤΥΧΙΑΚΗ ΔΙΠΛΩΜΑΤΙΚΗ ΕΡΓΑΣΙΑ ΟΝΟΜΑΤΕΠΩΝΥΜΟ: ΙΩΑΝΝΗΣ ΠΑΓΩΝΗΣ
ΤΙΤΛΟΣ: Growth and characterization of Type I (Straddling gap) and Type II (staggered gap) heterojunctions
alignment in thin films for potential photovoltaic applications
ΠΜΣ-Φυσικής   *Τμήμα Φυσικής*   *Πανεπιστήμιο Ιωαννίνων*

MS732_OP073 (11sec)
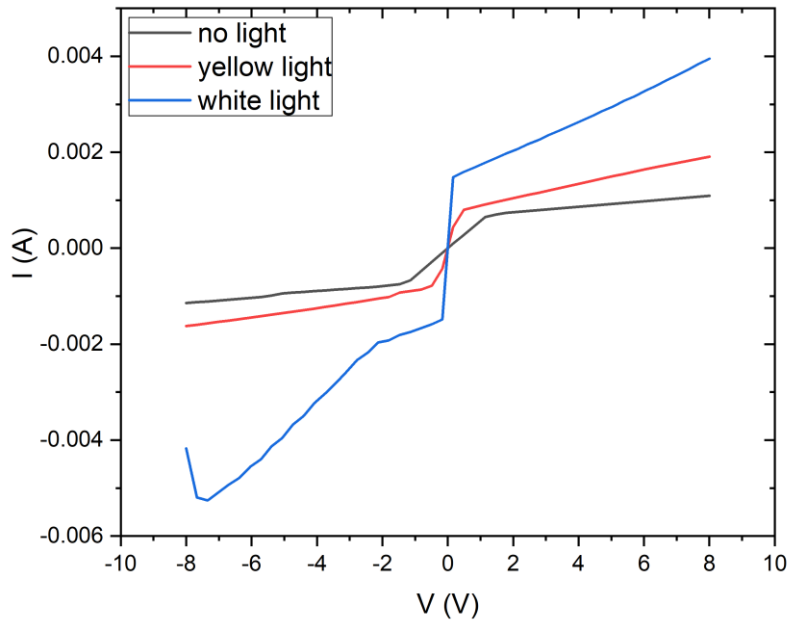
Figure 77: The I-V characteristics of the 11sec oxidation step sample.

MS733_OP073 (13sec)
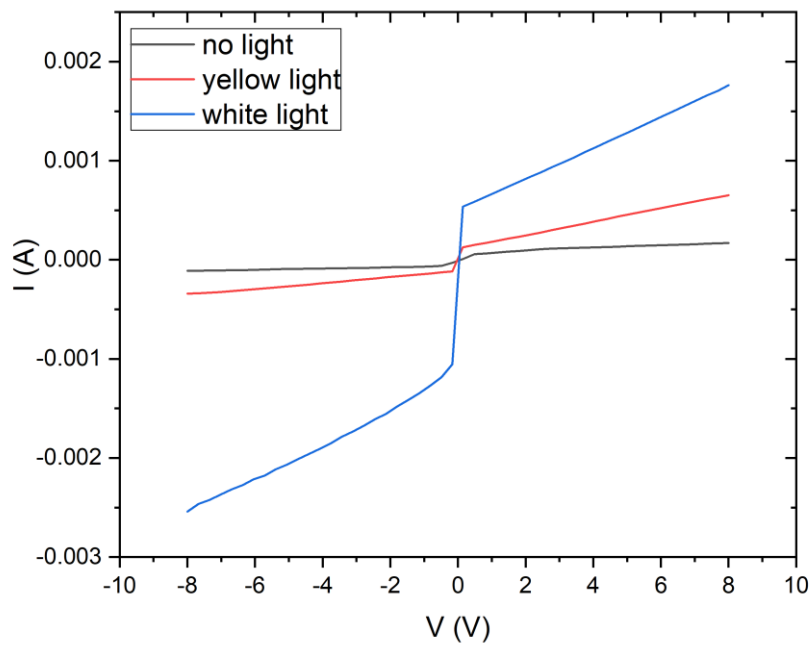
Figure 78: The I-V characteristics of the 13sec oxidation step sample.

For the samples the evolution of the maximum current for each oxidation step for V=±8V is shown in Figure 79:
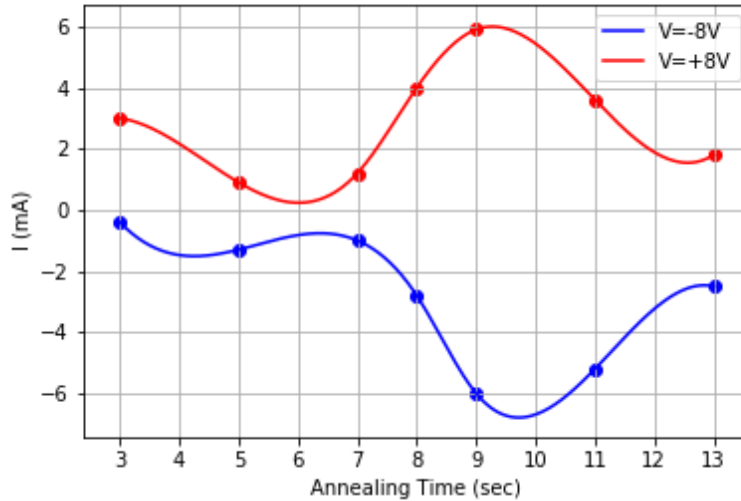
Figure 79: Maximum current evolution depending on the annealing step.

Additional electrical measurements were conducted in the samples for determining their photoresponse properties as potential photovoltaic or photosensing devices under real sun conditions. The measurements were based in checking their photocurrent change in illumination on and off conditions for a certain period. The photorepsonse measurements were done with the use of Sciencetech Inc 550-200-PS solar simulator in 2-probe mode. The solar simulator contains a Osram XBO 150w/cr Xenon lamp with intensity of (100mW/cm^2) with an AM 1.5 filter with an emission spectrum of 200-900nm as it is depicted below, Figure 80.
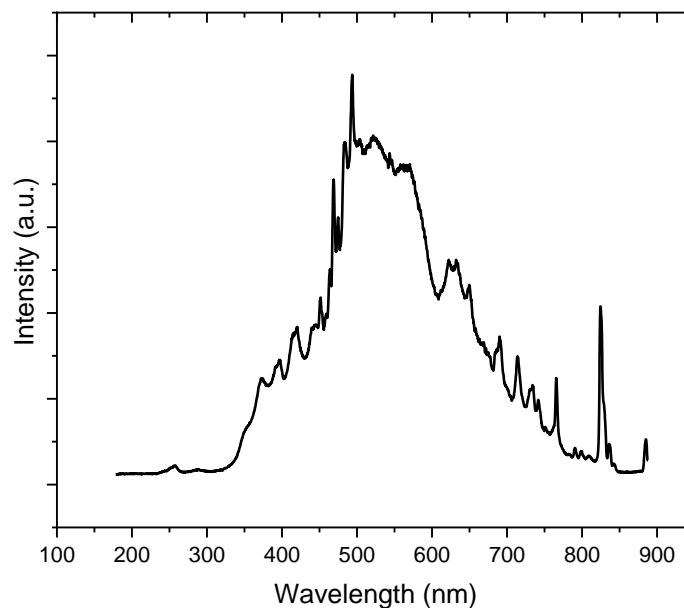
Figure 80: The spectra of the solar simulator lamp with the effect of AM1.5 filter.

For all the samples three minutes of illumination time of one Sun and three minutes of dark conditions were used as conditions with additional 30sec dark at the first cycle. The process was repeated for three cycles for determining if the phenomenon of photoresponse is repetitive. The results of normalized photocurrent response are shown in the Figure 81 in which we can realize that the Sn oxides as-grown thin films have behavior totally responsive to the drastic light changes making them suitable as potential photodetecting devices. The normalized photocurrent or photocurrent density (J) is the amount of current generated for a specific area of the film and it can also be referred as photocurrent density.

Comparing the results, we observe that the samples up to 7sec oxidation step we have lower photodetecting properties as we can conclude from the I-V characteristics as well because of the smaller current density increase upon illumination. Additionally, their required time for reaching saturation is much longer. For the samples from 8sec and more not only we have major increase in the photocurrent, the saturation also is rapid. The rise and recovery times of the samples indicate that they show excellent photoresponse properties. As rise time is named the necessary time for the current to rise from the 10% to the 90% of its maximum value, with recovery time to be named the opposite property (96) (97). At Figure 82 a schematic for the 7sec step and its characteristic photoresponse values is depicted. The results for the estimated photoresponse times are shown in Table 4. The samples with annealing step of 8sec and greater are exhibiting excellent photoresponse results with rise times smaller than one sec. The reason behind this drastic boost is the decrease of the concentration of the intermediate oxide (Sn_3O_4) which seems to act as an electron trap (95) which is a major handicap for the samples, as we also concluded from the evolution of maximum current of I-V characteristics. The results for voltage of 1V are the following:
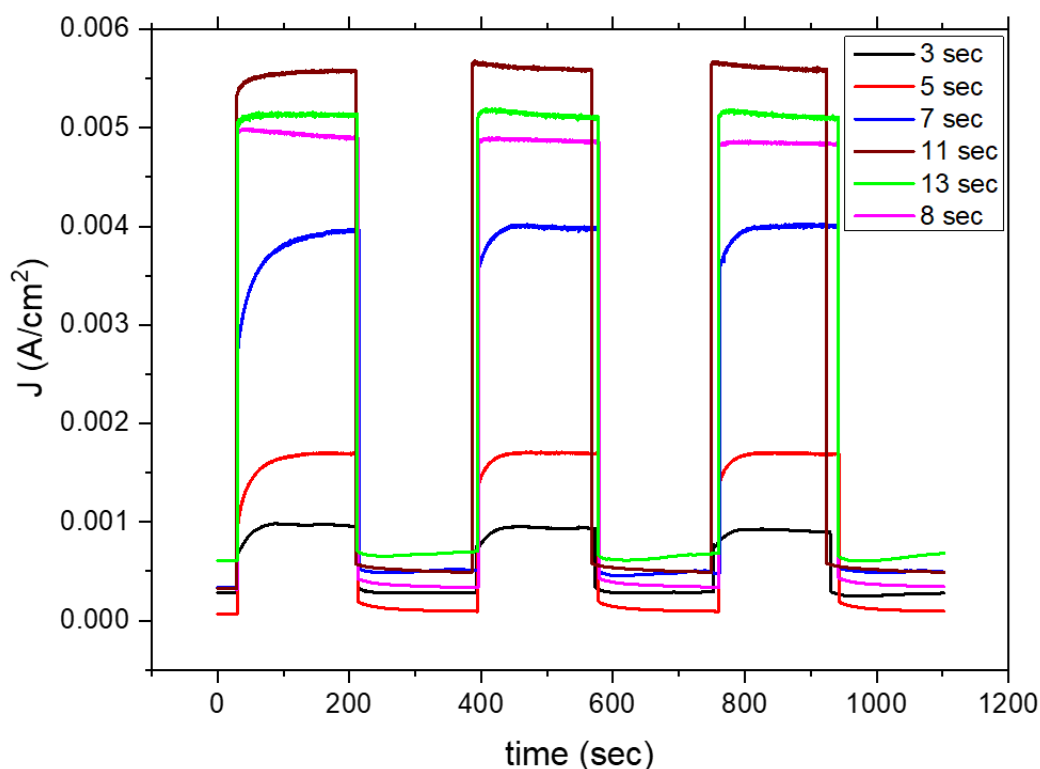
Figure 81: Photoresponse curves of the samples for V-+1V.

ΜΕΤΑΠΤΥΧΙΑΚΗ ΔΙΠΛΩΜΑΤΙΚΗ ΕΡΓΑΣΙΑ ΟΝΟΜΑΤΕΠΩΝΥΜΟ: ΙΩΑΝΝΗΣ ΠΑΓΩΝΗΣ
ΤΙΤΛΟΣ: Growth and characterization of Type I (Straddling gap) and Type II (staggered gap) heterojunctions alignment in thin films for potential photovoltaic applications
ΠΜΣ-Φυσικής   *Τμήμα Φυσικής*   *Πανεπιστήμιο Ιωαννίνων*

For the samples the rise and recovery times are estimated at the following table.

Oxidation Step (sec)	J_{max} (A/cm^2)	Rise Time (sec)	Recovery Time (sec)
3	9.7×10^{-4}	42.00	4.60
5	0.0017	34.00	4.00
7	0.0040	40.00	0.60
8	0.0049	0.80	1.00
11	0.0056	0.04	0.06
13	0.0051	0.11	0.07

Table 4: Characteristic values for the photo response measurements of the samples.
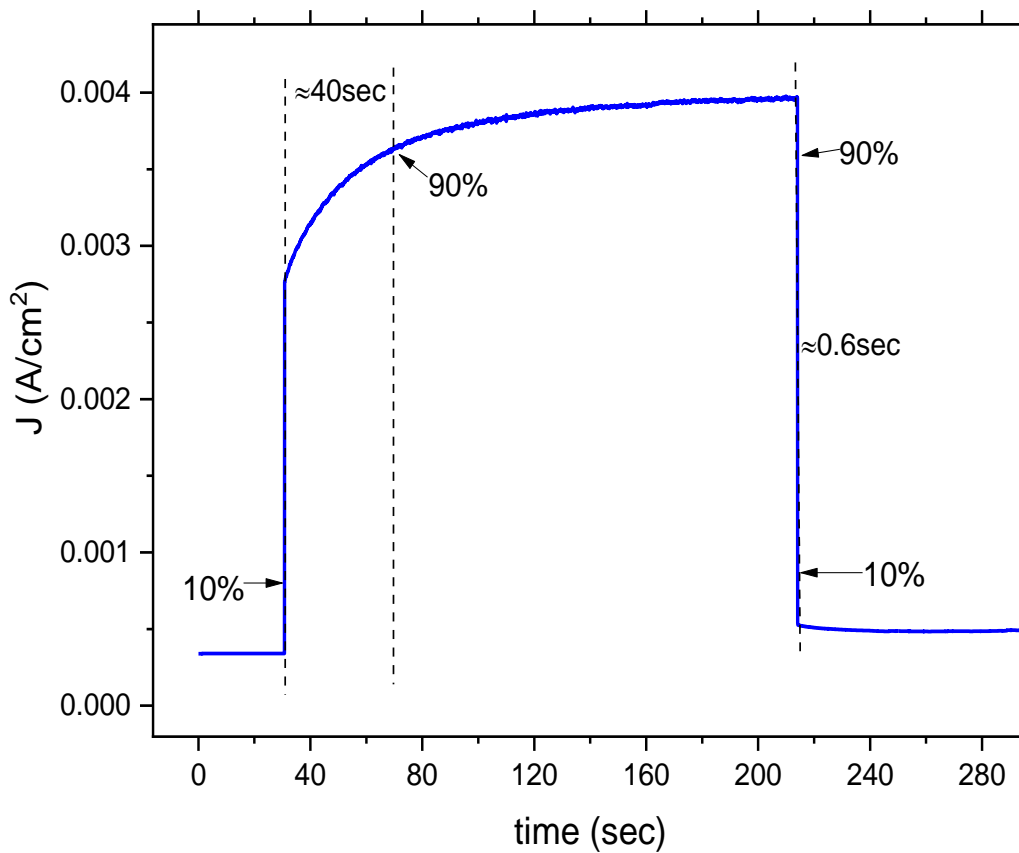
Figure 82: The photoresponse characteristics of the 7sec step sample.

Additional measurements were conducted to the 11sec sample with increased bias to 2V, Figure 83. The comparison showed that the photocurrent was increased about 1.7 times showing very positive results for the sample's evolution as potential photodetecting devices.
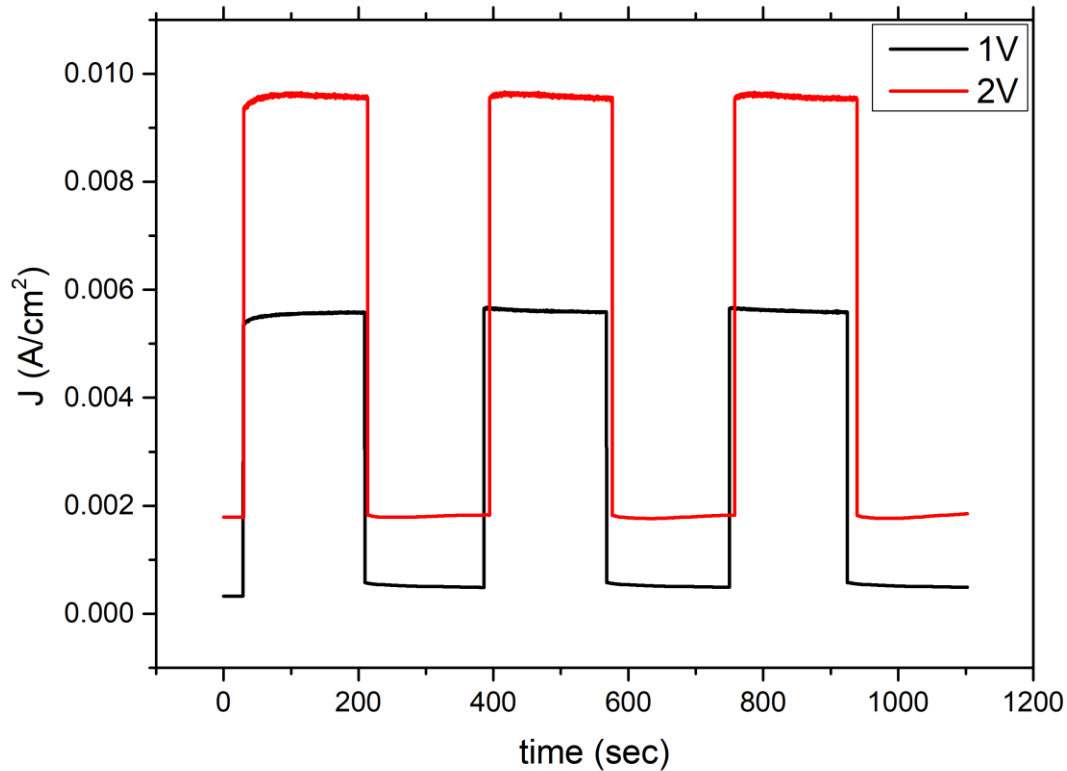
Figure 83: Photoresponse plots for the 11sec sample for V=+1, +2V.

3.2 Experimental Results for Zr-Ti-Cu Thin Films

3.2.1 Two Step Growth Method

The second category of the materials we choose will be presented in this chapter. The same philosophy of the two-step process was used as well. For the growth of the alloys the dual source RF/DC magnetron sputtering was used. As a buffer layer we deposited an alloy of Zr-Ti-Cu which is characterized as a metallic glass. The reasoning behind the material selection was about the formation of the resulting Type I heterojunction. The pressure of the vacuum chamber was around 2.5×10^{-5}mbar. All the samples follow a certain sputtering process for easier comparison of their results, which is characterized by deposition of metallic Zr supported by 50W DC power and metallic Ti supported by RF power at 60W with a frequency of 13.5MHz. Also, two Cu foils were placed onto the surface of the Zr target. High purity Ar gas (99.999%) was inserted in the chamber dropping the base pressure to a working pressure of 2.7×10^{-2}mbar for a fixed gas flow of 50sccm. The growth was conducted for a total deposition time of 20 minutes for the alloys buffer layer. The presputtering of the chamber was performed for a total of 10min in the same conditions.

For the second step of the two-step procedure, the as-grown Zr-Cu-Ti metallic glasses were annealed in oxygen plasma. The plasma chamber is consisted of a borosilicate glass tube supported by rotary pump with vacuum conditions of 3.3×10^{-2}mbar. Inside the chamber high purity O_2 gas (99.999%) was inserted, and the pressure changed to 7.4×10^{-2}mbar. The samples were oxidized for a total of 15sec annealing time with a power supply of 500W forming oxygen plasma in H mode (81).

89

3.2.2 Structural Characterization of Zr-Ti-Cu oxides thin films

A first identification of the crystal structures of the annealed Zr-Ti-Cu alloys was conducted by performing measurements of X-Ray Diffraction (XRD). Both metallic alloys and annealed films were measured in the same diffractometer with the Bragg-Bertrano geometry consisting of a Cu X-Rays tube (λ=1.5406Å). An angular range from 15º to 65º was scanned for the oxides. The XRD pattern of the Zr-Ti-Cu alloys is depicted in the following Figure 84 and it attains an amorphous metallic glass nature because of the disorientations formed from the multiple crystal structures (29) (30).
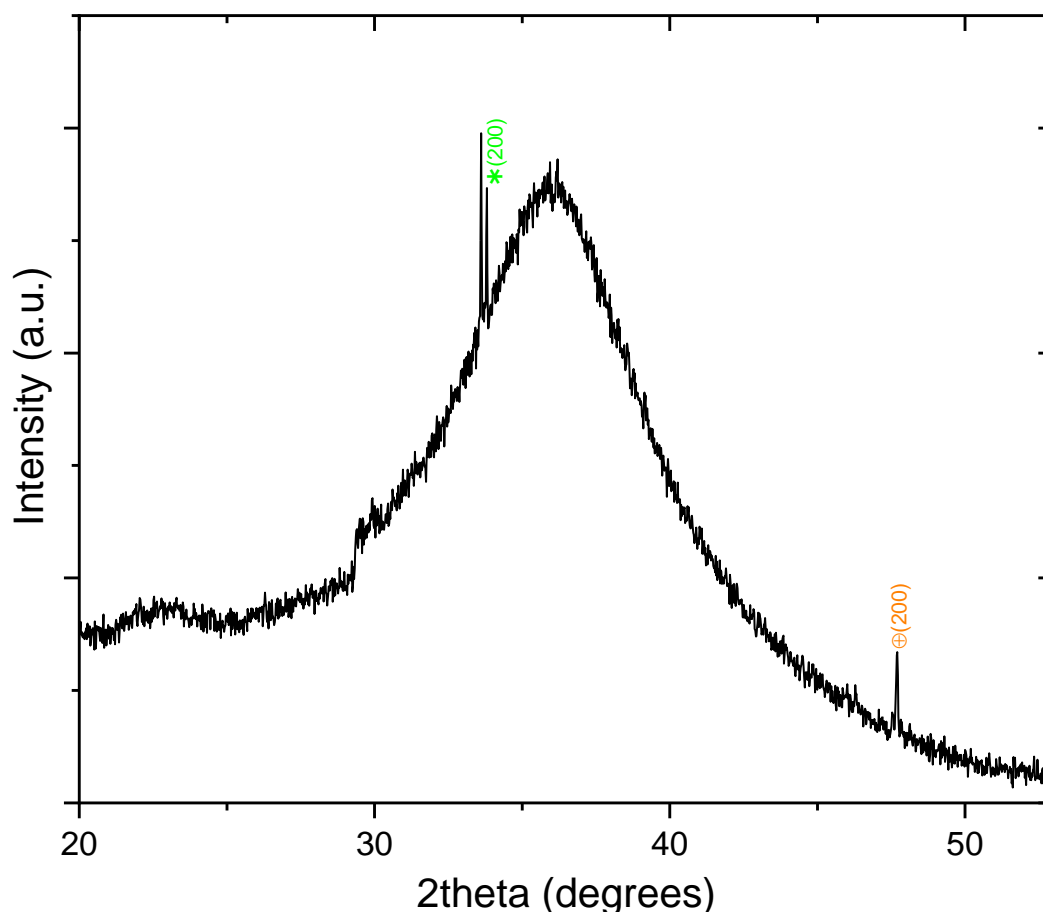
Figure 84: The XRD pattern of Zr-Ti-Cu alloys indicating amorphous structure.

The diffractogram from the oxidized Zr-Ti-Cu alloy is shown in Figure 85. As for the Zr-Ti-Cu oxides, with the peak identification from the bibliography, it occurs that the oxidized thin films have different crystal structures, as expected from the annealing process of plasma treatment. The results correspond to the Cooper oxides (CuO, Cu_2O), Titanium dioxide (TiO_2) and Zirconium Dioxide (ZrO_2) in both tetragonal and monoclinic crystal structures. The extra peaks from the Si substate in the patterns indicate the Bragg-Bertrano geometry's downside in the measurement of thin films. For the Cooper oxides characteristic peaks we detect the (110) and (220) for the Cu_2O at the body centered cubic structure (98) and as for the CuO, the (110), (11$\bar{2}$) and ($\bar{1}$13) peaks at the monoclinic structure corresponding to the tenorite mineral- (99) (100). For the TiO_2 we find two peaks at the tetragonal anatase structure

corresponding to the (200) and (204)- (101). Meanwhile for the TiO_2 rutile tetragonal structure we have peaks for the (211), (220), (002) and (310) directions- (102). As for the ZrO_2 peaks we have two crystal structures the monoclinic and the tetragonal with their respective peaks at (200), (220), ($\bar{1}$22), (122), ($\bar{1}$13), (311), (230) for the monoclinic structure- (103) and (001), (112), (200), (202) for the tetragonal structure- (104) (105). The existence of the main peak of tetragonal ZrO_2 indicates its excessiveness over the other oxides. The prevalence of ZrO_2 in tetragonal structure in small annealing times has already been shown in other recent works (30). Also, the lack metallic peaks were matched since the buffer layer was amorphous indicating fully oxidation of the surface.
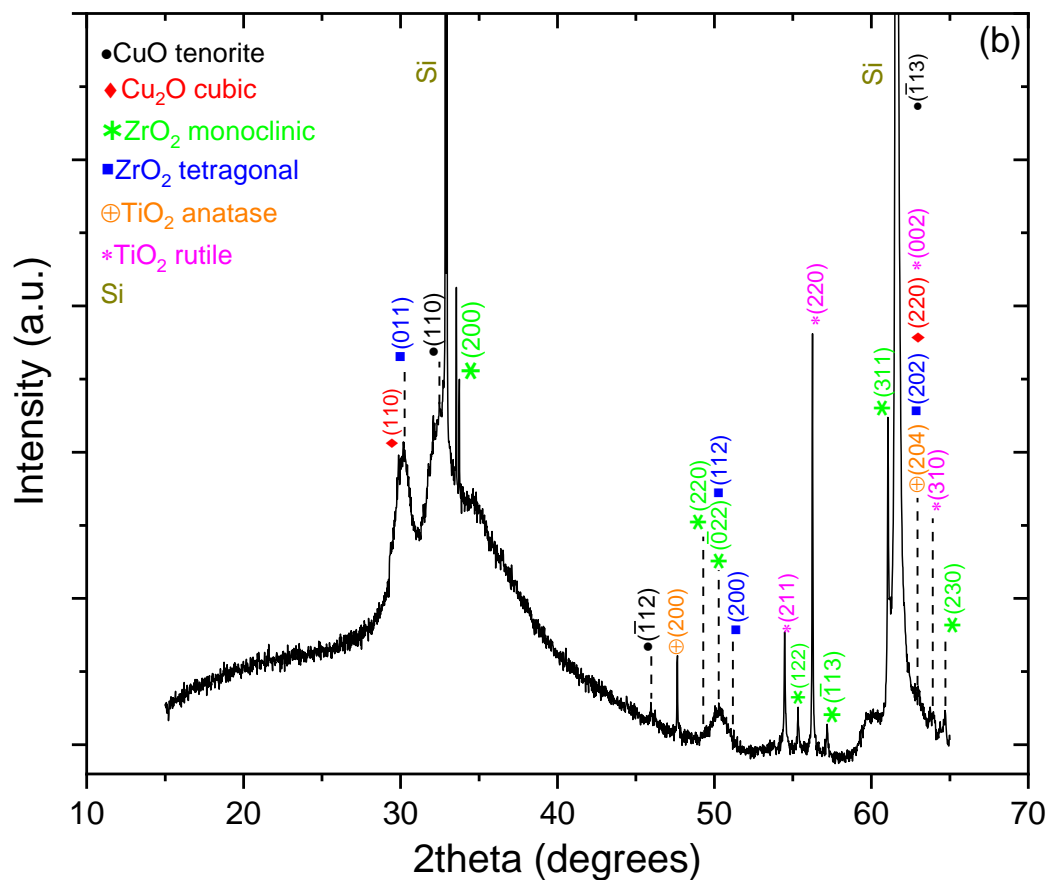
Figure 85: The XRD pattern of the Zr-Ti-Cu Oxides thin films.

By evaluating the characteristics of the diffraction peaks (position and FWHM) we used the Scherrer's formula (eq. 3.6) to estimate the average grain size of the sample with a value around 55nm.

3.2.3 Chemical Characterization of Zr-Ti-Cu oxides thin films

By performing X-Rays Photoelectron Spectroscopy measurements (XPS) we chemically characterized the as-grown samples. Additionally, we performed a first elemental composition of the phases concentrations in the surface. The XPS spectra were measured with the use of Mg anode (1253.6eV). Five different elements were identified from the survey scan of the samples: Zr, Ti, Cu, O and C. The identification

of these elements indicates that the two-step process used for the fabrication of the as-grown samples has not produced any impurities. The three metallic elements correspond to the sputter targets indicating the successful deposition of the alloy, the strong O peak the successful oxidation and C detected as atmospheric element. The survey spectrum is shown below, Figure 86:
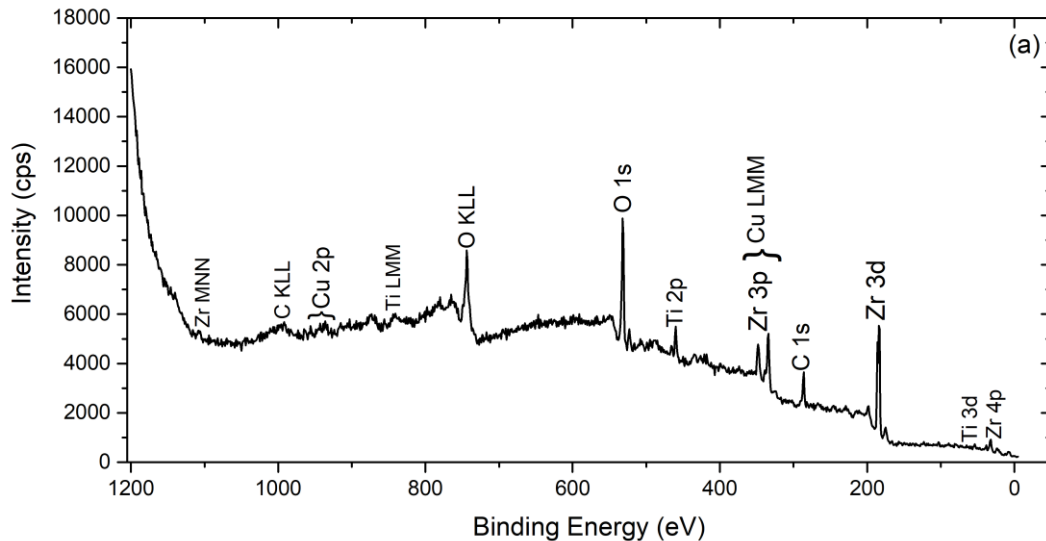
Figure 86: (a) The survey spectra of the oxidized Zr-Ti-Cu thin films.

High-resolution XPS spectra from the main peak of each element were measured for the Zr-Ti-Cu oxides. The spectra were measured for the Zr 3d, Ti 2p, Cu 2p, O 1s and C 1s orbitals. The detected photoelectron peaks were deconvoluted with Gaussian fitting by using the CasaXPS v2.3 analysis software. For the Zr, the $3d_{5/2}$ peak was detected at 182.0eV and the $3d_{3/2}$ at 184.4eV, a strong indication the presence of ZrO_2 oxide (Zr^{4+} state) according to bibliography (29) (30) (106). Also, the Ti $2p_{3/2}$ peak wad detected at 458.3eV and the Ti $2p_{1/2}$ at 464.1eV respectively. The peak positions strongly suggest the presence of TiO_2 (Ti^{4+} state) (56) (107) (108). As for the high-resolution spectra for the Cu 2p peak we detect two peaks from the fitting corresponding to the Cu_2O and CuO main oxides. Specifically for the peak of Cu $2p_{3/2}$ we observe two deconvoluted peaks at 932.6eV and at 934.2eV with complete agreement with the Cu $2p_{1/2}$ detected peaks that appear at 952.5eV and 954.1eV respectively (109). In addition, there are two additional weaker peaks that confirm the existence of the shake up satellite peaks that are characteristic of the spectrum of CuO oxide (56) (73). From the integrated Gaussians we estimated the percentages (%) of the oxides as: $ZrO_2/TiO_2/CuO/Cu_2O$ = 65.6%/15.0%/11.7%/7.7%. The deconvoluted curves come into complete agreement with the phases recognized from the XRD data. The lack of the respective metallic peaks in XPS spectra indicates that the surface was completely oxidized indicating the advantage of the metallic glass as the buffer layer. From the fitting of the O 1s peak, the main peak appears at 529.9eV and it's attributed to the metallic oxides (56). The C 1s peak does not give any extra information for the properties of the sample, and it is only used for the determination of the chemical shift. It has a similar form with the C 1s peak of the Sn oxides samples. Hence, the high-resolution XPS spectra are shown in the following graphs of Figure 87.

ΜΕΤΑΠΤΥΧΙΑΚΗ ΔΙΠΛΩΜΑΤΙΚΗ ΕΡΓΑΣΙΑ ΟΝΟΜΑΤΕΠΩΝΥΜΟ: ΙΩΑΝΝΗΣ ΠΑΓΩΝΗΣ
ΤΙΤΛΟΣ: Growth and characterization of Type I (Straddling gap) and Type II (staggered gap) heterojunctions
alignment in thin films for potential photovoltaic applications
ΠΜΣ-Φυσικής   *Τμήμα Φυσικής*   *Πανεπιστήμιο Ιωαννίνων*

ΜΕΤΑΠΤΥΧΙΑΚΗ ΔΙΠΛΩΜΑΤΙΚΗ ΕΡΓΑΣΙΑ ΟΝΟΜΑΤΕΠΩΝΥΜΟ: ΙΩΑΝΝΗΣ ΠΑΓΩΝΗΣ
ΤΙΤΛΟΣ: Growth and characterization of Type I (Straddling gap) and Type II (staggered gap) heterojunctions alignment in thin films for potential photovoltaic applications
ΠΜΣ-Φυσικής   *Τμήμα Φυσικής*   *Πανεπιστήμιο Ιωαννίνων*

Figure 87: High resolution XPS spectra (b) Zr 3d (c) Ti 2p (d) Cu 2p (e) O 1s.

3.2.4 Electrical Measurements Results

We wanted to model the total results of the Type I and Type II heterojunctions for their photodetecting properties by performing a first comparison of the photoresponsivity of the Sn oxides with the Zr-Ti-Cu alloys. The samples were measured in the same light spectra and instrumentation as the one mentioned in the previous chapter. The characteristics are shown in the following Figure 88 for dark and white light conditions. The films do not seem to react in the same way as for the Sn oxides samples. It came out that there is a major difference between the illumination conditions something that indicates that the films are not so capable as potential devices. There is a very high possibility that the I-V characteristics correspond to the so-called S-shaped I-V curves a common phenomenon in solar cell research and originates from the growth parameters of the devices (110).
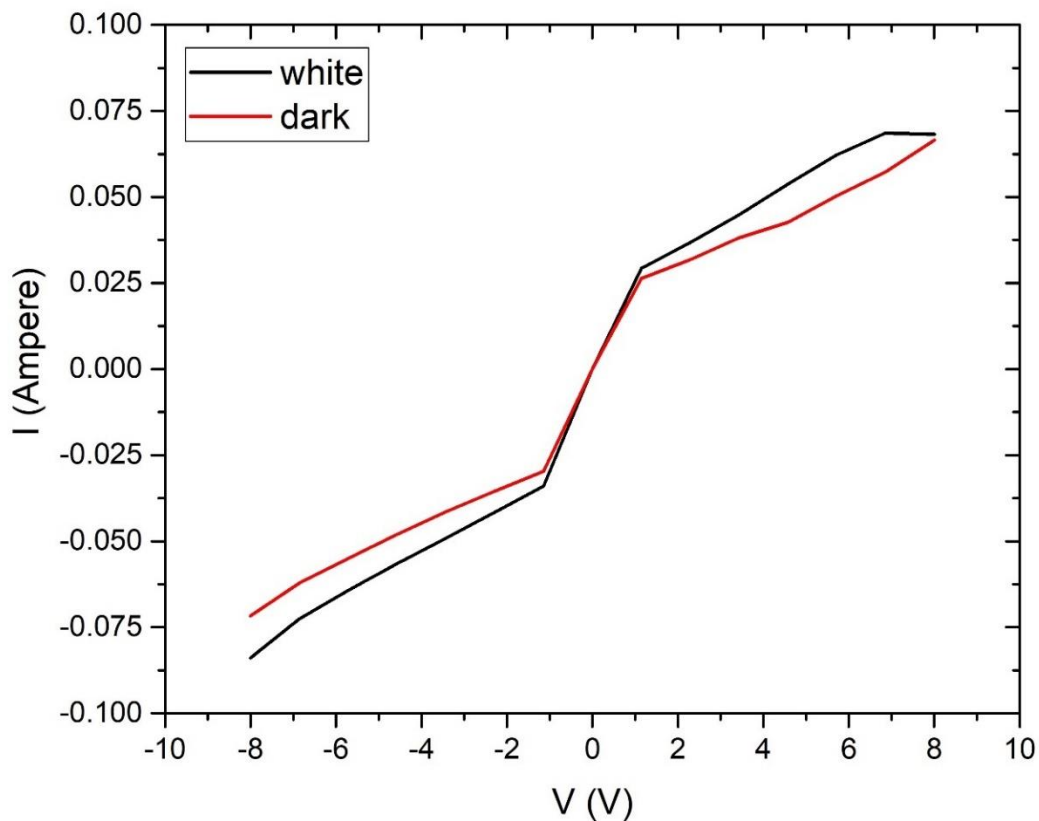
Figure 88: The I-V characteristics of the Zr-Ti-Cu oxides.

Additional photoresponse measurements were performed both at solar simulator and the Keithley setup for biases of 1V and 2V respectively. The results indicate no photoresponse from the exposure of the sample in solar simulator as it is shown at Figure 89. Meanwhile for the 4-probe measurement a total of four ON/OFF cycles of photoresponsivity were measured with ≈30sec duration of each cycle. Some indications of photoresponse are shown, but with a small current increase step of ≈0.13mA. Additively, the total current decreases over time indicating another drawback, Figure 90. Even though, the characteristic rise and recovery times at 0.7sec

and 0.1sec respectively indicate some promise. Although some positive results were extracted at the white light exposure, it is concluded that the films are not suitable as potential photoelectric devices as the Sn oxides system we developed. Still, the samples are promising as low light photodetectors and there might be still a chance of being appropriate photocatalysts.
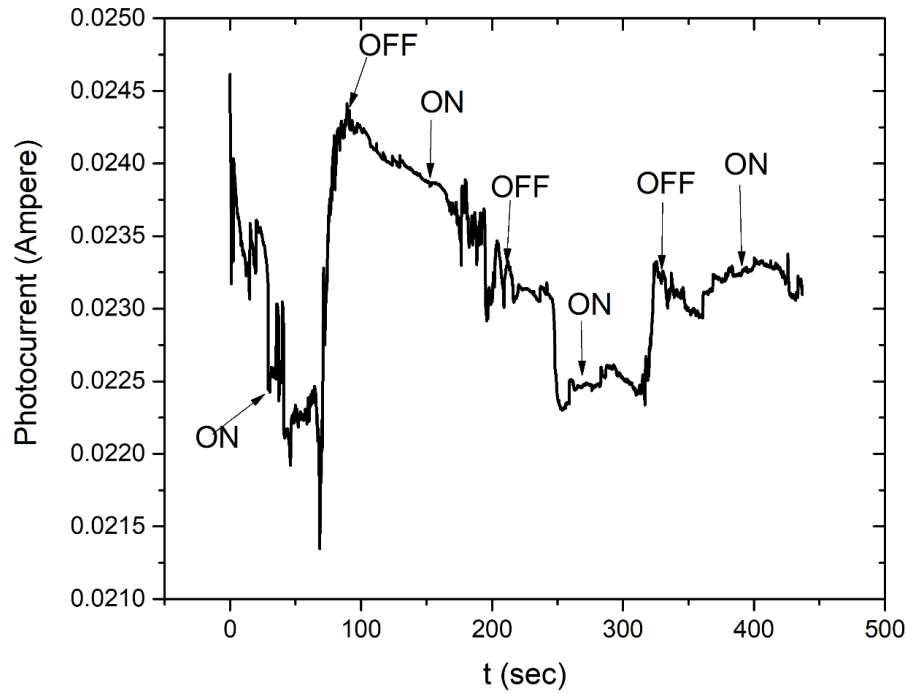
Figure 89: Photoresponse plots of Zr-Ti-Cu oxides under solar simulator for V=+1V.
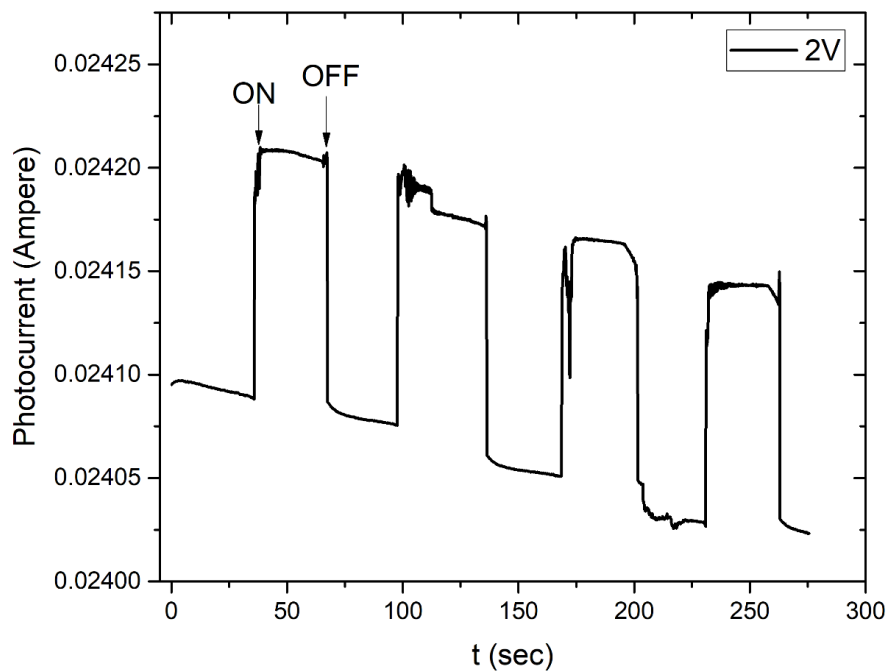
Figure 90: Photoresponse measurements under white light for V=+2V.

Conclusions

In this thesis we present experimental results from the growth of two types of heterojunction band alignment (I and II types). These materials were grown with a two-step process of magnetron sputtering deposition and oxygen plasma oxidation. The first system of Type II band alignment, we developed was the heterojunction of Sn oxides. Specifically, we produced rutile tetragonal SnO, SnO_2 and Sn_xO_y which has been identified as Sn_3O_4 intermediate oxide with the triclinic structure from the XRD. The oxides were confirmed by XPS measurements. As for the electrical measurements, I-V characteristics and photocurrent I-t measurements were conducted for the determination of their suitability as potential photodetectors or photovoltaic devices. The existence of Sn_3O_4 in big concentrations seems to create electron traps decreasing the resulting current. We conclude that these films could potentially be used in photodetecting, photocatalytic, or sensing devices.

The other material system we grew is an oxidized alloy of Zr-Cu-Ti metallic glass. The oxides of these materials are forming the Type I band alignment. The existence of the oxides was confirmed with the XRD diffraction pattern. Additionally with the use of XRD pattern we determined the crystal structures of the grown oxides. The existence of the elements was confirmed with the survey spectra of XPS, with no impurities detected. From the deconvoluted high resolution spectra we confirmed the existence of ZrO_2, CuO, Cu_2O and TiO_2 and estimated the percentages of the oxides in the outer surface. By the I-V measurements we concluded that they don't have the same behavior as the Type II Sn oxides. The photocurrent measurements indicated small photoresponse at the white light but at the overall results they are not suitable as potential solar cells. Generally, from the results we determined, we can conclude that the heterojunctions that form the Type II band alignment are more suitable for potential photovoltaic, sensing or photocatalytic uses.

ΜΕΤΑΠΤΥΧΙΑΚΗ ΔΙΠΛΩΜΑΤΙΚΗ ΕΡΓΑΣΙΑ ΟΝΟΜΑΤΕΠΩΝΥΜΟ: ΙΩΑΝΝΗΣ ΠΑΓΩΝΗΣ
ΤΙΤΛΟΣ: Growth and characterization of Type I (Straddling gap) and Type II (staggered gap) heterojunctions
alignment in thin films for potential photovoltaic applications
ΠΜΣ-Φυσικής   *Τμήμα Φυσικής*   *Πανεπιστήμιο Ιωαννίνων*

Index of Icons/Tables

Icons

ΜΕΤΑΠΤΥΧΙΑΚΗ ΔΙΠΛΩΜΑΤΙΚΗ ΕΡΓΑΣΙΑ ΟΝΟΜΑΤΕΠΩΝΥΜΟ: ΙΩΑΝΝΗΣ ΠΑΓΩΝΗΣ
ΤΙΤΛΟΣ: Growth and characterization of Type I (Straddling gap) and Type II (staggered gap) heterojunctions alignment in thin films for potential photovoltaic applications
ΠΜΣ-Φυσικής   *Τμήμα Φυσικής*   *Πανεπιστήμιο Ιωαννίνων*

Tables

References

1. **Donald R. Askeland, Pradeep P. Fulay, Wendelin J. Wright.** *The Science and Engineering of Materials.* 6th. s.l. : CL Engineering, 2010. 978-0495296027.

2. **Kittel, Charles.** *Introduction to Solid State Physics.* 4th. New York : John Wiley & Sons, 1971. 978-0-471-14286-7.

3. **Y. Bhargav Kumar, Ravindra K. Rawal, Ashutosh Thakur, G. Narahari Sastry.** Chapter 7 - Reversible and irreversible functionalization of graphene. [ed.] Frank Hagelberg Tandabany Dinadayalane. *Theoretical and Computational Chemistry.* 2022, Vol. 21, pp. 157-189.

4. **Wei Chen, Dongchen Qi, Xingyu Gao, Andrew Thye Shen Wee.** Surface transfer doping of semiconductors. *Progress in Surface Science.* 2009, Vol. 84, 9-10, pp. 279-321.

5. **Ruiz, Eliseo & Alvarez, Santiago & Alemany, Pere.** Electronic structure and properties of AlN. *Physical review. B, Condensed matter.* 1994, Vol. 49, pp. 7115-7123.

6. **Albert Malvino, David Bates.** *Electronic Principles (8th Edition).* s.l. : McGraw Hill, 2015. 978-0073373881.

7. **Electronic Devices and Circuit Theory, 11th Edition.** *Robert L Boylestad.* s.l. : Pearson, 2014. 978-9332542600.

8. **Vijay P. Singh, R.S. Singh, Karen E. Sampson.** *Chapter 6 - Thin-Film Solar Cells Based on Nanostructured CdS, CIS, CdTe and Cu2S,.* s.l. : Tetsuo Soga, 2006. pp. 167-190. 9780444528445.

9. **Sharma, Kusum & Raizada, Mrs. Pankaj & Hasija, Vasudha & Singh, Pardeep & Bajpai, Archana & Nguyen, Van-Huy & S, Rangabhashiyam & Kumar, Pawan & Nadda, Ashok & Kim, Soo Young & Varma, Rajender & Le Thi Thanh, Nhi & Le, Nhi & Le, Quyet.** ZnS-based quantum dots as photocatalysts for water purification. *ournal of Water Process Engineering.* 10 2021, Vol. 43, p. 102217.

ΜΕΤΑΠΤΥΧΙΑΚΗ ΔΙΠΛΩΜΑΤΙΚΗ ΕΡΓΑΣΙΑ ΟΝΟΜΑΤΕΠΩΝΥΜΟ: ΙΩΑΝΝΗΣ ΠΑΓΩΝΗΣ
ΤΙΤΛΟΣ: Growth and characterization of Type I (Straddling gap) and Type II (staggered gap) heterojunctions alignment in thin films for potential photovoltaic applications
ΠΜΣ-Φυσικής   *Τμήμα Φυσικής*   *Πανεπιστήμιο Ιωαννίνων*

10. **Ke Xu, Yuanfeng Xu, Hao Zhang, Bo Peng, Hezhu Shao, Gang Ni, Jing Li, Mingyuan Yao, Hongliang Lu, Heyuan Zhu and Costas M. Soukoulis.** The role of Anderson's rule in determining electronic, optical and transport properties of transition metal dichalcogenide heterostructures. 2018, Vol. 20, 48, pp. 30351-30364.

11. **Denton, Alan & Ashcroft, N.** Vegard's law. *Phys. Rev. A.* 03 1991, Vol. 43, pp. 3161-3164.

12. **Jiao Shuaishuai, Xue Wan, Zhang Cuimin, Li Feihu, Meng Bo & Zhan Zili.** Improving the formaldehyde gas sensing performance of the ZnO/SnO2 nanoparticles by PdO decoration. *Journal of Materials Science: Materials in Electronics.* 2020, Vol. 31, pp. 684–692.

13. **Hans, Lüth.** *Solid Surfaces, Interfaces and Thin Films. Graduate Texts in Physics.* s.l. : Springer, Cham, 2015. pp. 393–448. 978-3-319-10756-1.

14. **Dong In Kim, Ji Won Lee, Rak Hyun Jeong & Jin-Hyo Boo.** A high-efficiency and stable perovskite solar cell fabricated in ambient air using a polyaniline passivation layer. *Scientific Reports.* 01 2022, Vol. 12.

15. **William Chiappim Junior, Leandro X. Moreno, Rodrigo Savio Pessoa, António F. da Cunha, Pedro M.P. Salomé, Joaquim P. Leitão.** *Chapter 3 - Novel dielectrics compounds grown by atomic layer deposition as sustainable materials for chalcogenides thin-films photovoltaics technologies.* s.l. : Mariana Amorim Fraga, Delaina Amos, Savas Sonmezoglu, Velumani Subramaniam, 2021. pp. 71-100. 9780128215920.

16. **Long Hu, Qian Zhao, Shujuan Huang, Jianghui Zheng, Xinwei Guan, Robert Patterson, Jiyun Kim, Lei Shi, Chun-Ho Lin, Qi Lei, Dewei Chu, Wan Tao, Soshan Cheong, Richard D. Tilley, Anita W. Y. Ho-Baillie, Joseph M. Luther, Jianyu Yuan & Tom Wu.** Flexible and efficient perovskite quantum dot solar cells via hybrid interfacial architecture. *Nature Communications.* 01 2021, Vol. 12, 1.

17. **Shockley, William and Queisser, Hans J.** Detailed Balance Limit of Efficiency of p-n Junction Solar Cells. *Journal of Applied Physics.* 1961, Vol. 32, 3, pp. 510-519.

18. *Mathematical Tools for Computer-Generated Ornamental Patterns.* **Ostromoukhov, Victor.** Berlin : Springer, 2006. pp. 193–223.

19. **Das, Bijoy & Rastogi, Alok.** Thin Films for Secondary Data Storage. *IETE Journal of Research.* 1997, Vol. 43, pp. 221-232.

20. **George Loizos, George Giannopoulos, Christos Serletis, Tuhin Maity, Saibal Roy, Nicoleta Lupu, Hanae Kijima, Masahiro Yamaguchi, Dimitris Niarchos.** Soft Magnetic Multilayered Thin Films for HF Applications. *Physics Procedia.* 2015, Vol. 75, pp. 1096-1103.

21. **Tejendra K. Gupta, Manjeet Singh Goyat, Archana Dhyani, Ranjeet Kumar Brajpuriya.** *16 - Chemical vapor deposition of ferrite thin films.* s.l. : Woodhead Publishing, 2023. pp. 293-308. 9780128237175.

22. **Zhang, F., Mohammadi, E., Luo, X., Strzalka, J., Mei, J., & Diao, Y.** Zhang, F., Mohammadi, E., Luo, X., Strzalka, J., Mei, J., & Diao, Y. (2017). Critical Role of Surface Energy in Guiding Crystallization of Solution-Coated Conjugated Polymer Thin Films. Langmuir, 34(3), 1109–1122. doi:10.1021/acs.langmuir.7b02807 . *Langmuir.* 2017, Vol. 34, 3, pp. 1109-1122.

23. **Forgerini, F. L., & Marchiori, R.** A brief review of mathematical models of thin film growth and surfaces. *Biomatter.* 2014, Vol. 4, 1.

24. **Stephen J. Blundell, Katherine M. Blundell.** *Concepts in Thermal Physics (Second edition).* s.l. : Oxford University Press, U.S.A., 2009. 978-0199562107.

25. **I. Petrov, V. Orlinov, I. Ivanov, J. Kourtev.** Influence of the Basic Process Parameters on the Ion/Atom Arrival Rate Ratio during Magnetron Sputter Deposition of Thin Carbon Films. *Contributions to Plasma Physics.* 1988, Vol. 28, 3, pp. 265-273.

26. **B.S. Murty, J.W. Yeh, S. Ranganathan.** *Chapter 5 - Synthesis and Processing : High Entropy Alloys.* s.l. : B.S. Murty, J.W. Yeh, S. Ranganathan, 2014. pp. 77-89. 9780128002513.

27. **G.T. West, P.J. Kelly.** Influence of inert gas species on the growth of silver and molybdenum films via a magnetron discharge. *Surface and Coatings Technology.* 2011, Vol. 206, 7, pp. 1648-1652.

28. **Iliescu, Ciprian.** A COMPREHENSIVE REVIEW ON THIN FILM DEPOSITIONS ON PECVD REACTORS. *Annals of the Academy of Romanian Scientists Series on Science and Technology of Information.* 10 2021, Vol. 14, pp. 12-24.

29. **Panagiotopoulos, N.T. & Kovač, Janez & Cvelbar, Uroš & Patsalas, Panagiotis & Mozetic, Miran & Evangelakis, Georgos.** Tetragonal or monoclinic ZrO2 thin films from Zr-based glassy templates. *Journal of Vacuum Science & Technology A: Vacuum, Surfaces, and Films.* 09 2012, Vol. 30, pp. 051510-051510.

30. **Panagiotopoulos, N.T. & Kovač, Janez & Mozetic, Miran & Patsalas, P. & Evangelakis, Georgos.** Formation of tetragonal or monoclinic ZrO2 coatings by oxygen plasma treatment of Zr74.7Cu19.7Nb5.6 glassy thin films. *Journal of Vacuum Science & Technology A: Vacuum, Surfaces, and Films.* 09 2011, Vol. 29, pp. 051303-051303.

31. **Chen, Francis F.** *Introduction to Plasma Physics and Controlled Fusion.* s.l. : Springer Cham, 2015. 978-3319223087.

32. **Perera, Kalpani & Prendeville, Jack & Jaiswal, Amit & Jaiswal, Swarna.** old Plasma Technology in Food Packaging. *Coatings.* 12 2022, Vol. 12, p. 1896.

33. **Liu, Peitao & Shoulong, Wang & Li, Dianzhong & Li, Yiyi & Chen, Xing-Qiu.** Fast and Huge Anisotropic Diffusion of Cu (Ag) and Its Resistance on the Sn Self-diffusivity in Solid β-Sn. *Journal of Materials Science & Technology.* 12 2015, Vol. 32.

34. **Holleman, Arnold F., Wiberg, Egon and Wiberg, Nils.** Tin. *Lehrbuch der Anorganischen Chemie .* 1985, pp. 793–800.

35. **Akram, Muhammad.** Investigating the Effect of Dwell Time on the Physical Properties of Nano-sized Tin dioxide (SnO2) Prepared Through a Continuous Microwave Flow Process. *Pakistan Journal of Analytical & Environmental Chemistry.* 2021, Vol. 22, pp. 13-20.

36. **Asaithambi, Dr & Perumal, Sakthivel & Karuppaiah, Murugesan & Hayakawa, Y. & Loganathan, A. & Ravi, G.** Improved photocatalytic performance of nanostructured SnO2 via addition of alkaline earth metals (Ba2+, Ca2+ and Mg2+) under visible light irradiation. *Applied Physics A.* 03 2020, Vol. 126.

37. **Chen, Peng-Jen & Jeng, Horng-Tay.** Phase diagram of the layered oxide SnO: GW and electron-phonon studies. *Scientific Reports.* 05 2015, Vol. 5, p. 16359.

38. **Kachirayil J. Saji, Y.P. Venkata Subbaiah, Kun Tian, Ashutosh Tiwari.** P-type SnO thin films and SnO/ZnO heterostructures for all-oxide electronic and optoelectronic device applications. *Thin Solid Films.* 2016, Vol. 605, pp. 193-201.

39. **Cheuk Kai Gary Kwok, Ying Wang, Xingyu Shu, Kin Man Yu.** Conversion of p-type SnO to n-type SnO2 via oxidation and the band offset and rectification of an all-Tin oxide p-n junction structure. *Applied Surface Science.* 2023, Vol. 627, p. 157295.

40. **Roy, Animesh & Arbuj, Sudhir & Waghadkar, Yogesh & Shinde, Manish & Umarji, Govind & Rane, Sunit & Patil, Kashinath & Gosavi, Suresh & Chauhan, Ratna.** Concurrent synthesis of SnO/SnO2 nanocomposites and their enhanced photocatalytic activity. *Journal of Solid State Electrochemistry.* 01 2017, Vol. 21.

41. **Wang, Pengtao & Wanyin, Ge & Jia, Xiaohua & Huang, Jingtao & Zhang, Xinmeng & Lu, Jing.** SnO/SnO2 heterojunction: an alternative candidate for sensing NO2 with fast response at room temperature. *Frontiers of Materials Science.* 09 2022, Vol. 16, p. 220609.

42. **Adri Huda, Reisya Ichwani, Chanel Tri Handoko, Bambang Yudono, Muhammad Djoni Bustan, Fakhili Gulo.** Enhancing the visible-light photoresponse of SnO and SnO2 through the heterostructure formation using one-step hydrothermal route. *Materials Letters.* 2019, Vol. 238, pp. 264-266.

43. **Lawson, F.** Tin Oxide—Sn3O4. *Nature.* 1967, Vol. 215, pp. 955-956.

44. **Jinbo Zhang, Weiwei Xia, Mingtao Li, Zhipeng Yan, Saqib Rahman, Xianghua Zeng, Lin Wang, Jaeyong Kim.** Structural transformation and transport behavior of mixed valence compound Sn3O4 under high pressure. *Journal of Alloys and Compounds.* 2021, Vol. 886, p. 161197.

45. **Hu, Jianling & Tu, Jianhai & Li, Xingyang & Wang, Ziya & Yan, Li & Li, Quanshui & Wang, Fengping.** nhanced UV-Visible Light Photocatalytic Activity by Constructing Appropriate Heterostructures between Mesopore TiO2 Nanospheres and Sn3O4 Nanoparticles. *Nanomaterials.* 10 2017, Vol. 7, p. 336.

46. **Toyokazu Tanabe, Katsutoshi Nakamori, Tatsuhiro Tanikawa, Yasuo Matsubara, Futoshi Matsumoto.** Ultrathin nanosheet Sn3O4 for highly effective hydrogen evolution under visible light. *Journal of Photochemistry and Photobiology A: Chemistry.* 2021, Vol. 420, p. 113486.

47. **Weiwei Xia, Haibo Wang, Xianghua Zeng, Jie Han, Jun Zhu, Min Zhoua and Shudong Wua.** High-efficiency photocatalytic activity of type II SnO/Sn 3 O 4 heterostructures via interfacial charge transfer. *CrystEngComm.* 2014, Vol. 16, p. 6841.

48. **Kempa, K. & Michael, Giersig & Akinoglu, Eser & Han, Bing & RP, Li.** Physics of transparent conductors. *Advances in Physics.* 09 2016, Vol. 65, pp. 553-617.

49. **Edwards, Peter & Porch, A & Jones, Martin & Morgan, D & Perks, Richard.** Basic Materials Physics of Transparent Conducting Oxides. *Dalton transactions (Cambridge, England : 2003).* 11 2004, Vol. 19, pp. 2995-3002.

50. **Bibi, Shagufta & Shah, Attaullah & Mahmood, Arshad & Ali, Zahid & Raza, Qasim & Aziz, Uzma & Haneef, Aishath & Waheed, Abdul & Shah, Muhammad Zia Ullah.** Synthesis and characterization of binary ZnO–SnO2 (ZTO) thin films by e-beam evaporation technique. *Applied Physics A.* 03 2018, Vol. 124.

51. **Glenske K, Donkiewicz P, Köwitsch A, Milosevic-Oljaca N, Rider P, Rofall S, Franke J, Jung O, Smeets R, Schnettler R, Wenisch S, Barbeck M.** Applications of Metals for Bone Regeneration. *Int J Mol Sci.* 03 12, 2018, Vol. 19, 3.

52. **H. Men, Z.Q. Hu, J. Xu.** Bulk metallic glass formation in the Mg–Cu–Zn–Y system. *Scripta Materialia.* 2002, Vol. 46, 10, pp. 699-703.

53. **Yong Han, Junfa Zhu.** Surface Science Studies on the Zirconia-Based Model Catalysts. *Top Catal.* 07 2013, Vol. 56, pp. 1525–1541.

54. **M Landmann, E Rauls and W G Schmidt.** The electronic structure and optical response of rutile, anatase and brookite TiO2. *Journal of Physics: Condensed Matter.* 04 19, 2012, Vol. 24, 19, p. 195503.

55. **Di Paola, Agatino, Marianna Bellardita, and Leonardo Palmisano.** Brookite, the Least Known TiO2 Photocatalyst. Catalysts, 2013, Vol. 3, 1, pp. 36-73.

56. **Agrafioti, K.A. & Panagiotopoulos, N.T. & Moularas, Constantinos & Deligiannakis, Yiannis & Prouskas, Costas & Soukouli, P.P. & Evangelakis, Georgos.** Development of Ti-based nanocomposite oxide thin films with CuO and Nb2O5 additions suitable for catalytic applications. *Thin Solid Films.* 04 2023, Vol. 775, p. 139864.

57. **Ungeheuer K, Marszalek KW, Mitura-Nowak M, Perzanowski M, Jelen P, Marszalek M, Sitarz M.** Influence of Cr Ion Implantation on Physical Properties of CuO Thin Films. *International Journal of Molecular Sciences.* 04 2022, Vol. 23, 9, p. 4541.

58. **Gao, Ling & Pang, Chao & He, Dafang & Shen, Liming & Gupta, Arunava & Bao, Ningzhong.** Synthesis of Hierarchical Nanoporous Microstructures via the Kirkendall Effect in Chemical Reduction Process. *Scientific Reports.* 2015, Vol. 5, p. 16061.

59. **Sumita Choudhary, J. V. N. Sarma, Subhashis Gangopadhyay.** Growth and characterization of single phase Cu2O by thermal oxidation of thin copper films. *AIP Conference Proceedings.* 04 13, 2016, Vol. 1724, 1, p. 020116.

60. **Sawicka-Chudy, P., Sibiński, M., Wisz, G., Rybak-Wilusz, E., & Cholewa, M.** Numerical analysis and optimization of Cu2O/TiO2, CuO/TiO2, heterojunction solar cells using SCAPS. *Journal of Physics: Conference Series.* 05 2018, Vol. 1033, p. 012002.

61. **P L Khoo, K Satou and M Izaki.** The Electronic States of Copper Oxides Photoactive Layers Prepared by Electrodeposition followed by Annealing. *IOP Conference Series Materials Science and Engineering.* 2020, Vol. 920, 1, p. 012028.

62. **Dasineh Khiavi N, Katal R, Kholghi Eshkalak S, Masudy-Panah S, Ramakrishna S, Jiangyong H.** Visible Light Driven Heterojunction Photocatalyst of CuO–Cu2O Thin Films for Photocatalytic Degradation of Organic Pollutants. *Nanomaterials.* 2019, Vol. 9, 7, p. 1011.

63. **Mingkun Zhang, Lin Peng, Qichong Yuan, Liyuan Zheng, Yi Wang and Aiju Li.** A multifunctional separator modified using Y2O3/Co3O4 heterostructures boosting polysulfide

ΜΕΤΑΠΤΥΧΙΑΚΗ ΔΙΠΛΩΜΑΤΙΚΗ ΕΡΓΑΣΙΑ ΟΝΟΜΑΤΕΠΩΝΥΜΟ: ΙΩΑΝΝΗΣ ΠΑΓΩΝΗΣ
ΤΙΤΛΟΣ: Growth and characterization of Type I (Straddling gap) and Type II (staggered gap) heterojunctions alignment in thin films for potential photovoltaic applications
ΠΜΣ-Φυσικής   *Τμήμα Φυσικής*   *Πανεπιστήμιο Ιωαννίνων*

catalytic conversion for advanced Li–S batteries. *Sustainable Energy Fuels.* 07 2022, Vol. 6, pp. 3187-3194.

64. **Bilal Masood Pirzada, Niyaz A. Mir, Nida Qutub, Owais Mehraj, Suhail Sabir, M. Muneer.** Synthesis, characterization and optimization of photocatalytic activity of TiO2/ZrO2 nanocomposite heterostructures. *Materials Science and Engineering: B.* 2015, Vol. 193, pp. 137-145.

65. **Guerrero-Araque, Diana & Ramírez-Ortega, David & Acevedo-Peña, Próspero & Tzompantzi, F.J. & Calderon, H. & Gomez, Ricardo.** Interfacial Charge-Transfer Process across ZrO2-TiO2 Heterojunction and its Impact on Photocatalytic Activity. *Journal of Photochemistry and Photobiology A: Chemistry.* 2017, Vol. 335, pp. 276-286.

66. **M.R. Hoffmann, S.T. Martin, W. Choi, D.W. Bahnemann.** Environmental Applications of Semiconductor Photocatalysis. *Chemical Reviews.* 01 1995, Vol. 95, 1, pp. 69-96.

67. **Gaggero, Elisa & Calza, Paola & Cerrato, Erik & Paganini, Maria.** Cerium-, Europium- and Erbium-Modified ZnO and ZrO2 for Photocatalytic Water Treatment Applications: A Review. *Catalysts.* 12 2021, Vol. 11, p. 1520.

68. **Manikandan V, Packialakshmi JS, Bharti B, Jayanthi P, Dhandapani R, Velmurugan P, Elango D, Paramasivam R, Mohanavel V, Syed A, Elgorban AM, Bahkali AH, Muthupandian S.** Efficient One-Pot Synthesis of TiO2/ZrO2/SiO2 Ternary Nanocomposites Using Prunus × Yedoensis Leaf Extract for Enhanced Photocatalytic Dye Degradation. *Oxid Med Cell Longev.* 09 2022, Vol. 2022, pp. 1-14.

69. **P P Subha, L S Vikas and M K Jayaraj.** Solution-processed CuO/TiO 2 heterojunction for enhanced room temperature ethanol sensing applications. *Physica Scripta.* 03 2018, Vol. 93, 5, p. 055001.

70. **P.J Kelly, R.D Arnell.** Magnetron sputtering: a review of recent developments and applications. *Vacuum.* 2000, Vol. 56, 3, pp. 159-172.

71. **Hajakbari, Fatemeh & Rashvand, S. & Hojabri, Alireza.** Effect of plasma oxidation parameters on physical properties of nanocrystalline nickel oxide thin films grown by two-step method: DC sputtering and plasma oxidation. *Journal of Theoretical and Applied Physics.* 09 2019, Vol. 13, pp. 1-9.

72. **Montambaux, Gilles.** Generalized Stefan-Boltzmann Law. *Foundations of Physics.* 2018, Vol. 48, 4, pp. 395-410.

73. **Leng, Yang.** *Materials Characterization: Introduction to Microscopic and Spectroscopic Methods.* s.l. : Wiley-VCH Verlag GmbH & Co. KGaA, 2013. 9783527334636.

74. **B. D. Cullity, S. R. Stock.** *Elements of X-Ray Diffraction.* 3rd. s.l. : Pearson, 2001. 978-0201610918.

75. **Sarkar, Sumit & Das, Ratan.** Determination of structural elements of synthesized silver nano-hexagon from X-ray diffraction analysis. *Indian Journal of Pure and Applied Physics.* 10 2018, Vol. 56, pp. 765-772.

76. **Zaza, Fabio & Orio, Giovanni & Serra, Emanuele & Caprioli, F. & Pasquali, Mauro.** Low-Temperature Capacitive Sensor Based on Perovskite. *AIP COnference Proceedings.* 2015, Vol. 1667.

77. **Jeong Won Kim, Ansoon Kim.** Absolute work function measurement by using photoelectron spectroscopy. *Current Applied Physics.* 2021, Vol. 31, pp. 52-59.

78. **F.Watts, John.** *An Introduction to Surface Analysis by Electron Spectroscopy (Royal Microscopical Society Microscopy Handbooks).* Oxford : Oxford University Press., 1990.

79. **Briggs, D. and Grant, J.T.** *Surface analysis by Auger and x-ray photoelectron spectroscopy.* Chichester : IM Publications and Surface, 2003.

80. **Sun, Qian, Yen-Ping Peng, Hanlin Chen, Ken-Lin Chang, Yangyang Qiu and Shiau-Wu Lai.** Photoelectrochemical oxidation of ibuprofen via Cu2O-doped TiO2 nanotube arrays. *Journal of hazardous materials.* 2016, Vol. 319, pp. 121-9.

81. **Jung-Kyu Lee, Hyo-Chang Lee, Chin-Wook Chung.** E–H mode transition in inductively coupled plasma using Ar, O2, N2, and mixture gas. *Current Applied Physics.* 11, 2011, Vol. 5, pp. S149-S153.

82. **Preethi, T. and Senthil, Kalphana and Kan, Asho and Balakrishnaraja, Rengaraju and Sundaravel, B. and Saravanan, P.** Enhanced Humidity Sensing Properties of Surfactant-Free Hydrothermally Synthesized Tin Oxide Nanoparticles. *Journal of Nano- and Electronic Physics.* 01 2021, Vol. 13, pp. 06003-1.

83. **R.N. Mariammal, K. Ramachandran, B. Renganathan, D. Sastikumar.** On the enhancement of ethanol sensing by CuO modified SnO2 nanoparticles using fiber-optic sensor. *Sensors and Actuators B: Chemical.* 2012, Vol. 169, pp. 199-207.

84. **McCarthy, Gregory J. & Welton, Jean M.** X-Ray Diffraction Data for SnO2. An Illustration of the New Powder Data Evaluation Methods. *Powder Diffraction.* 09 1989, Vol. 4, 3, pp. 156-159.

85. **Sonia Jaśkaniec, Seán R. Kavanagh, João Coelho, Seán Ryan, Christopher Hobbs, Aron Walsh, David O. Scanlon & Valeria Nicolosi.** Solvent engineered synthesis of layered SnO for high-performance anodes. *npj 2D Materials and Applications volume.* 2021, Vol. 5.

86. **P.H. Suman, A.A. Felix, H.L. Tuller, J.A. Varela, M.O. Orlandi.** Comparative gas sensor response of SnO2, SnO and Sn3O4 nanobelts to NO2 and potential interferents. *Sensors and Actuators B: Chemical.* 2015, Vol. 208, pp. 122-127.

87. **Álvaro Caballero, Julián Morales and Luis Sánchez.** Tin Nanoparticles Formed in the Presence of Cellulose Fibers Exhibit Excellent Electrochemical Performance as Anode Materials in Lithium-Ion Batteries. *Electrochemical and Solid-State Letters.* 01 2005, Vol. 8, pp. 464-466.

88. **Fang Lu, Xiaobo Ji, Yingchang Yang, Wentao Denga and Craig E. Banks.** Room temperature ionic liquid assisted well-dispersed core-shell tin nanoparticles through cathodic corrosion. *RSC Advances.* 11 2013, Vol. 3, pp. 18791-18793.

89. **P, Zaumseil.** High-resolution characterization of the forbidden Si 200 and Si 222 reflections. *J Appl Crystallogr.* 03 2015, Vol. 48, pp. 528-532.

90. **Lili Zhao, Martin Steinhart, Maekele Yosef, Sung Kyun Lee, Torsten Geppert, Eckhard Pippel, Roland Scholz, Ulrich Gösele, and Sabine Schlecht.** Lithium Niobate Microtubes within Ordered Macroporous Silicon by Templated Thermolysis of a Single Source Precursor. *Chemistry of Materials.* 2005, Vol. 17, 1, pp. 3-5.

91. **Li-Xia Liu, Yang Zhou, Yu-Chung Chang, Jian-Rong Zhang, Li-Ping Jiang, Wenlei Zhu, Yuehe Lin.** Tuning Sn3O4 for CO2 reduction to formate with ultra-high current density. *Nano Energy.* 2020, Vol. 77, p. 105296.

92. **Haibo Zhu, Devon C. Rosenfeld, Moussab Harb, Dalaver H. Anjum, Mohamed Nejib Hedhili, Samy Ould-Chikh, and Jean-Marie Basset.** Ni–M–O (M = Sn, Ti, W) Catalysts Prepared by a Dry Mixing Method for Oxidative Dehydrogenation of Ethane. *ACS Catalysis.* 2016, Vol. 6, 5, pp. 2852–2866.

93. **Feng Qin, Yaya Ma, Shizheng Zheng, Changyuan Hu, Lin Wei, Ruofan Yang, Yanting Ma & Cuiqing Zhang.** Construction of Novel Z-Scheme N-CQDs/Sn3O4 Heterojunction for Excellent Photocatalytic Degradation of Organic Pollutant. *Journal of Cluster Science.* 2022, Vol. 33, 3, pp. 913–923 .

94. **Kim, Soyeon & Jahandar, Muhammad & Jeong, Jaehoon & Lim, Dong.** Recent Progress in Solar Cell Technology for Low-Light Indoor Applications. *Current Alternative Energy.* 01 2019, Vol. 3.

95. **Berengue, O. & Simon, R. & Chiquito, A. & Dalmaschio, Cleocir & Leite, Edson & Guerreiro, Haroldo & Guimarães, Francisco.** Semiconducting Sn3O4 nanobelts: Growth and electronic structure. *Journal of Applied Physics.* 107, 2010, Vol. 3.

96. **Bak, S.-Y., et al.** Sensitivity Improvement of Urchin-Like ZnO Nanostructures Using Two-Dimensional Electron Gas in MgZnO/ZnO. *Sensors.* 2019, Vol. 19, p. 5195.

97. **Mohamed S. Mahdi, K. Ibrahim, Naser M. Ahmed, A. Hmood, Shrook A. Azzez, Falah I. Mustafa, M. Bououdina.** Influence of pH value on structural, optical and photoresponse properties of SnS films grown via chemical bath deposition. *Materials Letters.* 2018, Vol. 210, pp. 279-282.

98. **He Q, Tian Y, Wu Y, Liu J, Li G, Deng P, Chen D.** Electrochemical Sensor for Rapid and Sensitive Detection of Tryptophan by a Cu2O Nanoparticles-Coated Reduced Graphene Oxide Nanocomposite. *Biomolecules.* 05 8, 2019, Vol. 9, 5, p. 176.

99. **Kang, Anita Sagadevan Ethiraj & Dae Joon.** Synthesis and characterization of CuO nanowires by a simple wet chemical method. *Nanoscale Research Letters .* 2012, Vol. 7, 70.

100. **Vu, Trang and Gim, Jihyeon and Kim, Jaekook.** Potassium-doped copper oxide nanoparticles synthesized by a solvothermal method as an anode material for high-performance lithium ion secondary battery. *Applied Surface Science.* 2014, Vol. 305.

101. **Robotti, Marco and Dosta, S. and Cano, Irene G. and Concustell, Amadeu and Cinca, Nuria and Guilemany, Jose Maria.** Attrition and Cryogenic milling powder production for Low Pressure Cold Gas Spray and composite coatings characterization. *Advanced Powder Technology.* 04 2016, Vol. 27.

102. **Srivastava, Leeladhar Chouhan & Sandeep Kumar.** Role of Anatase/Rutile Phases in Tuning the Magnetic, Optical, and Dielectric Properties of Mg-Doped TiO2 Compounds for

ΜΕΤΑΠΤΥΧΙΑΚΗ ΔΙΠΛΩΜΑΤΙΚΗ ΕΡΓΑΣΙΑ ΟΝΟΜΑΤΕΠΩΝΥΜΟ: ΙΩΑΝΝΗΣ ΠΑΓΩΝΗΣ
ΤΙΤΛΟΣ: Growth and characterization of Type I (Straddling gap) and Type II (staggered gap) heterojunctions
alignment in thin films for potential photovoltaic applications
ΠΜΣ-Φυσικής   *Τμήμα Φυσικής*   *Πανεπιστήμιο Ιωαννίνων*

Spintronics Application. *Journal of Superconductivity and Novel Magnetism.* 11 2022, Vol. 35, pp. 3807-3812.

103. **Guo C, Wang P, Liao S, Si H, Chen S, Fan G, Wang Z.** Morphology-Controllable Hydrothermal Synthesis of Zirconia with the Assistance of a Rosin-Based Surfactant. *Applied Sciences.* 2019, Vol. 9, 19, p. 4145.

104. **Wang, Jigang and Yin, Wenyan and He, Xiao and Wang, Qiang and Guo, Ming and Chen, Shaowei.** Good Biocompatibility and Sintering Properties of Zirconia Nanoparticles Synthesized via Vapor-phase Hydrolysis. *Scientific Reports.* 10 2016, Vol. 6, p. 35020.

105. **Málek J, Beneš L, Mitsuhashi T.** Powder diffraction data and Rietveld refinement of metastable t-ZrO2 at low temperature. *Powder Diffraction.* 1997, Vol. 12, 2, pp. 96-98.

106. **Liu, Jiangwei and Liao, Meiyong and Imura, Masataka and Tanaka, Akihiro and Iwai, Hideo and Koide, Yasuo.** Low on-resistance diamond field effect transistor with high-k ZrO2 as dielectric. *Scientific Reports.* 09 2014, Vol. 4, 1, p. 6395.

107. **Xiaodong Zhu, Guilan Wen, Hui Liu, Shihu Han, Shanhua Chen, Qingquan Kong & Wei Feng.** One-step hydrothermal synthesis and characterization of Cu-doped TiO2 nanoparticles/nanobucks/nanorods with enhanced photocatalytic performance under simulated solar light. *Journal of Materials Science: Materials in Electronics.* 07 2019, Vol. 30, pp. 13826–13834.

108. **Jianping Xu, Yanyan Gao, Shaobo Shi, Lina Kong, Rui Cao, Jing Chen, Yichen Bu, Xiaosong Zhang & Lan Li.** Growth of MoS2 nanoflakes and the photoelectric response properties of MoS2/TiO2 NRs compositions. *Journal of Materials Science: Materials in Electronics.* 2019, Vol. 30, pp. 21465–21476.

109. **Yiting Wang, Yinyun Lü, Wenwen Zhan, Zhaoxiong Xie, Qin Kuang and Lansun Zhenga.** Synthesis of Porous Cu2O/CuO Cages using Cu-based Metal-Organic-Framework as Templates and their Gas-sensing Properties. *J. Mater. Chem. A.* 2015, Vol. 24, 3, pp. 12796-12803.

110. **Lijian Zuo, Jizhong Yao, Hanying Li, Hongzheng Chen.** Assessing the origin of the S-shaped I–V curve in organic solar cells: An improved equivalent circuit model. *Solar Energy Materials and Solar Cells.* 2014, Vol. 122, pp. 88-93.

111. **C M Goringe, D R Bowler and E Hernández.** Tight-binding modelling of materials. *Records on Progress in Physics.* 1997, Vol. 60, 12, p. 1447.

112. **Killen, R. & Morrissey, Liam & Burger, Matthew & Vervack, Ronald & Tucker, Orenthal & Savin, Daniel.** The Influence of Surface Binding Energy on Sputtering in Models of the Sodium Exosphere of Mercury. *The Planetary Science Journal.* 06 2022, Vol. 3, p. 139.

113. **Kwon, Sasikala Sundar and Ganesh Venkatachalam and Seong Jung.** Biosynthesis of Copper Oxide (CuO) Nanowires and Their Use for the Electrochemical Sensing of Dopamine. *Nanomaterials.* 2018, Vol. 8.

APPENDIX A : XPS Concentrations Script (Sage Math v9.1)

```
x = var('x')

# Fit parameters for a deconvoluted peak
A_value = 6000
FWHM_value = 1
mu_value = 486.0

# Gaussian parameters for the photoelectron peak
A2_value = 8000
FWHM2_value = 2
mu2_value = 487.0

# Define the Gaussian function with constants
gaussian = A_value * exp(-((x - mu_value)**2) / (2 * (FWHM_value / (2 * sqrt(2 *
log(2))))**2))

# Define the Gaussian function with constants for the photoelectron peak
gaussian2 = A2_value * exp(-((x - mu2_value)**2) / (2 * (FWHM2_value / (2 *
sqrt(2 * log(2))))**2))

# Set the integration limits
lower_limit = 484.5
upper_limit = 488.5

# Set the integration limits for the photoelectron peak
lower_limit2 = 484
upper_limit2 = 489

# Numerically integrate the Gaussian function. Error estimate represents the accuracy.
area_numeric, error_estimate1 = numerical_integral(gaussian, lower_limit,
upper_limit)

# Numerically integrate the photoelectron peak. Error estimate2 represents the
accuracy.
area_numeric2, error_estimate2 = numerical_integral(gaussian2, lower_limit2,
upper_limit2)

# Result of Area of the deconvoluted curve (phase or state)
print("Numeric Area under the curve:", area_numeric)

# Result of Area of the photoelectron peak
print("Numeric Area of the photoelectron peak:", area_numeric2)

# Calculation of the %percentage of a denconvoluted curve (phase or state)
print("Percentage of the phase in the peak :",(100*area_numeric)/area_numeric2,"%")
```